

INFLUENCE OF PARTICLE SHAPE ON DILATANCY AND LIQUEFACTION  
SUSCEPTIBILITY

by

Deniz Ranjpour

B.S., Civil Engineering, University of Tabriz, 2012

Submitted to the Institute for Graduate Studies in  
Science and Engineering in partial fulfillment of  
the requirements for the degree of  
Master of Science

Graduate Program in Civil Engineering  
Boğaziçi University

2015

INFLUENCE OF PARTICLE SHAPE ON DILATANCY AND LIQUEFACTION  
SUSCEPTIBILITY

APPROVED BY:

Assoc. Prof. Özer ÇİNİCİOĞLU .....  
(Thesis Supervisor)

Prof. Erol GÜLER .....

Assist. Prof. Berrak TEYMUR .....

DATE OF APPROVAL: 15.07.2015

## ACKNOWLEDGEMENTS

First of all, I would like to express my sincere gratitude to my thesis supervisor, Assoc. Prof. Özer Çinicioğlu, for his precious and ceaseless support. I believe his keen look, prominent knowledge and meticulous comments eased the way for this study to shape.

I would like to thank the members of the thesis committee, Prof. Erol Güler and Assist. Prof. Berrak Teymur for their invaluable time and attention.

I would also like to thank Turkish Scientific and Technical Researches Institute (TÜBİTAK) for supporting me financially during my M.S studies. This research was supported by Turkish Scientific and Technological Research Council of Turkey (TÜBİTAK), Project number: 114M329.

Finally, I would like to thank my family for their endless love and my friends in Karl Terzaghi Laboratory for their priceless helps.

## ABSTRACT

# INFLUENCE OF PARTICLE SHAPE ON DILATANCY AND LIQUEFACTION SUSCEPTIBILITY

Dilatancy is a volumetric parameter directly dependant on void ratio ( $e$ ), and as a result relative density ( $I_D$ ), as well as confinement pressure  $p'_i$ . Besides, liquefaction is a behavior of saturated cohesionless soils under undrained condition, depending on the increase of pore water pressure inside the voids during cyclic loading. The effect of dilatancy on liquefaction phenomena has been studied by other researchers and in general, they concluded that phases of dilation can result in significant regain in shear stiffness and strength, as a result of instances of pore-pressure reduction. The aim of this study is to investigate the influence of particle shape on peak dilation angle and liquefaction susceptibility. Additionally, the correlation between peak dilatancy angle and liquefaction susceptibility is examined. For this purpose, first of all, microscopic pictures of 50 individual particles of 3 sand types were processed using an image processing software (ImageJ) to quantify their average circularity and roundness. Then conducting CD triaxial tests on each of 3 sand types, dilatancy constants  $\alpha_\psi$  and  $m_\psi$  of Cinicioglu and Abadkon [30] relationship were obtained. Finally over 200 cyclic simple shear tests were conducted on sand specimens observe peak dilatancy angle-number of cycles to liquefy relationships for the sand types. Defining normalized number of cycles to liquefy, the relationship between peak dilatancy angle and normalized number of cycles to liquefy was investigated. Other cyclic shearing variables were also taken into account. The effects of initial cyclic shear stress, consolidation pressure, stress ratio amplitude and cyclic period on dynamic behavior were investigated. The most important point about this study is probing the effect of different agents on dilation angle and liquefaction susceptibility from a more numerical point of view.



## ÖZET

### PARÇACIK GEOMETRİSİNİN GENLEŞME VE SIVILAŞABİLİRLİK ÜSTÜNDEKİ ETKİSİ

Hacimsel genleşme, boşluk oranı  $e$  'na direk bağlı olan ve özgül ağırlık ( $I_D$ ) ile efektif gerilmenin ( $p'_i$ ) sonucu olarak meydana gelen bir hacimsel parametredir. Ayrıca sıvılaşma, doymuş kohezyonsuz zeminlerin tekrarlı yükleme altında boşluklardaki su basıncının artışına bağlı olarak drenajsız durumundaki davranışdır. Bu çalışmanın amacı, parçacık geometrisi etkisinin maksimum genleşme açısı ve sıvılaşılabiliğe etkisinin araştırılmasıdır. Bununla beraber, maksimum genleşme açısı ile sıvılaşılabiliğin arasındaki ilişki de araştırılmıştır. Bu çalışmanın kapsamında öncelikle 3 farklı kum tipine ait olan 50 farklı parçacığın mikroskobik şekilleri, bir görüntü işlem programı (ImageJ) yardımı ile ortalama daireselliklerinin belirlenmesi yolu ile değerlendirilmiştir. Daha sonra her 3 kum tipine CD (konsolidasyonlu-drenajlı) üç eksenli basınç testi yapılarak, Çinicioğlu ve Abadkon bağıntısının hacimsel genleşme katsayıları  $\alpha_\psi$  ve  $m_\psi$  elde edilmiştir. Sonuç olarak kum numeneleri üzerinde, maksimum genleşim açısı-sıvılaşmaya neden olan tekrarlı sayısı ilişkisini gözlemlemek amacı ile 4 farklı gerilme oranı genişliğinde ve tekrarlı periyot kombinasyonlarında ve farklı konsolidasyon basınçlarında (50 kPa, 100 kPa ve 150 kPa) 200'den fazla tekrarlı direkt basit kesme deneyi uygulanmıştır. Araştırmanın ilerki aşamasında, diğer tekrarlı kayma parametreleri de dikkate alınmıştır. Başlangıç tekrarlı kayma gerilmesinin, konsolidasyon basıncının, gerilme oranı genişliğinin ve tekrarlı periyodunun; maksimum genleşme açısı-sıvılaşmaya neden olan tekrarlı sayısı veya maksimum genleşim açısı-normalize edilmiş sıvılaşmaya neden olan tekrarlı sayısı değerlerine etkileri araştırılmıştır. Bu çalışma ile vurgulanmak istenen en önemli nokta, farklı etkenlerin genleşim açısı ve sıvılaşılabiliğin üzerindeki etkilerinin daha sayısal bir bakış açısı ile araştırılmasıdır.

## TABLE OF CONTENTS

ACKNOWLEDGEMENTS . . . . .	iii
ABSTRACT . . . . .	iv
ÖZET . . . . .	v
LIST OF FIGURES . . . . .	viii
LIST OF TABLES . . . . .	xiv
LIST OF SYMBOLS . . . . .	xvi
LIST OF ACRONYMS/ABBREVIATIONS . . . . .	xix
1. INTRODUCTION . . . . .	1
2. LITERATURE REVIEW . . . . .	3
2.1. Particle Shape Quantification . . . . .	3
2.2. Shear Strength and Dilation . . . . .	6
2.3. Relationship Between Friction and Dilatancy Angles . . . . .	9
2.4. Influence of Particle Shape on Soil Strength and Dilatancy . . . . .	13
2.5. Liquefaction and Liquefaction Potential . . . . .	15
2.6. Influence of Particle Shape on Liquefaction Susceptibility . . . . .	16
2.7. Imaging Techniques for Defining Particle Shape . . . . .	17
2.8. Image Processing Software . . . . .	18
2.9. Triaxial Testing History . . . . .	18
2.10. Cyclic Simple Shear Test History . . . . .	19
2.11. Simulating Undrained Condition with Constant Volume Condition . . . . .	20
3. METHODOLOGY . . . . .	21
3.1. Shape Factor Analysis . . . . .	21
3.2. Triaxial Testing Program . . . . .	25
3.3. Automated Triaxial Testing Apparatus . . . . .	27
3.3.1. Triaxial Testing Procedure . . . . .	28
3.3.2. Sample Preparation . . . . .	30
3.3.3. Test Corrections . . . . .	30
3.4. Cyclic Simple Shear Testing . . . . .	33
3.4.1. CSS Testing Program . . . . .	33

3.4.2.	Automated Cyclic Simple Shear Testing Apparatus . . . . .	34
3.4.3.	Cyclic Simple Shear Testing Procedure . . . . .	35
3.4.4.	Sample Preparation . . . . .	39
3.4.5.	Testing Materials . . . . .	39
4.	EXPERIMENTS AND TEST RESULTS . . . . .	41
4.1.	Shape Factor Analysis Results . . . . .	41
4.2.	Triaxial Testing . . . . .	48
4.2.1.	Sile Sand Triaxial Test Results . . . . .	49
4.2.2.	Kilyos Sand Triaxial Test Results . . . . .	51
4.3.	Cyclic Simple Shear Test . . . . .	54
4.3.1.	Akpınar Sand CSS Test Results . . . . .	58
4.3.2.	Sile Sand CSS Test Results . . . . .	63
4.3.3.	Kilyos Sand CSS Test Results . . . . .	66
5.	DISCUSSION . . . . .	74
5.1.	Influence of Particle Shape on Critical State Friction Angle . . . . .	75
5.2.	Influence of Shape Factor on Dilatancy Angle . . . . .	76
5.3.	Influence of Vertical Pressure on Liquefaction Susceptibility . . . . .	78
5.4.	Liquefaction Potential of Sands with Regard to Dilation angle . . . . .	81
5.5.	Influence of Stress Ratio Amplitude on Liquefaction Susceptibility . . . . .	86
5.5.1.	Akpınas Sand SRA Effect . . . . .	86
5.5.2.	Sile Sand SRA Effect . . . . .	87
5.5.3.	Kilyos Sand SRA Effect . . . . .	89
5.5.4.	Comparing SRA Effects . . . . .	90
5.6.	Influence of Cyclic Period on Liquefaction Susceptibility . . . . .	93
5.6.1.	Akpınar Sand CP Effect . . . . .	93
5.6.2.	Sile Sand CP Effect . . . . .	94
5.6.3.	Kilyos Sand CP Effect . . . . .	96
5.6.4.	Comparing CP Effects . . . . .	97
6.	CONCLUSIONS . . . . .	100
6.1.	Recommendations for Future Work . . . . .	102
	REFERENCES . . . . .	103

## LIST OF FIGURES

Figure 2.1.	Powers [9] Qualitative Sphericity-Roundness Chart. . . . .	4
Figure 2.2.	Krumbein [10] Comparison Chart for Roundness. . . . .	4
Figure 2.3.	Krumbein and Sloss [11] Particle Roundness- Sphericity Chart. . .	4
Figure 2.4.	The $R(\theta)$ Method. . . . .	6
Figure 2.5.	Typical Shearing Responses of Granular Soils [19]. . . . .	7
Figure 2.6.	Dilatancy Effects on Coulomb's Failure Envelope [20]. . . . .	8
Figure 2.7.	Peak, Critical and Residual State of the Soil During Shearing. . .	9
Figure 2.8.	Assumed Sliding Mechanism for Rowe's Stress Dilatancy Relation- ship [25]. . . . .	11
Figure 3.1.	Example Image of Akpinar Sand Particles. . . . .	22
Figure 3.2.	Example Binary image of Akpinar Sand Particles. . . . .	22
Figure 3.3.	Example Image of Numbers Ascribed to Akpinar Sand Particles. .	23
Figure 3.4.	Example ImageJ Output Table. . . . .	23
Figure 3.5.	Automatic Triaxial System. . . . .	27
Figure 3.6.	Schematic of a Flow Trac Unit [22]. . . . .	28

Figure 3.7.	Piston Area Correction Test (Abadkon, 2012). . . . .	31
Figure 3.8.	Variation of Uplift Force With Cell Pressure (Abadkon, 2012). . .	31
Figure 3.9.	Two Different Area Corrections According to Sample Shape. . . .	32
Figure 3.10.	GeoComp Direct Simple Shear Apparatus. . . . .	34
Figure 3.11.	Vertical and Simple Shear Loads. . . . .	34
Figure 3.12.	GeoComp Direct Simple Shear Apparatus. . . . .	35
Figure 3.13.	An ideal waveform [76]. . . . .	37
Figure 3.14.	The limit for difference in amplitudes of successive half-cycles [76].	37
Figure 3.15.	The limit for difference in duration of successive half-cycles [76]. .	38
Figure 3.16.	Unacceptable waveform due to spikes at peaks [76]. . . . .	38
Figure 3.17.	Unacceptable ringing on waveform [76]. . . . .	38
Figure 3.18.	Akpinar Grain Size Distribution. . . . .	40
Figure 3.19.	Kilyos Grain Size Distribution. . . . .	40
Figure 3.20.	Sile Grain Size Distribution. . . . .	40
Figure 4.1.	Example Dilation Angle-Axial Strain Diagram. . . . .	49

Figure 4.2.	Sile sand $\tan \psi_p$ calculated with Schanz and Vermeer [29] relationship - $\tan \psi_p$ calculated with Cinicioglu and Abadkon [30] relationship. . . . .	50
Figure 4.3.	Linear relationship between peak friction angle and peak dilation angle of Sile sand. . . . .	51
Figure 4.4.	Kilyos sand $\tan \psi_p$ calculated with Schanz and Vermeer [29] relationship - $\tan \psi_p$ calculated with Cinicioglu and Abadkon [30] relationship. . . . .	53
Figure 4.5.	Linear relationship between peak friction angle and peak dilation angle of Kilyos sand. . . . .	53
Figure 4.6.	Example CSS Test Result. . . . .	55
Figure 4.7.	Relative Density- $K_o$ Relationship for Akpinar Sand. . . . .	56
Figure 4.8.	Relative Density- $K_o$ Relationship for Kilyos Sand. . . . .	57
Figure 4.9.	Relative Density- $K_o$ Relationship for Sile Sand. . . . .	57
Figure 4.10.	Akpinar $\tan \psi_p$ - $NCL$ (Consolidation pressure= 50 kpa). . . . .	60
Figure 4.11.	Akpinar $\tan \psi_p$ - $NCL$ (Consolidation pressure= 100 kpa). . . . .	61
Figure 4.12.	Sile $\tan \psi_p$ - $NCL$ (Consolidation pressure= 50 kpa). . . . .	64
Figure 4.13.	Sile $\tan \psi_p$ - $NCL$ (Consolidation pressure= 100 kpa). . . . .	66
Figure 4.14.	Kilyos $\tan \psi_p$ - $NCL$ (Consolidation pressure= 50 kpa). . . . .	68

Figure 4.15.	Kilyos $\tan \psi_p$ - $NCL$ (Consolidation pressure= 100 kpa). . . . .	70
Figure 4.16.	Kilyos $\tan \psi_p$ - $NCL$ (Consolidation pressure= 150 kpa). . . . .	72
Figure 5.1.	Influence of Circularity on Critical State Friction Angle. . . . .	75
Figure 5.2.	Influence of Roundness on Critical State Friction Angle. . . . .	76
Figure 5.3.	Influence of Particle Circularity and Roundness on $\alpha_\psi$ and $m_\psi$ values. . . . .	77
Figure 5.4.	Kilyos $\tan \psi_p$ - $NCL$ Relationship, Initial Shear Stress=30 kPa, CP=1 sec. . . . .	78
Figure 5.5.	Kilyos $\tan \psi_p$ - $NCL$ Relationship, Initial Shear Stress=30 kPa, CP=2 sec. . . . .	79
Figure 5.6.	Kilyos $\tan \psi_p$ - $NNCL$ Relationship, Initial Shear Stress=30 kPa, CP=1 sec. . . . .	80
Figure 5.7.	Kilyos $\tan \psi_p$ - $NNCL$ Relationship, Initial Shear Stress=30 kPa, CP=2 sec. . . . .	80
Figure 5.8.	$\tan \psi_p$ - $NNCL$ Relationships, Vertical Stress=50 kPa, SRA=0.2, CP=1 sec. . . . .	81
Figure 5.9.	$\tan \psi_p$ - $NNCL$ Relationships, Vertical Stress=50 kPa, SRA=0.2, CP=2 sec. . . . .	82
Figure 5.10.	$\tan \psi_p$ - $NNCL$ Relationships, Vertical Stress=50 kPa, SRA=0.3, CP=1 sec. . . . .	83

Figure 5.11. $\tan \psi_p$ - $NNCL$ Relationships, Vertical Stress=50 kPa, SRA=0.3, CP=2 sec. . . . .	83
Figure 5.12. $\tan \psi_p$ - $NNCL$ Relationships, Vertical Stress=100 kPa, SRA=0.2, CP=1 sec. . . . .	84
Figure 5.13. $\tan \psi_p$ - $NNCL$ Relationships, Vertical Stress=100 kPa, SRA=0.2, CP=2 sec. . . . .	84
Figure 5.14. $\tan \psi_p$ - $NNCL$ Relationships, Vertical Stress=100 kPa, SRA=0.2, CP=2 sec. . . . .	85
Figure 5.15. $\tan \psi_p$ - $NNCL$ Relationships, Vertical Stress=100 kPa, SRA=0.3, CP=1 sec. . . . .	85
Figure 5.16. Akpinar Sand SRA Effect on $\tan \psi_p$ - $NNCL$ Relationships, CP=1 sec. . . . .	86
Figure 5.17. Akpinar Sand SRA Effect on $\tan \psi_p$ - $NNCL$ Relationships, CP=2 sec. . . . .	87
Figure 5.18. Sile Sand SRA Effect on $\tan \psi_p$ - $NNCL$ Relationships, CP=1 sec.	88
Figure 5.19. Sile Sand SRA Effect on $\tan \psi_p$ - $NNCL$ Relationships, CP=2 sec.	88
Figure 5.20. Kilyos Sand SRA Effect on $\tan \psi_p$ - $NNCL$ Relationships, CP=1 sec.	89
Figure 5.21. Kilyos Sand SRA Effect on $\tan \psi_p$ - $NNCL$ Relationships, CP=2 sec.	90
Figure 5.22. $\tan \psi_p - (NNCL)_{CP}$ Relationships, CP=1 sec. . . . .	91



Figure 5.23. $\tan \tan \psi_p - (NNCL)_{CP}$ Relationships, CP=2 sec. . . . .	92
Figure 5.24. Akpinar Sand CP Effect on $\tan \psi_p$ - $NNCL$ Relationships, SRA=0.2. . . . .	93
Figure 5.25. Akpinar Sand CP Effect on $\tan \psi_p$ - $NNCL$ Relationships, SRA=0.3. . . . .	94
Figure 5.26. Sile Sand CP Effect on $\tan \psi_p$ - $NNCL$ Relationships, SRA=0.2. . . . .	95
Figure 5.27. Sile Sand CP Effect on $\tan \psi_p$ - $NNCL$ Relationships, SRA=0.3. . . . .	95
Figure 5.28. Kilyos Sand CP Effect on $\tan \psi_p$ - $NNCL$ Relationships, SRA=0.2. . . . .	96
Figure 5.29. Kilyos Sand CP Effect on $\tan \psi_p$ - $NNCL$ Relationships, SRA=0.3. . . . .	97
Figure 5.30. $\tan \psi_p$ -( $NNCL$ ) $_{SRA}$ Relationships, SRA=0.2. . . . .	99
Figure 5.31. $\tan \psi_p$ -( $NNCL$ ) $_{SRA}$ Relationships, SRA=0.3. . . . .	99

## LIST OF TABLES

Table 3.1.	Comparison of Theoretical and Predicted Shape Parameter Values [19]. . . . .	21
Table 3.2.	Number of Analyzed Particles. . . . .	24
Table 3.3.	Sile Sand Triaxial Testing. . . . .	26
Table 3.4.	Kilyos Sand Triaxial Testing. . . . .	26
Table 3.5.	CSS Tests SRA and CP Combinations. . . . .	36
Table 3.6.	Sand Properties. . . . .	39
Table 4.1.	Average Circularity and Roundness Values for All Sand Types. . .	41
Table 4.2.	Circularity and Roundness Values of Individual Sile Sand Particles.	42
Table 4.3.	Circularity and Roundness Values of Individual Akpınar Sand Par- ticles. . . . .	44
Table 4.4.	Circularity and Roundness Values of Individual Kilyos Sand Particles.	46
Table 4.5.	Sile Sand Triaxial Testing. . . . .	49
Table 4.6.	Kilyos Sand Triaxial Testing. . . . .	52
Table 4.7.	SRA and CP Combinations. . . . .	54

Table 4.8.	Equations Used to Calculate $K_0$ for CSS samples. . . . .	57
Table 4.9.	Akpinar CSS Test Results for 50 Kpa Consolidation Pressure. . . .	58
Table 4.10.	Akpinar CSS Test Results for 100 Kpa Consolidation Pressure. . .	62
Table 4.11.	Sile CSS Test Results for 50 Kpa Consolidation Pressure. . . . .	63
Table 4.12.	Sile CSS Test Results for 100 Kpa Consolidation Pressure. . . . .	65
Table 4.13.	Kilyos CSS Test Results for 50 Kpa Consolidation Pressure. . . . .	67
Table 4.14.	Kilyos CSS Test Results for 100 Kpa Consolidation Pressure. . . .	69
Table 4.15.	Kilyos CSS Test Results for 150 Kpa Consolidation Pressure. . . .	71
Table 5.1.	Circularity, Roundness and Critical State Friction Angle of Sand Types. . . . .	75
Table 5.2.	Circularity, Roundness, $\alpha_\psi$ and $m_\psi$ of Sand Types. . . . .	77
Table 5.3.	Comparing SRA Effects for CP=1 sec. . . . .	91
Table 5.4.	Comparing SRA Effects for CP=2 sec. . . . .	91
Table 5.5.	Comparing CP Effects for SRA=0.2 sec. . . . .	98
Table 5.6.	Comparing CP Effects for SRA=0.3 sec. . . . .	98

## LIST OF SYMBOLS

$A$	Cross sectional are
$A_0$	Initial sample are
$A_c$	Corrected sample are
$A_m$	Membrane are
$B$	Ratio of specimen pore pressure change to cell pressure change
$C$	Circularity
$D_C$	Specimen diameter
$D_F$	Fractal dimension
$e$	Void ratio
$e_{max}$	Maximum void ratio
$e_{min}$	Minimum void ratio
$E_m$	Young's modulus
$f$	Frequency
$F$	Force applied to stretch the specimen
$F_b$	Buoyancy force
$G_s$	Specific gravity
$h_a$	Initial specimen height
$h_c$	Specimen height after consolidation
$I_D$	Relative density
$I_D$	Relative density
$K_0$	Ratio of horizontal stress to vertical stress at-rest
$L$	Unstretched length
$L_{Major}$	Length of the major axis
$m_{\psi}$	Empirical constant value
$n$	Harmonic number
$p$	Perimeter
$p_a$	Atmospheric pressure
$p'$	Mean effective stress

$p'_i$	Pre-shear confinement pressure
$R$	Roundness
$t_{90}$	Time corresponding to 90% of primary consolidation
$t_m$	Membrane thickness
$V$	Volume
$W_s$	Dry unit weight
$\alpha_\psi$	Empirical Constant Value
$\beta_\psi$	Constant value depending on relative density
$\gamma'$	Shear strain ratio
$\gamma_s$	Dry unit weight
$\gamma_w$	Water unit weight
$\Delta h$	Height change
$\Delta h$	Length change
$\epsilon_1$	Axial strain
$\epsilon_2$	Radial strain
$\epsilon_3$	Radial strain
$\epsilon_v$	Volumetric strain
$\dot{\epsilon}_1$	Axial strain ratio
$\dot{\epsilon}_2$	Radial strain ratio
$\dot{\epsilon}_3$	Radial strain ratio
$\dot{\epsilon}_v$	Volumetric strain ratio
$\theta$	Angle between radii measurements in $R(\theta)$ method
$\sigma_c$	Cell pressure
$\sigma'_h$	Effective horizontal stress
$\sigma'_n$	Effective normal stress
$\sigma'_v$	Effective vertical stress
$\tau$	Shear stress
$\tau_f$	Shear stress at failure
$\phi_p$	Peak friction angle
$\phi_\mu$	Fundamental angle of friction

$\phi'$	Critical state friction angle
$\phi'_{cs}$	Critical state friction angle
$\psi$	Dilation angle
$\psi_p$	Peak dilation angle

## LIST OF ACRONYMS/ABBREVIATIONS

ASTM	American Society for Testing and Material
CD	Consolidated Drained
CP	Cyclic Period
CSR	Cyclic Stress Ratio
CSS	Cyclic Simple Shear
DEM	Discrete Element Modeling
FS	Factor of Safety
LM	Light Microscope
LPI	Liquefaction Potential Index
MDSS	Multidirectional Direct Simple Shear
NCL	Number of Cycles to Liquefy
NIH	National institute of Health
NNCL	Normalized Number of Cycles to Liquefy
PWP	Pore Water Pressure
SEM	Scanning Electron Microscope
SRA	Stress Ratio Amplitude
STDEV	Standard Deviation
SGI	Swedish Geotechnical Institute

# 1. INTRODUCTION

The importance of geotechnical investigation before, during and after construction has been known for decades now but the influences of microscopic properties of grains on their mechanical properties had not received enough attention due to lack of proper equipment, until almost recently. However, now that accurate image capturing devices and image processing software are more widespread, the relationship between different shape factors and soil properties can be inquired more effectively. In this study, two of the most influential grain shape factors, Circularity and Roundness, are investigated. Circularity and roundness values of individual grains are calculated through digital image processing of grain images captured by light microscopes.

This study attempts to investigate the influence of particle shape characteristics on the dilatant properties, and accordingly the liquefaction potential of cohesionless soils. Dilation is a term, initially used by Reynolds [1] back in 1885, expressing the tendency of dense granular material to expand under shear stress. Dilative property is influential on soil properties such as strength and stress-strain relationships. On the other hand, dilation potential of granular soils is dependent on a variety of properties such as relative density, mean effective stress, gradation, soil fabric and shape factors. These are the same factors that define the liquefaction risk for cohesionless soils. Therefore, there is an intrinsic link between dilation angle and liquefaction potential. Liquefaction on the other hand, is a phenomenon mostly seen in saturated loose sands, which intend to compress either during shearing or under the action of cyclic loading. Accordingly, this study investigates the influence of grain shape on the dilative properties and liquefaction potential. Therefore, the main goal is to investigate if there is a relationship connecting the shape factor to dilatancy and liquefaction susceptibility.

In this thesis a light microscope and a digital microscope camera (Mshot) were used to capture the particle images and an image processing software (ImageJ) was used to process the images and find circularity and roundness for each grain. Furthermore, Consolidated-Drained (CD) Triaxial tests were performed on 3 different sand types in order to define the necessary soil constants that will allow the computation of dilation angle based on relative density and mean effective stress. Also, Constant Volume Cyclic



Simple Shear tests were conducted to find liquefaction susceptibility of each sand type. Cyclic simple shear device is capable of simulating cyclic loading under un-drained condition. Therefore there will be a hypothetical excess pore water pressure generation as if the test was truly un-drained. The number of cycles at which the excess pore water pressure reaches initial vertical stress, so the effective vertical stress drop to zero, will identify the liquefaction susceptibility.

In general, at relatively low confinement levels, dense granular soils exhibit a dilative response when subjected to shear loading conditions [2]. A sand mass will undergo this coupled shear-dilation process due to packing changes that occur during cyclic loading [3]. Such phases of dilation can result in significant regain in shear stiffness and strength, as a result of instances of pore-pressure reduction.

## 2. LITERATURE REVIEW

### 2.1. Particle Shape Quantification

Investigating particle shape was of interest in geology field prior to geotechnical engineering field. Particle shape is considered to be the result of two main factors. First is the difference in transportation agents bringing the rock from its original place to deposit [4] and the second factor is the particle genesis itself (rock structure, mineralogy, hardness, etc.) [5].

There are three different scales used to describe particle morphology, shape or form, angularity or roundness, surface texture or roughness. Form or shape factor deals with the gross form of a particle (axis lengths, perimeter, surface area, volume, etc.) where angularity or roundness reflects the number and sharpness of corners [6]. According to Wadell [7] form and roundness are mutually independent factors. Moreover, surface texture or roughness provides details about the number, size and sharpness of the asperities along the particle surface and on the corners [6].

On the early stage of morphology measurements, standard two dimensional charts developed by Rittenhouse [8], Powers [9], Krumbein [10] and Krumbein and Sloss [11], were in use to compare each particle to the standardized shapes in the chart.

With progression in digital image capturing and processing, variety of mathematical definitions were suggested by different authors for circularity (2D form of sphericity) and roundness over years, which finally resulted in definitions suggested as:

Roundness

$$R = \frac{4A}{\pi L_{Major}^2} \quad (2.1)$$

Circularity

$$C = \frac{4\pi A}{p^2} \quad (2.2)$$

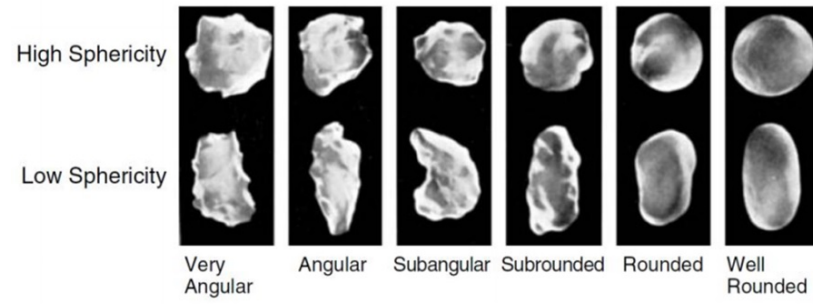


Figure 2.1. Powers [9] Qualitative Sphericity-Roundness Chart.

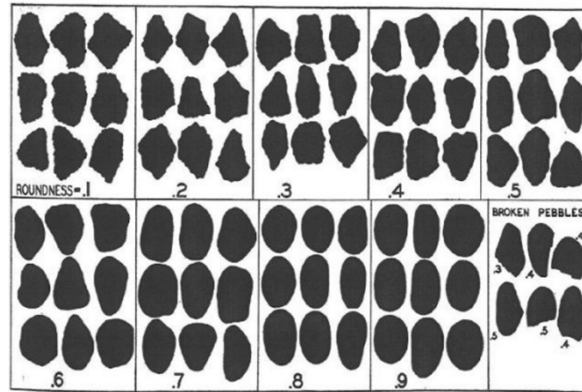


Figure 2.2. Krumbein [10] Comparison Chart for Roundness.

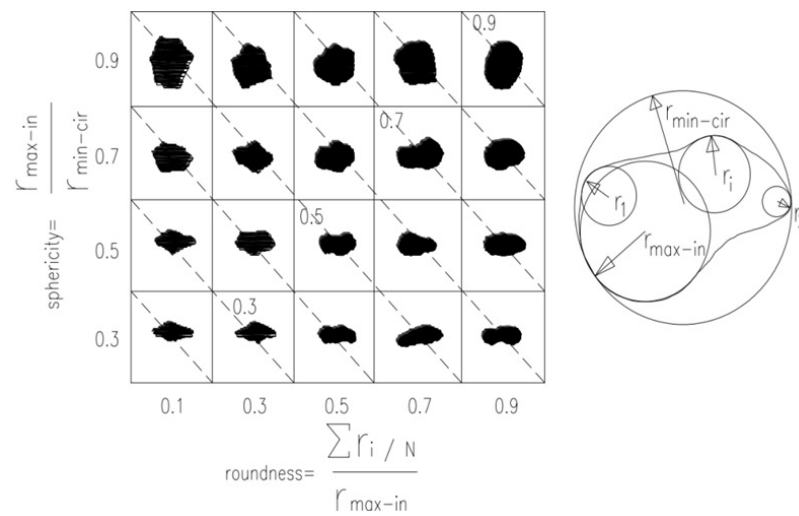


Figure 2.3. Krumbein and Sloss [11] Particle Roundness- Sphericity Chart.

Where  $P$  is the perimeter of the particle,  $A$  is the cross-sectional area, and  $L_{Major}$  is the length of the major axis.

Morphology which was defined as a “generalized method of representing and analyzing the structure of fine particles and their sets” [12], emerged as an analytical method to describe the form and shape of fine particles. Morphology includes the Fourier series representations as a first order approximation [12]. Fourier analysis of grain profiles correlates observed size and shape with mathematical relationships.

The  $(R, \theta)$  periodic function is most commonly used in representation by Fourier series and this technique. A profile is described by measuring the radii,  $R$ , at uniformly distributed values of  $\theta$ ,  $(0^\circ - 360^\circ)$ , measuring the angle between radii measurements. The grain profile is then unrolled to obtain a waveform. Then the characterization of shape derived from measured parameters is represented by a Fourier series and Fourier descriptors are used to describe the boundary of a grain. The  $R(\theta)$  method introduced by Ehrlich and Weinberg [13] represents the boundary of certain classes of particle in which  $R(\theta)$  is the radius of the particle boundary at the angle  $\theta$  [12].

$$\mathbf{R}(\theta) = a_0 + \sum_{n=1}^{\infty} (\mathbf{a}_n \cos n\theta + \mathbf{b}_n \sin n\theta) \quad (2.3)$$

Where

$$\mathbf{a}_0 = \frac{1}{2\pi} \int_0^{2\pi} R(\theta) d\theta \quad (2.4)$$

$$\mathbf{a}_n = \frac{1}{\pi} \int_0^{2\pi} R(\theta) \cos n\theta d\theta \quad n = 1, 2, 3, \dots \quad (2.5)$$

$$\mathbf{b}_n = \frac{1}{\pi} \int_0^{2\pi} R(\theta) \sin n\theta d\theta \quad n = 1, 2, 3, \dots \quad (2.6)$$

Where  $a(n)$  and  $b(n)$  are the Fourier coefficients and  $n$  is the harmonic number.

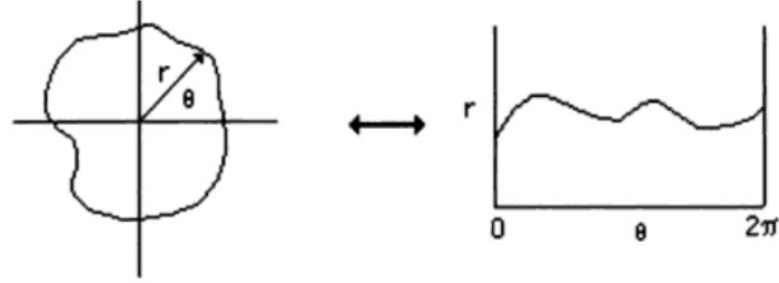


Figure 2.4. The  $R(\theta)$  Method.

The drawback of this methodology is the inability of correctly analyzing highly irregular [53] or re-entrant particles [55].

The fractal dimension,  $D_F$ , is a parameter that measures roughness and irregularity of a given profile. Kaye [16] defines the fractal dimension technique as the ability of a rugged boundary to occupy its void space. In two dimensional fractal analyses,  $D_F$  ranges from 1.0 to 2.0. For a perfectly straight line, DF is equal to 1.0, whereas DF approaches 2.0 for a jagged line. There are many methods to measure the fractal dimension like divider method and are-perimeter method from which the results confirm the importance of differentiating between textural and structural aspects of roughness.

## 2.2. Shear Strength and Dilation

Coulomb defined shear strength at failure as:

$$\tau_f = (\sigma'_n) \tan \phi' \quad (2.7)$$

Where  $\tau_f$  is the shear stress,  $\sigma'_n$  is the effective normal stress, and  $\phi'$  is the effective friction angle. However the linear failure envelope represents the soil at critical state

conditions. The critical state concept was proposed by Roscoe, Schofield and Wroth [17], and Schofield and Wroth [18], and is defined as the end or ultimate state of a deformation process, in which soil continues to shear under constant stress without volume change. Besides, critical state friction angle, which is constant for a given sand and depends only on the mineralogy of the sand grains, is defined as the friction angle of the soil shearing at a constant volume.

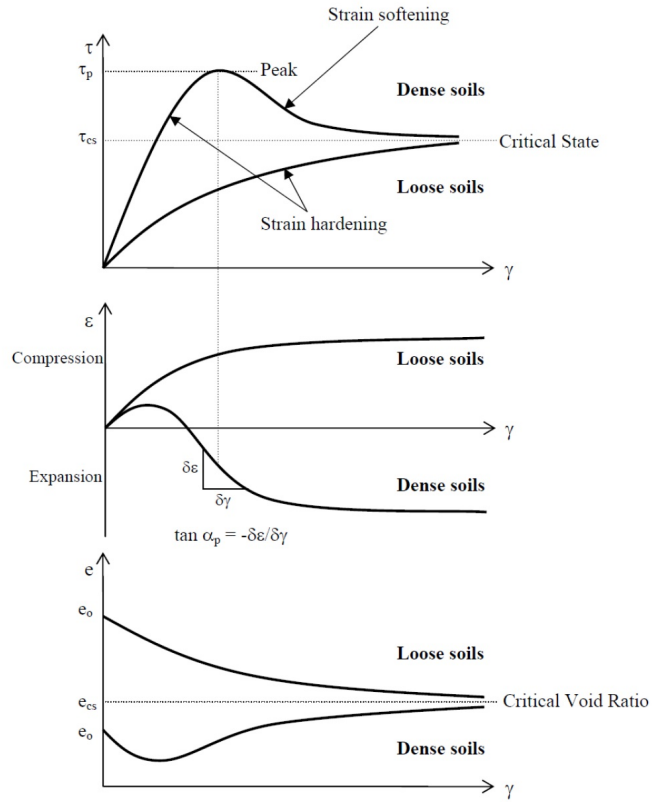


Figure 2.5. Typical Shearing Responses of Granular Soils [19].

A dense soil may contract slightly before granular interlock prevents further contraction, then the soil must dilate in order to continue shearing. Dilatancy is defined as the gradient of volumetric strain and shear strain change. Dilatancy angle ( $\psi$ ) can be calculated as:

$$\sin \psi = \frac{-(\dot{\epsilon}_1 + \dot{\epsilon}_2 + \dot{\epsilon}_3)}{\dot{\epsilon}_1 - \dot{\epsilon}_3} \quad (2.8)$$

Where  $\dot{\epsilon}_1$  is the strain rate in vertical direction,  $\dot{\epsilon}_2$  and  $\dot{\epsilon}_3$  are strain rates in horizontal directions.

Once the concept of dilatancy was known the Coulomb's frictional law was modified to:

$$\tau_f = (\sigma'_n)_f \tan(\phi'_{cs} + \psi_p) \quad (2.9)$$

Where  $\psi_p$  is the peak dilation angle.

In case of densely packed granular assemblies, since dilatant behavior should be

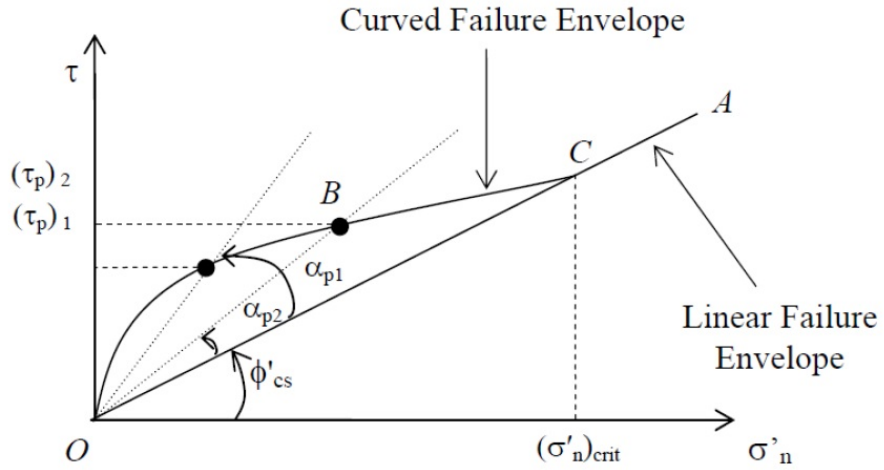


Figure 2.6. Dilatancy Effects on Coulomb's Failure Envelope [20].

overcome during shearing, peak strength is observed. Once this peak strength caused by dilation has been overcome through continued shearing, the resistance provided by the soil to the applied shear stress reduces (Strain Softening). Strain softening will continue until no further changes in volume of the soil occur during continued shearing. This condition is defined as the critical state.

Using the Mohr-Coulomb failure criterion, peak effective friction angle for cohesionless soil under axisymmetric triaxial or plane strain conditions can be determined as:

$$\phi'_p = \sin^{-1} \frac{(\sigma'_1 - \sigma'_3)}{(\sigma'_1 + \sigma'_3)} \quad (2.10)$$

Subscript  $p$  refers to peak conditions,  $\sigma'_1$  and  $\sigma'_3$  are the major and minor principal effective stresses respectively.

For the plane strain compression condition,  $\phi'_p$  is given by Bishop [60] as:

$$\phi'_p = \cos^{-1} \left[ \left( \frac{2\sigma'_2}{\sigma'_1 + \sigma'_3} \right)_p^{\frac{1}{2}} \right] \quad (2.11)$$

If the shearing is continued to very large shear strains, the shear strength drops below the critical state shear strength. This strength is called the residual shear strength and the friction angle corresponding to this strength is the residual friction angle of the soil [22].

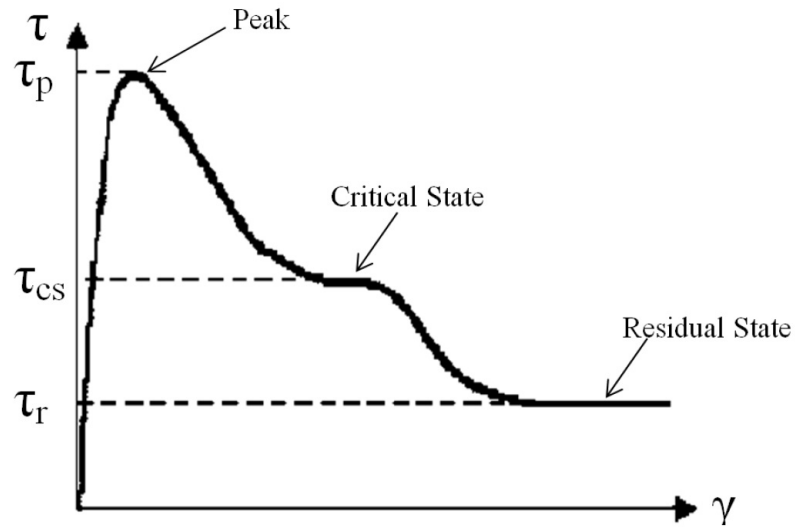


Figure 2.7. Peak, Critical and Residual State of the Soil During Shearing.

These three stages can only be observed in soils that contain sufficient amount of plate-like particles [23]. For soils that are dominantly composed of rotund particles, the residual strength is equal to critical state strength.

### 2.3. Relationship Between Friction and Dilatancy Angles

The simplest, but crudest way to explain and understand the relationship between critical state friction angle, dilation angle and peak friction angle is to use the



Coulomb's frictional law where:

$$\tau_f = (\sigma'_n)_f \tan(\phi'_{cs} + \psi_p)$$

Then assuming that the above equation is valid, the friction angle at failure could be calculated as:

$$\phi'_p = \phi'_{cs} + \psi_p \quad (2.12)$$

However, as it will later be shown in this thesis, real relationship between  $\phi'_p$ ,  $\phi'_{cs}$  and  $\psi_p$  is different from that shown in the above equation. Taylor [24] attempted to explain the influence of dilatancy angle on peak friction angle in terms of energy dissipation rate. Assuming the input and dissipated work in a simple shear sample:

$$\dot{W} = \sigma'_n \dot{\epsilon}_v + \tau \dot{\gamma} = (\tan \phi'_{cs}) \sigma'_n \dot{\gamma} \quad (2.13)$$

Then knowing  $\tan \phi = \frac{\tau}{\sigma'_n}$  and  $\tan \psi = -\frac{\dot{\epsilon}_v}{\dot{\gamma}}$  the equation can be written as:

$$\tan \phi' = \tan \phi'_{cs} + \tan \psi \quad (2.14)$$

Rowe [25] examined the properties of regular assemblies of spheres and assumed that sliding takes place on a saw-toothed plane and stress, strain ratios are functions of  $\alpha$  and  $\beta$  angles.

The functions are such that  $\alpha$  can be eliminated to give the following equation:

$$\frac{\sigma'_1}{\sigma'_3} = \frac{\tan(\phi_\mu + \beta) - \dot{\epsilon}_3}{\tan \beta} \frac{\dot{\epsilon}_1}{\dot{\epsilon}_3} \quad (2.15)$$

Then assuming minimum energy hypothesis, which supposes that the energy ratio during deformation varies with particle arrangement with its minimum value corresponding

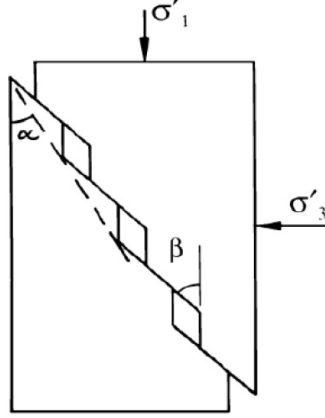


Figure 2.8. Assumed Sliding Mechanism for Rowe's Stress Dilatancy Relationship [25].

to particular deformation state,  $\beta$  is determined as:

$$\beta = \frac{\pi}{4} - \frac{\phi_\mu}{2} \quad (2.16)$$

And the equation will be:

$$\frac{\sigma'_1}{\sigma'_3} = \tan^2 \left( \frac{\pi}{4} - \frac{\phi_\mu}{2} \right) \left( \frac{-\dot{\epsilon}_3}{\dot{\epsilon}_1} \right) \quad (2.17)$$

Where  $\phi_\mu$  is the fundamental angle of friction for grain to grain contact.

De Josselin de Jong [26] showed that it is possible to derive Rowe's [25] dilatancy expression without assuming energy principles, only by using friction laws.

$$\sin \alpha = \left( \frac{\frac{\delta \epsilon_1}{K \delta \epsilon_3} + 1}{\frac{\delta \epsilon_1}{K \delta \epsilon_3} - 1} \right) \quad (2.18)$$

Where  $\alpha$  is the dilation angle,  $k = 1$  for plane strain and  $k = 2$  for triaxial loading conditions.

Bolton [27] analyzed the strength and dilatancy of 17 sand types under axisymmetric and plane strain conditions at different densities for various confining pressures. He derives empirical relationships for dilatancy as:

Plane Strain Conditions:

$$\phi'_{max} - \phi'_{critical} = 0.8\psi = 5I_R \quad (2.19)$$

Triaxial condition:

$$\phi'_{max} - \phi'_{critical} = 0.8\psi = 3I_R \quad (2.20)$$

Where  $I_R$  is the relative density index defined as:

$$I_R = I_D (Q - \ln p') - R \quad (2.21)$$

Where  $I_D$  is the relative density,  $p'$  is the mean effective stress at peak. Bolton determined that  $Q = 10$  and  $R = 1$  create a good definition for all test results. Bolton [27] also determined the following relationship applicable for both triaxial and plane strain loading conditions:

$$\left( -\frac{d\epsilon_v}{d\epsilon_1} \right)_{max} = 0.3I_R \quad (2.22)$$

Where  $\left( -\frac{d\epsilon_v}{d\epsilon_1} \right)_{max}$  is a measure of dilatancy rate in triaxial test.

Based on plasticity concepts, Vermeer and de Borst [28] defined the dilation angle by:

$$\psi = \sin^{-1} \left( \frac{\dot{\epsilon}_p}{-2\dot{\epsilon}_1 + \dot{\epsilon}_p} \right) \quad (2.23)$$

Then in 1996 Schanz and Vermeer [29] developed the following relationship relating the relative density index and dilatancy angle based on Rowe's theory [25] and Bolton's theory [27]:

$$\psi = \sin^{-1} \left( \frac{I_R}{6.7 + I_R} \right) \quad (2.24)$$

Where  $I_R$  is the relative dilatancy index defined by Bolton [27].

They also supported the assumption that dilatancy angle resulted from plain-strain and triaxial tests are almost the same. They suggested the following equation for calculation of dilatancy angle in triaxial testing:

$$\sin \psi = -\frac{\frac{\dot{\epsilon}_v}{\dot{\epsilon}_1}}{2 - \frac{\dot{\epsilon}_v}{\dot{\epsilon}_1}} \quad (2.25)$$

Cinicioglu and Abadkon [30] conducted conventional drained triaxial compression tests consolidated under  $K_0$  condition to investigate the uncoupled effects of preshear mean effective stress ( $p'_i$ ) and volumetric state as defined by preshear relative density  $I_D$  on peak dilation angle  $\psi_p$ . They grouped the test results into several small  $I_D$  ranges showed that for constant  $I_D$  values,  $\frac{p'_i}{p_a}$ - $\tan \psi_p$  relationship is linear.

$$\tan \psi_p = \alpha_\psi \left( \frac{p'_i}{p_a} \right) + \beta_\psi \quad (2.26)$$

Where  $\beta_\psi$  is a constant value depending on  $I_D$ , So the equation above can be written as:

$$\tan \psi_p = \alpha_\psi \left( \frac{p'_i}{p_a} \right) + m_\psi I_D \quad (2.27)$$

Where  $\alpha_\psi$  and  $m_\psi$  are empirical constants which can be obtained by conducting a few triaxial tests.

#### 2.4. Influence of Particle Shape on Soil Strength and Dilatancy

In recent years, particle shape analysis has been improved significantly due to the development in image capturing techniques and image processing methods. Shape has a pronounced effect on the engineering properties of granular soils. Holubec and D'Appolonia [31] analyzed results of tests on four granular materials with particles in the medium to fine sand and suggest that strength, as measured by friction angle,

increased with increasing angularity.

According to Rowe's equation [25]:

$$\frac{\sigma'_1}{\sigma'_3 \left(1 + \frac{d\dot{V}}{V\dot{\epsilon}_1}\right)} = \tan^2 \left(45 + \frac{\phi_f}{2}\right) \quad (2.28)$$

Where  $\frac{d\dot{V}}{V}$  is volumetric strain,  $\dot{\epsilon}_1$  is axial strain and  $\phi_f$  is defined as:

$$\phi_f = \kappa \tan \phi_\mu \quad (2.29)$$

Where  $\phi_\mu$  is the true angle of friction between the mineral surfaces of the particles. The value of  $\phi_\mu$  depends on the nature of the mineral, the properties of its surface, roughness and on the size of the load per particle [32]. Besides  $\kappa$  is a coefficient which increases with degree of remoulding and associated energy loss. Ng [33] examined the effects of particle shape and stress path using drained and undrained (constant volume) triaxial tests. The friction angles obtained from the specimens composed of two different ellipsoidal types were higher than those of the mono-size specimens.

Alshibli and Alsaleh [34] conducted a detailed analysis of the surface roughness, roundness, and sphericity of three different sizes of silica sands using digital microscopy. They found that as the surface roughness increases, the friction and dilatancy angles of the sands also increase.

Cho *et al.* [35] determined that a decrease in sphericity and/or roundness leads to increase in  $e_{max}$  and  $e_{min}$ , decrease in small-strain stiffness and increase in sensitivity to state of stress, increase in compressibility under zero-lateral strain loading, increase in  $\phi'_{cs}$ , and increase in the critical state line intercept.

Guo and Su [36] researched the effect of particle angularity on the strength and dilation of granular materials. They determined that particle angularity has a significant influence on the peak friction angle and dilatancy, however no correlation was developed.

Cox [19] used a weighted factor analysis combining six main grain shape parameters, Circularity, Roundness, Compactness, ModRatio, Sphericity, and Aspect Ratio into

the Weighted Single Sand Shape Factor, WSSSF. The correlation was given as below:

$$\frac{\left(\frac{\psi_p}{\phi'_{cs}}\right)}{I_D} = -0.117 \ln \left( \frac{\alpha'_n}{p_a} \times WSSSF \right) + 0.457 \quad (2.30)$$

Where  $I_D$  is relative density,  $\phi'_{cs}$  is critical state friction angle,  $\psi_p$  is peak dilation angle,  $\sigma'_n$  is effective vertical stress and  $p_a$  is atmospheric pressure.

## 2.5. Liquefaction and Liquefaction Potential

Soil liquefaction is one of the major causes of earthquakes related damages for structures resting in or on saturated or partially saturated soils. The term “Liquefied” was first used by Hazen [37] in soil mechanics field, referring to the 1918 failure of the Calaveras Dam in California. Although the effects of liquefaction have been long understood, it was more thoroughly brought to the attention of engineers after the 1964 Niigata earthquake and 1964 Alaska earthquake.

Liquefaction Potential Index ( $LPI$ ) was originally developed in Japan to estimate the potential of liquefaction to cause foundation damage at a site [38]. It was assumed that the severity of liquefaction is proportional to thickness of the liquefied layer, proximity of the liquefied layer to the surface and amount by which the factor of safety ( $FS$ ) is less than 1.0, where ( $FS$ ) is defined as below:

$$FS = \frac{\text{Cyclic Resistance Ratio}}{\text{Cyclic Stress Ratio}} \quad (2.31)$$

$$\text{Cyclic Stress or Resistance Ratio} = \frac{\tau_{cyclic}}{\sigma'_1} \quad (2.32)$$

Where  $\sigma'_1$  is effective vertical stress.

$$\mathbf{LPI} = \int_0^{20m} Fw(z)dz \quad (2.33)$$

Where  $z$  is depth in meter and  $w(z) = 10 - 0.5z$ , also:

$$FS \leq 1 \longrightarrow F = 1 - FS$$

$$FS > 1 \longrightarrow F = 0$$

Iwasaki [39] concluded that severe liquefaction is likely at sites with  $LPI$  greater than 15 and that severe liquefaction is unlikely at sites with  $LPI$  less than 5.

Studying liquefaction, two main values should be determined, the dynamic loading caused by earthquake, which is quantified as cyclic stress ratio ( $CSR$ ), and soil liquefaction resistance, quantified as cyclic resistance ratio at a specific magnitude of earthquake ( $CRRM$ ). These parameters were outlined by Seed and Peacock [40] and later improved by Seed [41], and Seed *et al.* [42] [43]. The  $CSR$  is the ratio of the shear stress generated by the earthquake to the vertical effective stress at the desired depth. The  $CRRM = 7.5$  is the ratio of the cyclic resistance to liquefaction to vertical effective stress at an earthquake with magnitude 7.5. Liquefaction at a given depth is expected to occur when  $CSR > CRRM = 7.5$  at that depth [44].

## 2.6. Influence of Particle Shape on Liquefaction Susceptibility

Ishibashi *et al.* [45] have shown that the resistance to liquefaction increases with increase in particle angularity. Their observations are, however, restricted to relatively low levels of confining stresses.

Vaid *et al.* [46] investigated two medium sands with essentially identical gradations, one angular and the other rounded. They concluded that the decrease in resistance with confining pressure increases with increase in relative density and is larger for angular sand than for rounded sand. At low confining pressures, angular sand is considerably more resistant to liquefaction than rounded sand over the entire range of relative densities.

Inherent factors affecting the flow behavior of sands include grain size, size distribution, shape, angularity, and surface roughness. Extrinsic factors include void ratio, fabric, initial effective stresses, and stress path [6].

Ashour and Norris [48] suggested a formulation for assessing the drained and undrained rebounded response of sand for use in assessment of its undrained behavior. The formulation presented is a function of the void ratio, confining pressure, and basic properties of sand, such as relative density, uniformity coefficient, and roundness, which are typically available to the designer or can be obtained from visual inspection. The developed formulas allow one to predict the potential of sand to liquefy, the extend of liquefaction (limited or complete liquefaction) or dilative behavior, the peak and residual strength values, as well as the whole undrained stress-strain curve and effective stress path.

Considerable studies on liquefaction behaviour of granular materials have been done using discrete element method by Sitharam [49], Dinesh [50], Vinod [51], but in all these studies the investigated particles were spherical. The significance of particle shape effect on the engineering properties of soil was highlighted by Ashmawy *et al.* [52]. They used Discrete Element Modeling (*DEM*) method to simulate cyclic shear tests as a result of which at the maximum void ratio, the susceptibility to liquefaction was independent of particle shape. However, they stated that the influence of particle morphology on liquefaction susceptibility was significant in the case of sands prepared at the same void ratio.

## 2.7. Imaging Techniques for Defining Particle Shape

Light microscope, LM, has been used in studies examining grain shape (Vallejo, [53]; Sukumaran and Ashmawy, [6]; Gori and Mari, [54] as well as the Scanning Electron Microscope, SEM, (Bowman *et al.*, [55]; Whalley and Orford, [56]; Thomas *et al.*, [57]. Using a SEM, both grain shape and the surface of a particular grain can be observed due to the significant magnification abilities of SEM. However, it is an expensive apparatus to use and relatively difficult to perform tests with. On the other hand, LM is low in cost and simple to work with. Besides, considering that the concentration of this study is on the shape and not the surface characteristics of particles, LM seems sufficient to make use of.

The camera which was used to capture the images was an Mshot brand, MD50 model digital microscope camera.



## 2.8. Image Processing Software

The image processing program used in this study was ImageJ [58]. It is a Java based open sourced image-processing tool adapted from an earlier Macintosh version of the National Institute of Health (NIH) Image program. This program is available over the public domain and is able to assess numerous image formats with numerous built-in editing and analyzing tools. This program has many advantages such as high speed, easy conversion of picture to binary format, attribution of a specific number to each processed particle and easy modification of image's brightness/contrast, threshold, and color balance.

According to thorough investigation performed by Cox [19], one of the most accurate ImageJ plugins is Shape Descriptors. This plugin [59] uses the following formulas to calculate circularity and roundness:

$$Roundness = \frac{4A}{\pi L_{Major}^2}$$

$$Circularity = \frac{4\pi A}{p^2}$$

## 2.9. Triaxial Testing History

Bishop and Hankel [60] suggested the conventional triaxial apparatus as a simple apparatus for which the preparation of cylindrical samples are relatively easy.

Triaxial apparatus has the outstanding advantage of controlling the drainage and measuring pore pressure. Terzaghi [61] was the first to perform triaxial test on fine-grain under controlled condition of drainage, and Rendulic [62] was the first to measure the pore pressure in triaxial tests conducted on clay.

Over the years, there have been significant developments in triaxial apparatus due to progress in microcomputers and control systems. In 1983, Hight [63] developed an accurate control system which was capable of applying specified stress and strain steps to the samples in various test equipment such as hydraulic triaxial apparatus [64].

Atkinson [65] and Atkinson *et al.* [66] developed microcomputer controlled stress path equipment. This equipment controls a standard hydraulic stress path cell for samples with conventional instrumentation monitored by a simple transducer reading device. Siddique *et al.* [67] developed a fully automated computer controlled testing system for triaxial stress and strain path tests, which was capable of controlling both stress and strains imposed on the specimen.

In this study, the GeoComp LoadTrac II and FlowTrac II system was used which for triaxial testing fully automates the conduct of CU, CD and any possible stress path triaxial test on soils. Once a soil sample is in place, and the test conditions are selected, the system will run the entire triaxial test from start to finish. This system is operated by software which automates the initialization, saturation, consolidation (isotropic, anisotropic, or  $K_o$ ) and shear phases of the test.

## 2.10. Cyclic Simple Shear Test History

The first direct simple shear test equipment was built in Swedish Geotechnical Institute (SGI) in 1936. This device confined specimens using a rubber membrane and tightly placed aluminum rings, and it was capable of uniformly deform a soil specimen in pure shear.

Later in 1953, a device was designed that used a square box for sand specimens, at the University of Cambridge. This experimental device was the first of many apparatuses developed at University of Cambridge in future years.

None of these devices were capable of performing truly undrained tests since no back pressure could be applied for full saturation. Franke [68] and Dyvik [69] developed Direct Simple Shear device, testing samples enclosed in a pressurized cell to ensure a full saturation of the sample and accurate pore pressure measurements. In the 1960's the Norwegian Geotechnical institute (NGI) created a device that was able to strain in simple shear after vertical loading using a rubber membrane reinforced with a wound wire encased by the rubber [70]. DeGroot *et al.* [71] developed an automated electrop-

neumatic control system for conducting undrained direct simple shear tests on cohesive soils and DeGroot *et al.* [72] applied further changes to the apparatus and described the new multidirectional direct simple shear (MDSS) apparatus which was direct simple shear device that had the unique capability of applying two independent horizontal shear stresses to a circular soil specimen.

With software and control systems progress, various companies have produced fully automated test devices with precise input and output data. GeoComp ShearTrac II-DSS system is one of the best Direct Simple Shear test apparatuses presently available. It is a universal shear system capable of performing the consolidation, static and cyclic direct simple shear phases under full automatic control. This system is of the type developed at NGI in the mid- 1960's.

### **2.11. Simulating Undrained Condition with Constant Volume Condition**

GeoComp Shear Trac II-DSS is capable of running the shearing phase either under constant load or constant volume condition. Constant load test would mean maintaining a constant vertical load on the top cap during the shearing which simulates the drained condition. Constant volume test would mean maintaining a constant volume condition simulating the undrained condition. This option is especially of importance for cyclic loading.

Bjerrum and Landva [73] proposed this equivalence between the two tests and furthermore, stated that the change in vertical stress observed in a constant volume test is similar to the change in pore pressure that would have occurred in a constant load undrained test. Also Dyvik *et al.* [69] designed a chamber for the NGI Direct Simple Shear device to validate the “constant volume” hypothesis. The chamber provided the capability of performing truly undrained tests and measuring the pore pressure inside the soil specimen. The authors compared truly undrained tests and constant volume drained test results on normally consolidated clay and obtained very similar results in both case.

### 3. METHODOLOGY

#### 3.1. Shape Factor Analysis

The image processing program used in this study is ImageJ [58]. It is a Java based open sourced image-processing tool adapted from an earlier Macintosh version of the National Institute of Health (NIH) Image program.

Pictures were taken using an Mshot brand, MD50 model digital light microscope camera. Care was taken to prevent particles to overlap while capturing the images, so the processing would be easier and more precise (Figure 3.1). Then the captured images were processed using ImageJ software. Then using ImageJ unclear particles were discarded from the images and the rest were taken into account for shape factor analysis. The shape descriptor plugin was used in this study to obtain circularity and roundness values. Cox [19] used a simple circle to investigate differences in the shape parameters from the two plugins of ImageJ as compared to the theoretical values associated with a circle. Both manually sketched circle and “Circle Test” plugin [74], which automatically draws a circle of radius 60 pixels in an image of size 324 pixels x 200 pixels, to investigate the outcome values was used. The discrepancy between the plugins and the theoretical value in Circularity is more than roundness. A difference of about 10% lower is observed in the plugins values as compared to the theoretical.

Table 3.1. Comparison of Theoretical and Predicted Shape Parameter Values [19].

<b>Grain Shape Parameter</b>	<b>Manual</b>	<b>Plugin</b>	<b>Theoretical</b>
<b>Circularity</b>	0.908	0.910	1.000
<b>Roundness</b>	1.000	1.000	1.000

Each image was turned into binary as shown in Figure 3.2 since ImageJ is only capable of processing this type of picture.

The program ascribes a label to each particle, and any other dark stain in the picture

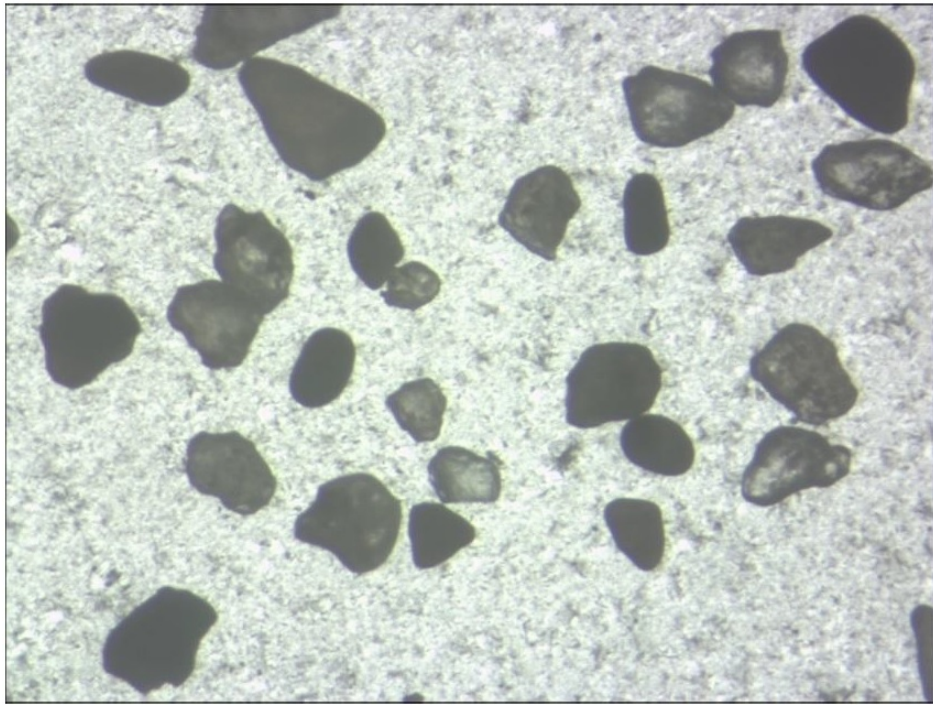


Figure 3.1. Example Image of Akpinar Sand Particles.



Figure 3.2. Example Binary image of Akpinar Sand Particles.

(Figure 3.3), and calculates the necessary parameters, like area, perimeter and circularity for each slice(Figure 3.4).

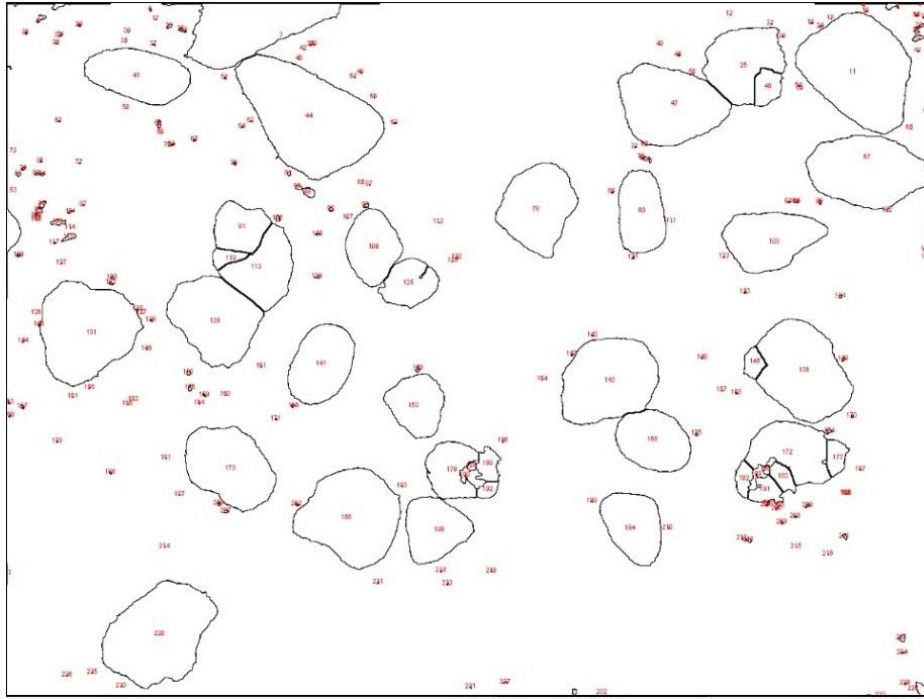


Figure 3.3. Example Image of Numbers Ascribed to Akpinar Sand Particles.

Single particle values of 1-1							
File Edit Font							
Slice	Particle	Area	Perimeter	Angle	Form Factor	Round	Comp
1	1	1506.00	393.34	79.59	0.12	0.60	0.78
1	2	385.00	134.08	14.24	0.27	0.61	0.78
1	3	11567.00	1148.09	0.89	0.11	0.29	0.54
1	4	3496.00	839.40	176.98	0.06	0.15	0.39
1	5	9534.00	506.15	5.77	0.47	0.46	0.68
1	6	6645.00	475.32	91.91	0.37	0.74	0.86
1	7	4.00	7.66	90.00	0.86	0.68	0.83
1	8	24052.00	629.70	39.35	0.76	0.78	0.88
1	9	69.00	38.04	91.69	0.60	0.44	0.67
1	10	8.00	10.49	162.70	0.91	0.70	0.83

Figure 3.4. Example ImageJ Output Table.

Since the program calculates the value of each shape parameter for every particle, clear or unclear, the clear particles were chosen manually. Then the circularity and roundness values for chosen particles from all the captured pictures were gathered in an excel file.

Table 3.2. Number of Analyzed Particles.

<b>Number of Particles</b>	<b>Mean C</b>	<b>Mean R</b>	<b>C STDEV</b>	<b>R STDEV</b>
<b>15</b>	0.716	0.708	0.053	0.137
<b>25</b>	0.716	0.723	0.040	0.1162
<b>50</b>	0.716	0.728	0.042	0.110
<b>75</b>	0.710	0.724	0.051	0.124
<b>100</b>	0.716	0.719	0.049	0.119
<b>125</b>	0.717	0.717	0.048	0.115
<b>150</b>	0.720	0.717	0.048	0.116
<b>175</b>	0.722	0.717	0.048	0.112
<b>200</b>	0.721	0.718	0.049	0.109
<b>225</b>	0.724	0.726	0.049	0.112
<b>250</b>	0.723	0.726	0.052	0.115
<b>275</b>	0.722	0.724	0.051	0.116
<b>300</b>	0.723	0.724	0.052	0.119
<b>325</b>	0.720	0.720	0.063	0.122
<b>350</b>	0.722	0.723	0.062	0.121

Processing images of 350 individual particles showed that using the average circularity and roundness values of 50 particles would correspond to the minimum Standard Deviation for both parameters. So 50 was the number of particle processed for each sand type.

### 3.2. Triaxial Testing Program

Vaid *et al.*, [46] studied the effect of relative density and confinement pressure on liquefaction using CSS apparatus. According to their test results, both parameters, relative density and confinement pressure, affects the liquefaction potential of a specimen. Also they realized that a considerable densification, particularly of angular sand, inevitably occurs under the application of large confining pressure. Because of this dependence of relative density on confining pressure, the influence of relative density and confining pressure on resistance to liquefaction cannot be isolated easily. In this study, dilation angle calculated using Cinicioglu and Abadkon [30] relationship, which is a parameter depending on both relative density and confinement pressure, is used as a liquefaction susceptibility indicator.

Triaxial tests were conducted on samples that have different combinations of relative density and pre-shear mean effective stress. Results are used to calculate the constants,  $\alpha_\psi$  and  $m_\psi$ , Proposed by Cinicioglu and Abadkon [30]. This process was repeated for each sand type. Equation that was used for calculating the dilatancy angles of samples is given below [30]:

$$\tan \psi_p = \alpha_\psi \left( \frac{p'_i}{p_a} \right) + m_\psi I_D$$

Each triaxial test was conducted under  $K_0$  consolidated drained condition on normally consolidated samples. All tests were performed according to ASTM (D7181) standard in an automated triaxial testing apparatus.

The  $\alpha_\psi$  and  $m_\psi$  values for Akpınar sand, were already calculated by Altunbas [75] with the exact same method.



Table 3.3. Sile Sand Triaxial Testing.

Test No	$\sigma'_1 (kPa)$	$p'_i (kPa)$	$I_D$	$K_0$
1	100	63.1	0.61	0.446
2	100	69.7	0.54	0.545
3	100	66.1	0.5	0.492
4	200	107.4	0.5	0.305
5	250	153.1	0.96	0.419
6	150	90.5	0.58	0.405
7	250	118.1	0.73	0.270

Table 3.4. Kilyos Sand Triaxial Testing.

Test No	$\sigma'_1 (kPa)$	$p'_i (kPa)$	$I_D$	$K_0$
1	150	94.3	0.66	0.441
2	250	185	0.39	0.610
3	300	160.3	0.45	0.299
4	200	128.5	0.51	0.467
5	225	120.6	0.39	0.294
6	250	133.4	0.48	0.298
7	200	135.7	0.69	0.518

### 3.3. Automated Triaxial Testing Apparatus

In this study, the GeoComp LoadTrac II and FlowTrac II system was used which consists of two automatic flow pumps and a computer controlled loading frame. This apparatus fully automates the conduction of UU, CU, CD and any possible stress path triaxial tests on soils. Once a soil sample is in place, and the test conditions are selected, the system will run the entire triaxial test from start to finish. This system is operated by software which automates the initialization, saturation, consolidation (isotropic, anisotropic, or  $(K_o)$ ) and shear phases of the test.



Figure 3.5. Automatic Triaxial System.

Loading frame, also called load trac, both controls the load applied on the specimen and

measures the displacement during the test. Automatic flow pumps, intelligent units composed of a flow pump, a pressure sensor and a control board, regulate pressure and volume cell and sample. Flow tracs house precision micro stepper motors that move pistons in cylinders filled with water. Pressure transducers determine the signals being sent to the stepper motor and the number of motor steps is used to calculate the volume changes. Pressure increments can increase and decrease in any pattern by any amount. The count readings from sensors are converted to engineering units using the calibration factors.

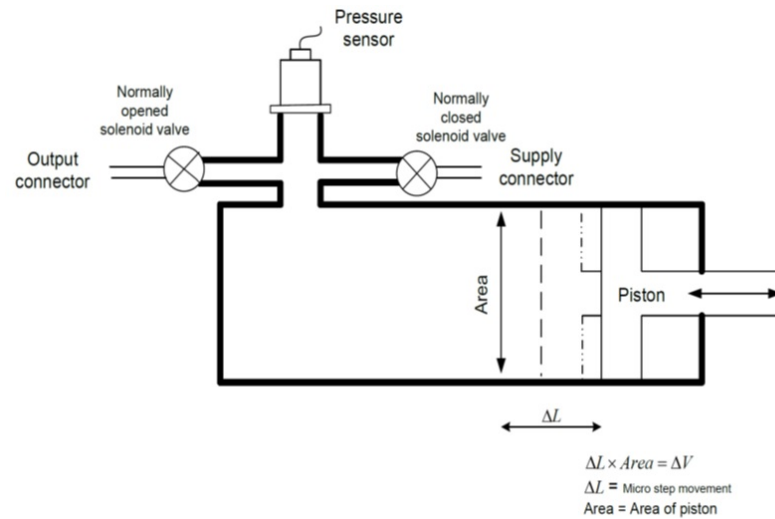


Figure 3.6. Schematic of a Flow Trac Unit [22].

### 3.3.1. Triaxial Testing Procedure

In this study triaxial tests were conducted in four stages:

(i) Initialization:

During initialization phase small magnitudes of horizontal stress, vertical stress and pore pressure are applied to the specimen for about 20 minutes. This phase controls the propriety of apparatus functions.

(ii) Saturation Phase:

In saturation phase cell and pore pressures are raised incrementally while effective

stress on the specimen is kept constant in order to achieve the maximum saturation ratio. According to ASTM (D-7181) pore pressure parameter (B ratio) is obtained from the following equation:

$$B = \frac{\Delta u}{\Delta \sigma_3} \quad (3.1)$$

Where  $\Delta u$  is the change in the specimen pore pressure that occurs when cell pressure changes and specimen drainage valves are closed and  $\Delta \sigma_3$  is the change in cell pressure. A minimum value of 0.95 was achieved for all experiments.

(iii) Consolidation Phase:

The apparatus consolidates the specimen under  $K_0$  condition. It automatically prevents the lateral straining by adjusting cell pressure. At rest earth pressure coefficient of sand samples could be monitored during the whole consolidation phase and it is calculated as:

$$K_o = \frac{\sigma'_h}{\sigma'_v} \quad (3.2)$$

Where  $\sigma'_h$  is the effective horizontal stress and  $\sigma'_v$  is the effective vertical stress.

(iv) Shearing Phase:

In this stage samples were sheared under drained conditions by increasing the vertical stress with the constant strain rate of  $(2.5 \times 10^2) \% / \text{min}$ . According to ASTM (D- 7181) shear strain rate has been obtained from the following equation.

$$\dot{\epsilon} = \frac{4\%}{10t_{90}} \quad (3.3)$$

Where  $\dot{\epsilon}$  is the shear strain rate and  $t_{90}$  is the time corresponding to 90% of primary consolidation. The maximum axial strain reached during shearing was 18% and the critical state of each sample was discernible.

### 3.3.2. Sample Preparation

The samples were prepared with the air pluviation technique. In this method a funnel, together with a tube when higher relative density is needed, is used. Sand falls through the funnel inside the membrane from a constant height. The height is decided according to the needed relative density. The higher the falling height gets, the denser the specimens become. Also vibration was applied in order to achieve denser specimens.

### 3.3.3. Test Corrections

There are 3 important corrections that should be applied to the triaxial test results:

(i) Piston Area Correction:

Buoyancy force pushes the piston upward while the piston is applying vertical load to the sample. Effective area of the piston should be measured to account for the buoyancy force effect. For this purpose, the cell is filled with water and pressure is applied to piston. The buoyancy force can be calculated as:

$$F_b = 0.153\sigma_c + 6.25 \quad (3.4)$$

Where  $F_b$  is the buoyancy force in Newtons and  $\sigma_c$  is the cell pressure in  $kPa$ . Calculated buoyancy force should be subtracted from the total load value.

(ii) Rubber membrane correction:

Thickness of the membrane restraint can influence the radial stress applied on the sample. According to ASTM (D-4767), the following equation is used to correct the principal stress difference for the effect of rubber membrane:

$$\Delta(\sigma_1 - \sigma_3) = \frac{4E_m t_m \epsilon_1}{D_c} \quad (3.5)$$

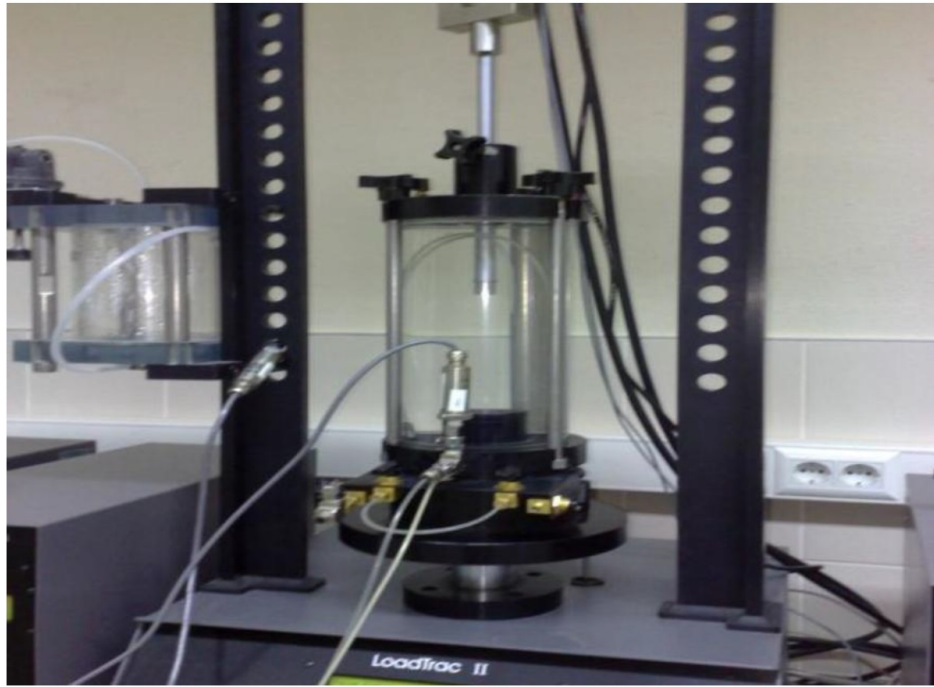


Figure 3.7. Piston Area Correction Test (Abadkon, 2012).

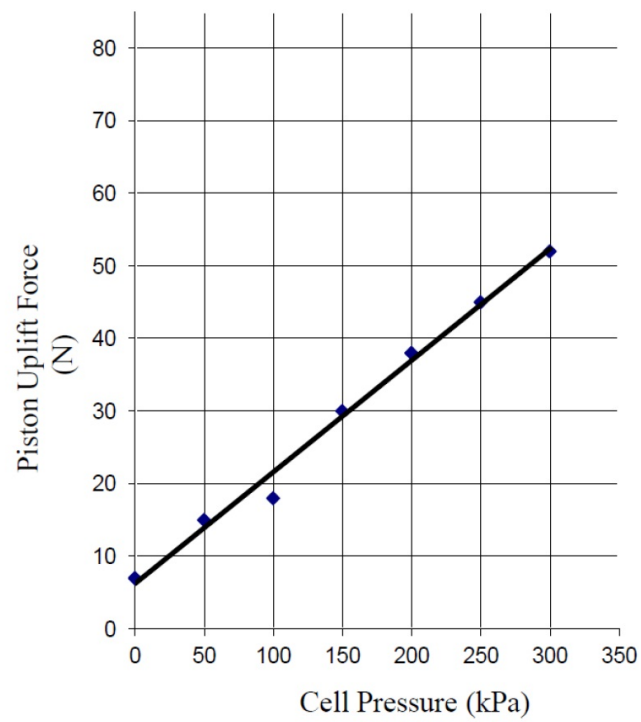


Figure 3.8. Variation of Uplift Force With Cell Pressure (Abadkon, 2012).

where  $\Delta(\sigma_1 - \sigma_3)$  is the correction to be subtracted from the measured deviator stress,  $D_c$  is the diameter of the sample after consolidation,  $E_m$  is the young's modulus for the membrane material,  $t_m$  is the membrane thickness and  $\epsilon_1$  is the axial strain.

$E_m$  can be calculated as follows:

$$E_m = \frac{\frac{F}{A_m}}{\frac{\Delta L}{L}} \quad (3.6)$$

Where  $F$  is the force applied to stretch the membrane,  $L$  is unstretched length of the membrane,  $\Delta L$  is the length change of the membrane and  $A_m$  is the area of the membrane.

(iii) Sample Area Correction:

There are two kinds of sample area correction depending on the sample shape during the shearing phase:

- Uniform area correction
- Parabolic area correction

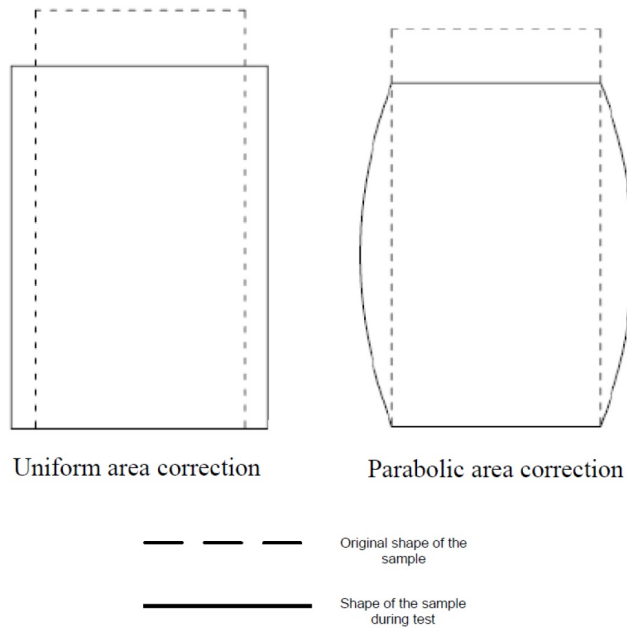


Figure 3.9. Two Different Area Corrections According to Sample Shape.

In this study, the specimens were all parabolically shaped during the shearing, so the equation below was used to correct the area change in vertical stress calculation:

$$A_c = A_0 \frac{1 - \epsilon_v}{1 - \frac{5}{3}\epsilon_1} \quad (3.7)$$

Where  $A_c$  is the corrected sample area,  $A_0$  is the initial area of the sample,  $\epsilon_v$  is the volumetric strain during shearing and  $\epsilon_1$  is the axial strain.

Axial strain is calculated as follows:

$$\epsilon_1 = \frac{\Delta h}{h_c} \quad (3.8)$$

Where  $\Delta h$  is the change in height of the specimen during loading  $h_c$  is the height of sample after consolidation which can be obtained from the following equation:

$$h_c = h_0 - \Delta h_0 \quad (3.9)$$

Also  $h_0$  is the initial height of the sample and  $\Delta h_0$  is the change of height in the specimen at the end of the consolidation phase.

### 3.4. Cyclic Simple Shear Testing

#### 3.4.1. CSS Testing Program

A series of cyclic simple shear tests were conducted on each sand type with different Stress Amplitude Ratio (SRA) and Cyclic Period (CP) combinations in order to investigate the liquefaction susceptibility of each sand type under each condition. The purpose was to see the possible relationships between dilatant properties, granular shape factors and liquefaction resistances.

The specimens were consolidated under 50 kPa, 100 kPa or 150 kPa vertical stress and then sheared with cyclic simple shear loading until failure due to liquefaction.



### 3.4.2. Automated Cyclic Simple Shear Testing Apparatus

The device used for cyclic simple shear test in this study was Geocomp ShearTrac II which is capable of conducting direct shear, simple shear and cyclic simple shear tests on short, cylindrically shaped specimens.

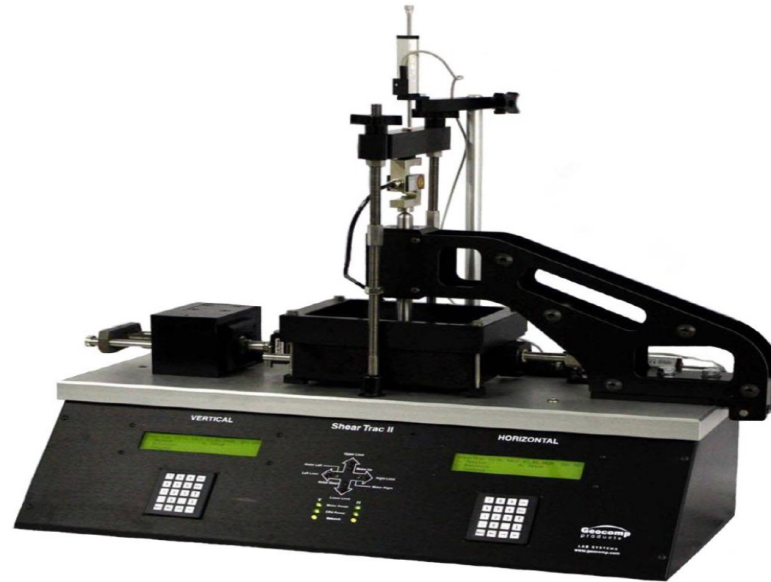


Figure 3.10. GeoComp Direct Simple Shear Apparatus.

The specimens are laterally confined by brass rings, as a result the changes in specimen height is equal to volume change. Under the simple shear test condition, normal stress ( $\sigma_v$ ) acts on top and shear stress ( $\tau$ ) acts on the bottom of the specimen while the top of the specimen is horizontally fixed and also radial strains are zero.

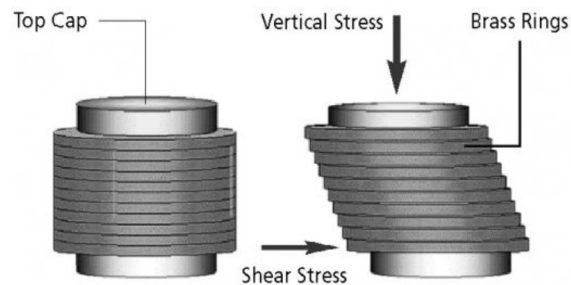


Figure 3.11. Vertical and Simple Shear Loads.

The CSS testing with this apparatus is fully automated and the apparatus is equipped with sensors for measuring and adjusting stress. During the cyclic simple shear loading phase, the apparatus maintains the specimen height constant by automatically adjusting the vertical stress applied. As a result of the zero radial strain condition forced by the brass rings, volume of sample remains unchanged throughout the CSS test. The difference between initial vertical stress and the real-time vertical stress is assumed as a hypothetical excess pore water pressure, which would be generated if the specimen was truly undrained. So when this difference becomes zero, it means that the hypothetical pore water pressure has become equal to vertical stress, the effective vertical stress has become zero and the sample has liquefied.

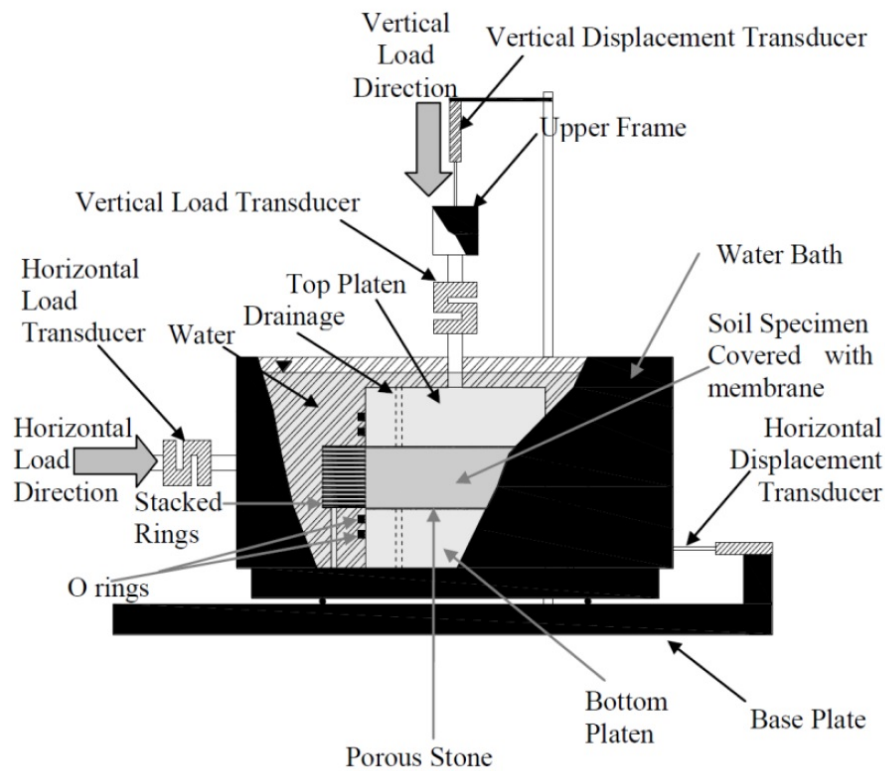


Figure 3.12. GeoComp Direct Simple Shear Apparatus.

### 3.4.3. Cyclic Simple Shear Testing Procedure

In this study the CSS test were conducted in two phases:

## (i) Consolidation Phase

All specimens were consolidated prior to shearing. Testing reconstituted dry samples, the ultimate consolidation stress was chosen as 50 kPa, 100 kPa and 150 Kpa for 15 minutes. Monitoring cyclic tests it was observed that this time is enough to decrease the vertical displacement ratio to zero.

## (ii) Cyclic Shearing

4 cyclic loading combinations were used for each sand type:

Table 3.5. CSS Tests SRA and CP Combinations.

Combination	SRA	CP
1	0.2	1
2	0.2	2
3	0.3	1
4	0.3	2

where CP is the cyclic period and SRA is the stress ratio amplitude, defined for the testing apparatus as:

$$SRA = \frac{\text{Applied Shear Stress}}{\text{Applied vertical Stress}} \quad (3.10)$$

The ideal sinusoidal waveform may not be achieved easily. According to Silver [76], the waveforms are acceptable provided that the difference between the amplitudes and durations of successive half-cycles is less than 10%, the noise (ringing) in the waveform is not significant, and there are not any prominent spikes near the peaks of waveform. The unacceptable waveforms can cause abnormal changes in pore water pressure resulting in significant deviations from the actual soil response to an ideal sinusoidal waveform.

The ShearTrac II apparatus uses a closed-loop load control system in order to provide a load-history consistent with that of an ideal sinusoidal waveform. It

uses a parameter called “Update A” for automatic updating of the load increments in a closed-loop loading system during a cyclic loading test due to nonlinear response of the material. Update A factor is dependent on several factors such as the stiffness and the dimensions of soil specimen, frequency of loading ( $f$ ), and calibration factors of the apparatus, and can be obtained using a calculation tool provided by the manufacturer. Other important parameter in the algorithm of closed-loop control, P-Gain, I-Gain and D-Gain were kept at default values as it was suggested in the apparatus instruction manual.

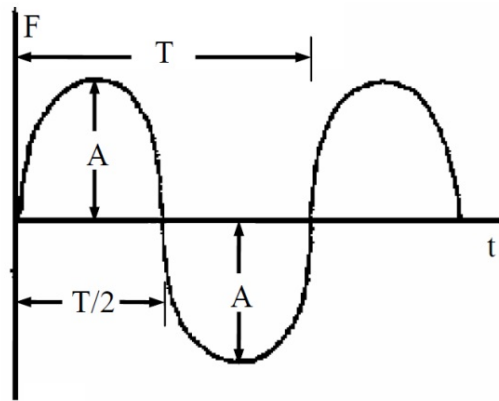


Figure 3.13. An ideal waveform [76].

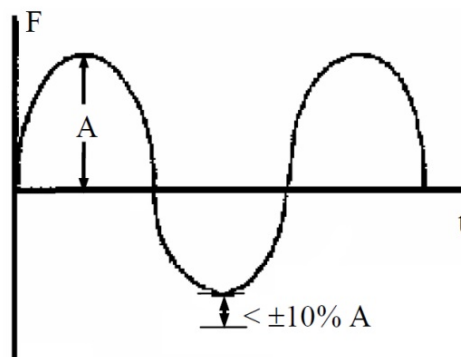


Figure 3.14. The limit for difference in amplitudes of successive half-cycles [76].

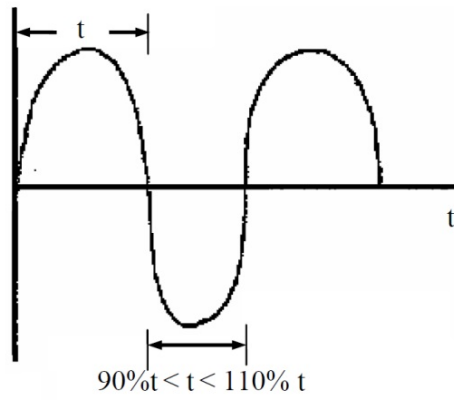


Figure 3.15. The limit for difference in duration of successive half-cycles [76].

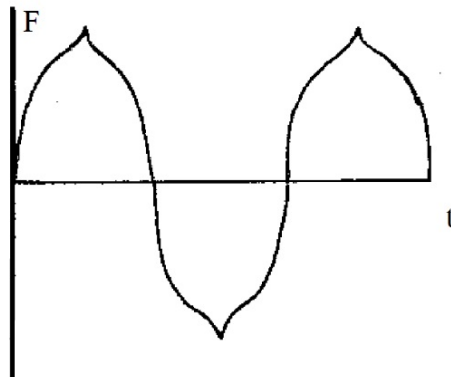


Figure 3.16. Unacceptable waveform due to spikes at peaks [76].

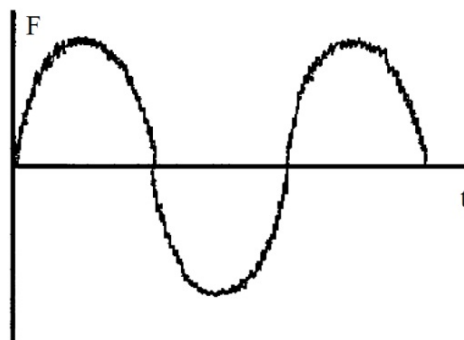


Figure 3.17. Unacceptable ringing on waveform [76].

#### 3.4.4. Sample Preparation

Like the triaxial specimens, air pluviation method was used for cyclic simple shear test specimens. Since diversity in sample relative densities was enough and there was no exact target relative density, first the specimens were prepared and then the relative density was obtained using sample volume, weight and specific gravity of the sand. Mild vibration was also used in CSS tests to prepare denser specimens.

#### 3.4.5. Testing Materials

3 types of sands were tested in this study, Akpınar sand, Kilyos sand and Sile sand, with characteristics as follows. Specific gravity values were determined according to ASTM D854 – 10 standard test.

Table 3.6. Sand Properties.

Sand Type	Specific Gravity	Maximum Void Ratio	Minimum Void Ratio
Sile	2.61	0.78	0.52
Akpınar	2.63	0.87	0.58
kilyos	2.66	0.77	0.44

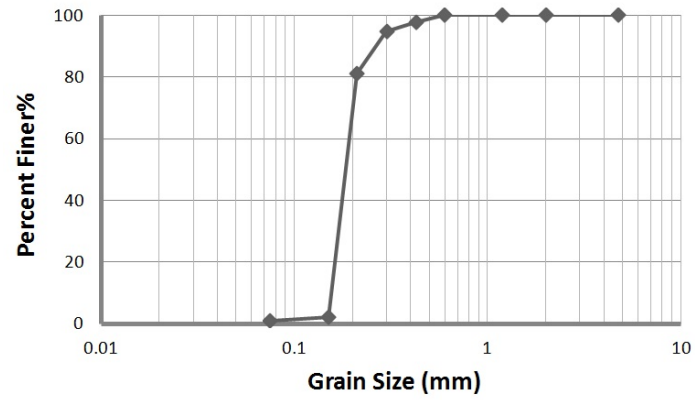


Figure 3.18. Akpinar Grain Size Distribution.

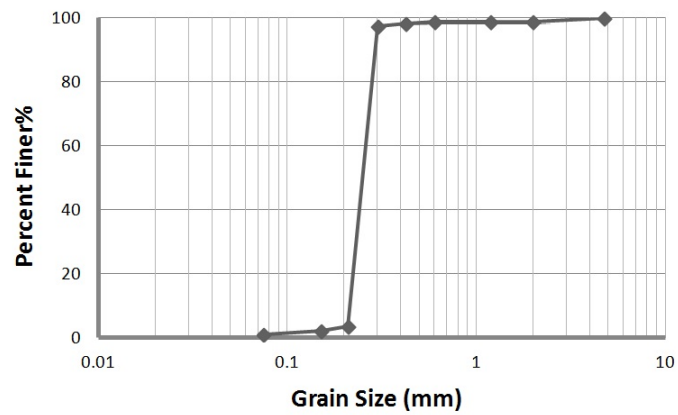


Figure 3.19. Kilyos Grain Size Distribution.

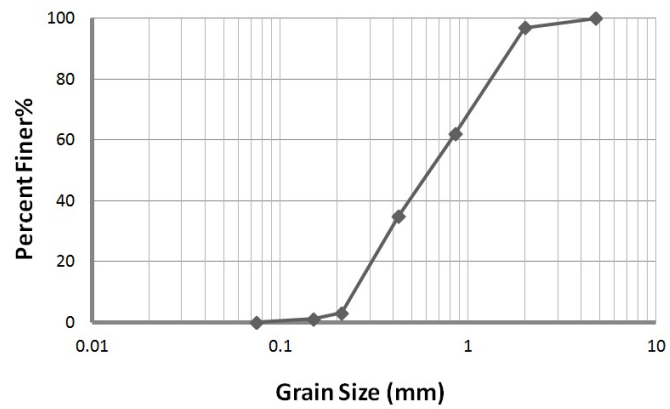


Figure 3.20. Sile Grain Size Distribution.

## 4. EXPERIMENTS AND TEST RESULTS

In this chapter shape factors, triaxial test results and cyclic simple shear test results will be investigated:

- (i) Average Circularity and Roundness of the sand particles will be evaluated.
- (ii) Consolidated Drained Triaxial test results will be used in order to find the  $\alpha_\psi$  and  $m_\psi$  values of Equation 2.27.
- (iii) Cyclic Simple Shear tests results will be considered to investigate the liquefaction susceptibility of each sand type.

### 4.1. Shape Factor Analysis Results

The parameters used in this study are circularity and roundness which are calculated as Equations 2.1 and 2.2.

The more proximate the roundness values get to 1, the less angularity is expected, meaning that the particles have more rounded corners. Besides as the circularity approaches 1, the shape of the particle becomes more circular.

As can be seen in Table 4.1 , both circularity and roundness are the highest in Kilyos

Table 4.1. Average Circularity and Roundness Values for All Sand Types.

<b>Sand Type</b>	<b>Circularity</b>	<b>Roundness</b>
<b>Sile</b>	0.674	0.725
<b>Akpınar</b>	0.716	0.728
<b>Kilyos</b>	0.743	0.759

sand and the lowest in Sile sand. The effect of this difference will be investigated in upcoming chapters.



Table 4.2. Circularity and Roundness Values of Individual Sile Sand Particles.

Particle	Circularity	Roundness
1	0.73	0.77
2	0.65	0.66
3	0.56	0.55
4	0.7	0.88
5	0.71	0.68
6	0.69	0.78
7	0.66	0.62
8	0.79	0.77
9	0.64	0.87
10	0.73	0.91
11	0.62	0.6
12	0.56	0.51
13	0.67	0.67
14	0.7	0.76
15	0.73	0.63
16	0.76	0.75
17	0.75	0.8
18	0.62	0.51
19	0.69	0.63
20	0.38	0.73
21	0.63	0.57
22	0.62	0.63
23	0.66	0.51
24	0.6	0.63
25	0.67	0.64
26	0.74	0.77

Table 4.2. Circularity and Roundness Values of Individual Sil Sand Particles (cont).

Particle	Circularity	Roundness
27	0.63	0.68
28	0.6	0.62
29	0.6	0.56
30	0.71	0.64
31	0.66	0.63
32	0.64	0.83
33	0.63	0.91
34	0.74	0.83
35	0.68	0.83
36	0.69	0.6
37	0.65	0.81
38	0.76	0.78
39	0.72	0.79
40	0.74	0.86
41	0.73	0.88
42	0.7	0.87
43	0.62	0.56
44	0.72	0.85
45	0.67	0.98
46	0.72	0.75
47	0.73	0.94
48	0.67	0.83
49	0.63	0.58
50	0.81	0.8

Table 4.3. Circularity and Roundness Values of Individual Akpınar Sand Particles.

Particle	Circularity	Roundness
1	0.75	0.77
2	0.62	0.47
3	0.63	0.59
4	0.73	0.71
5	0.74	0.8
6	0.7	0.55
7	0.64	0.59
8	0.73	0.79
9	0.72	0.92
10	0.77	0.68
11	0.74	0.77
12	0.75	0.87
13	0.77	0.73
14	0.77	0.73
15	0.72	0.69
16	0.73	0.97
17	0.68	0.71
18	0.71	0.68
19	0.76	0.81
20	0.71	0.69
21	0.76	0.84
22	0.72	0.58
23	0.71	0.66
24	0.71	0.73
25	0.67	0.8
26	0.71	0.79

Table 4.3. Circularity and Roundness Values of Individual Akpinar Sand Particles (cont).

<b>Particle</b>	<b>Circularity</b>	<b>Roundness</b>
27	0.72	0.63
28	0.65	0.7
29	0.7	0.66
30	0.77	0.95
31	0.71	0.64
32	0.67	0.72
33	0.8	0.93
34	0.71	0.59
35	0.67	0.59
36	0.74	0.72
37	0.77	0.83
38	0.78	0.91
39	0.73	0.65
40	0.71	0.85
41	0.73	0.59
42	0.62	0.68
43	0.73	0.67
44	0.72	0.67
45	0.7	0.75
46	0.72	0.68
47	0.74	0.77
48	0.78	0.83
49	0.68	0.68
50	0.65	0.83

Table 4.4. Circularity and Roundness Values of Individual Kilyos Sand Particles.

Particle	Circularity	Roundness
1	0.78	0.68
2	0.79	0.76
3	0.81	0.76
4	0.79	0.76
5	0.76	0.67
6	0.67	0.62
7	0.82	0.91
8	0.76	0.91
9	0.68	0.76
10	0.62	0.41
11	0.68	0.58
12	0.65	0.65
13	0.83	0.76
14	0.73	0.71
15	0.73	0.71
16	0.78	0.91
17	0.72	0.56
18	0.75	0.74
19	0.75	0.76
20	0.73	0.8
21	0.82	0.72
22	0.75	0.69
23	0.67	0.64
24	0.73	0.73
25	0.76	0.94
26	0.77	0.93

Table 4.4. Circularity and Roundness Values of Individual Kilyos Sand Particles (cont).

Particle	Circularity	Roundness
27	0.75	0.87
28	0.73	0.93
29	0.79	0.79
30	0.76	0.68
31	0.75	0.83
32	0.77	0.76
33	0.8	0.93
34	0.78	0.78
35	0.72	0.67
36	0.75	0.75
37	0.77	0.88
38	0.65	0.52
39	0.78	0.79
40	0.7	0.55
41	0.65	0.68
42	0.78	0.85
43	0.78	0.87
44	0.81	0.94
45	0.76	0.73
46	0.77	0.84
47	0.59	0.91
48	0.74	0.91
49	0.75	0.79
50	0.74	0.71

## 4.2. Triaxial Testing

As explained previously, Cinicioglu and Abadkon [30] formula is used for calculating the dilation angle of samples with different pre-shear relative densities and confinement pressures. The soil specific constants,  $\alpha_\psi$  and  $m_\psi$  should be determined first in order to use this formula. For that purpose, CD triaxial test results are needed. Theoretically, two points are enough to derive the  $\tan \psi_p - \frac{p'_i}{p_a}$  linear relationship, since the influences of density and pressure on  $\alpha_\psi$  are uncoupled. However in this study, more tests were conducted to increase accuracy, thus the average values determined were used.

$$\tan \psi_p = \alpha_\psi \left( \frac{p'_i}{p_a} \right) + m_\psi I_D$$

Peak dilation angle value ( $\psi_p$ ) for each triaxial test was calculated from the triaxial test data using Schanz and Vermeer [29] equation:

$$\sin \psi = -\frac{\frac{\dot{\epsilon}_v}{\dot{\epsilon}_1}}{2 - \frac{\dot{\epsilon}_v}{\dot{\epsilon}_1}}$$

This equation allows the calculation of the dilation angle at any instance during the shearing phase. Peak dilation angle is the peak value of the moving average trend line on the dilation angle- axial strain graph (Figure 4.1).

Care must be taken while deciding on the peak dilation angle value since pinpointing the accurate peak point on the average trend line can be difficult.

The  $\alpha_\psi$  and  $m_\psi$  constant values for Akpınar sand were previously determined by Altunbas [75] with the exact same method and apparatus.

The final resultant values for Akpınar sand were:

$$\alpha_\psi = -0.0662$$

$$m_\psi = 0.64$$

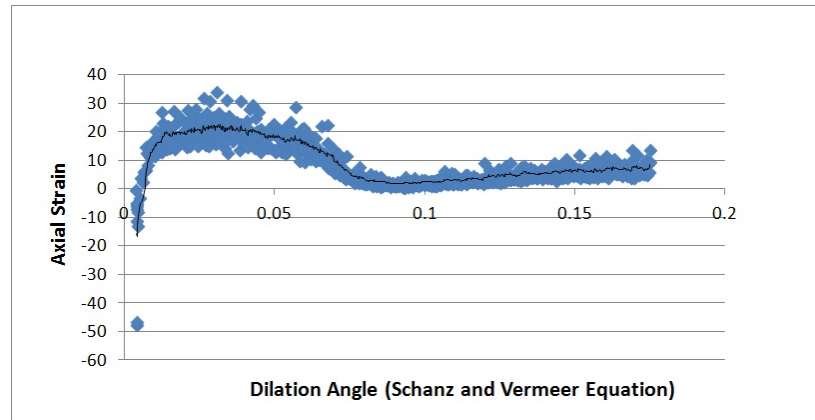


Figure 4.1. Example Dilation Angle-Axial Strain Diagram.

#### 4.2.1. Silé Sand Triaxial Test Results

CD triaxial tests were conducted on 7 Silé sand samples with differing combinations of pre-shear confinement pressure ( $p'_i$ ) and relative density ( $I_D$ ) (Table 4.5). The

Table 4.5. Silé Sand Triaxial Testing.

Test No	$\sigma'_1$ (kPa)	$p'_i$ (kPa)	$I_D$	$K_0$
1	100	63.1	0.61	0.446
2	100	69.7	0.54	0.545
3	100	66.1	0.5	0.492
4	200	107.4	0.5	0.305
5	250	153.1	0.96	0.419
6	150	90.5	0.58	0.405
7	250	118.1	0.73	0.270

final resultant values for Silé sand were:

$$\alpha_{\psi} = -0.3191$$

$$m_{\psi} = 0.723$$



The validity of the calculated average  $\alpha_\psi$  and  $m_\psi$  values were tested knowing that the tangent of dilation angles calculated directly from triaxial test results should be equal to the tangent of dilation angle calculated from Cinicioglu and Abadkon [30] formula.

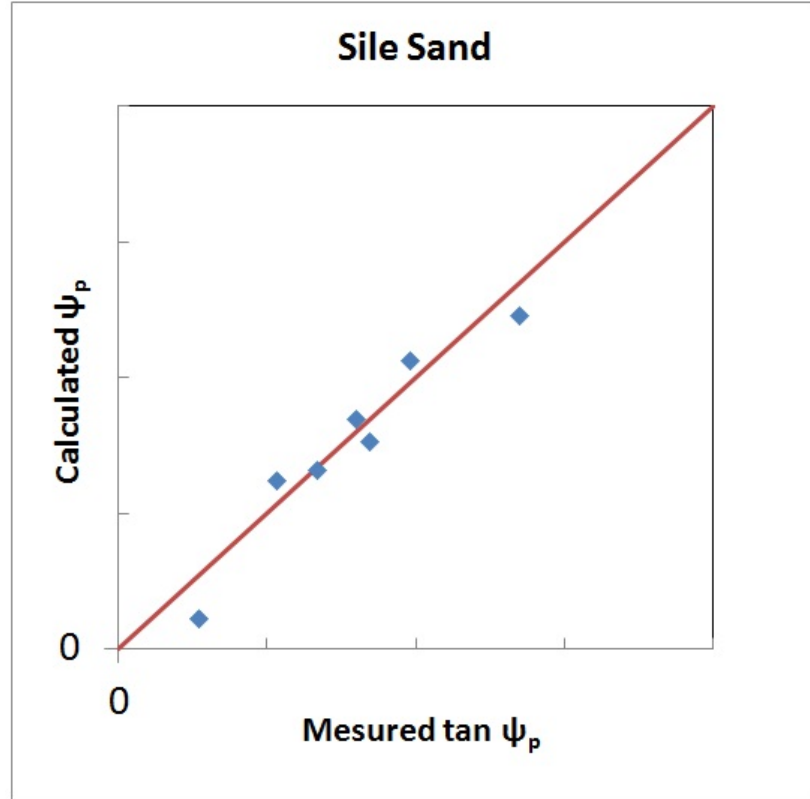


Figure 4.2. Sile sand  $\tan \psi_p$  calculated with Schanz and Vermeer [29] relationship -  $\tan \psi_p$  calculated with Cinicioglu and Abadkon [30] relationship.

As shown in Figure 4.2, the points slide slightly from the  $x = y$  line. The divergence may be because of minor errors in testing procedure, especially errors in measuring the relative densities since dry sand samples are so sensitive to any motion or even a seldom impact.

It is known that there is a linear relationship between peak friction angle and peak dilation angle values of each sand type.

Peak friction angle is calculated using triaxial test outcome according to Coulomb's

model:

$$\sin \phi_p = \frac{(\sigma'_1)_p - (\sigma'_3)_p}{(\sigma'_1)_p + (\sigma'_3)_p} \quad (4.1)$$

where  $(\sigma'_1)_p$  and  $(\sigma'_3)_p$  are stress values at the peak strength point of the specimen.

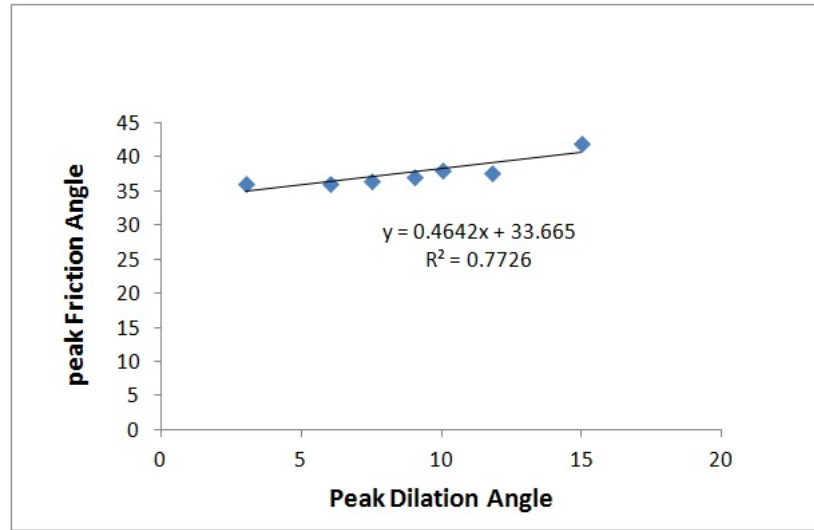


Figure 4.3. Linear relationship between peak friction angle and peak dilation angle of Sil sand.

The zero intercept of this line (Figure 4.3) corresponds to critical state friction angle where the dilation angle is zero. Critical state friction angle is 33.7 degrees for Sil sand.

Loose sand samples may have zero dilation angle which means their peak friction angle is equal to their critical state friction angle.

#### 4.2.2. Kilyos Sand Triaxial Test Results

CD triaxial tests were conducted on 7 Kilyos sand samples with differing combinations of pre-shear confinement pressure ( $p'_i$ ) and relative density ( $I_D$ ) (Table 4.6).

Table 4.6. Kilyos Sand Triaxial Testing.

Test No	$\sigma'_1$ (kPa)	$p'_i$ (kPa)	$I_D$	$K_0$
1	150	94.3	0.66	0.441
2	250	185	0.39	0.610
3	300	160.3	0.45	0.299
4	200	128.5	0.51	0.467
5	225	120.6	0.39	0.294
6	250	133.4	0.48	0.298
7	200	135.7	0.69	0.518

The final resultant values for Sils sand were:

$$\alpha_{\psi} = -0.00172$$

$$m_{\psi} = 0.5896$$

As shown in Figure 4.4, the points slide slightly from the  $x=y$  line. The results are acceptable since the divergence is not so severe.

Deriving the linear relationship between peak friction angle and peak dilation angle values for Kilyos sand, it can be seen that the critical state friction angle for this sand type is 31.2 degrees (Figure 4.5).

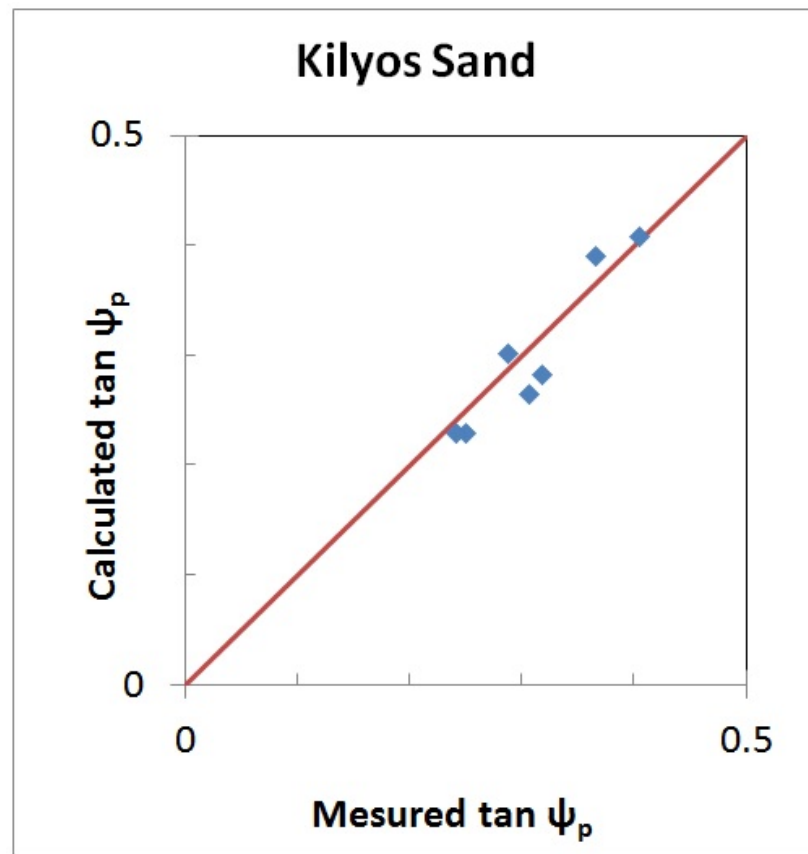


Figure 4.4. Kilyos sand  $\tan \psi_p$  calculated with Schanz and Vermeer [29] relationship -  $\tan \psi_p$  calculated with Cinicioglu and Abadkon [30] relationship.

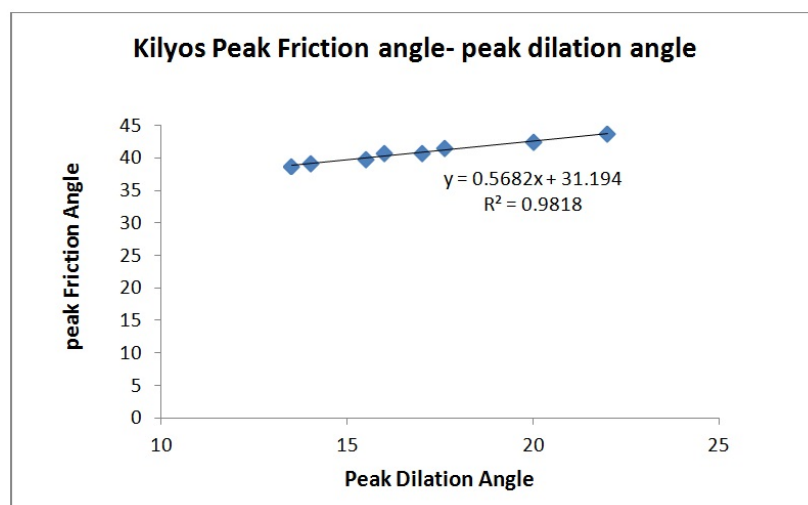


Figure 4.5. Linear relationship between peak friction angle and peak dilation angle of Kilyos sand.

### 4.3. Cyclic Simple Shear Test

Cyclic simple shear tests were conducted on sand samples with differing relative densities under each of the 4 Stress Ratio Amplitude (SRA) and Cyclic Period (CP) combinations below.

Table 4.7. SRA and CP Combinations.

Combination	SRA	CP (sec)
1	0.3	1
2	0.3	2
3	0.2	1
4	0.2	2

Each of Akpınar and Sile sand samples were consolidated under 50 kPa and 100 kPa vertical stresses. Kilyos sand samples were also tested with 150 kPa consolidation pressure, other than 50 kPa and 100 kPa, in order to investigate the effect of consolidation pressure more clearly.

Samples were assumed liquefied when the generated hypothetical excess pore water pressure became equal to initial vertical stress. The number of loading cycles at which the samples liquefy (NCL) were obtained using graphs provided by the software. As shown in Figure 4.6, the CSS test software provides shear strain, shear stress and excess pressure graphs depending on the number of loading cycles.

The dilation angles of the CSS samples were calculated using the empirical equation proposed by Cinicioglu and Abadkon [30] (Equation 2.27). Dilatancy constants  $\alpha_\psi$  and  $m_\psi$  used in the dilatancy equation were calculated using triaxial tests.

Relative density ( $I_D$ ) of each CSS sample was calculated as follows:

$$I_D = \frac{e_{max} - e}{e_{max} + e_{min}} \quad (4.2)$$

where  $e_{min}$  and  $e_{max}$  are maximum and minimum void ratios of the sand, determined according to ASTM D-4253 and ASTM D-4254 standards, and  $e$  is void ratio of sample

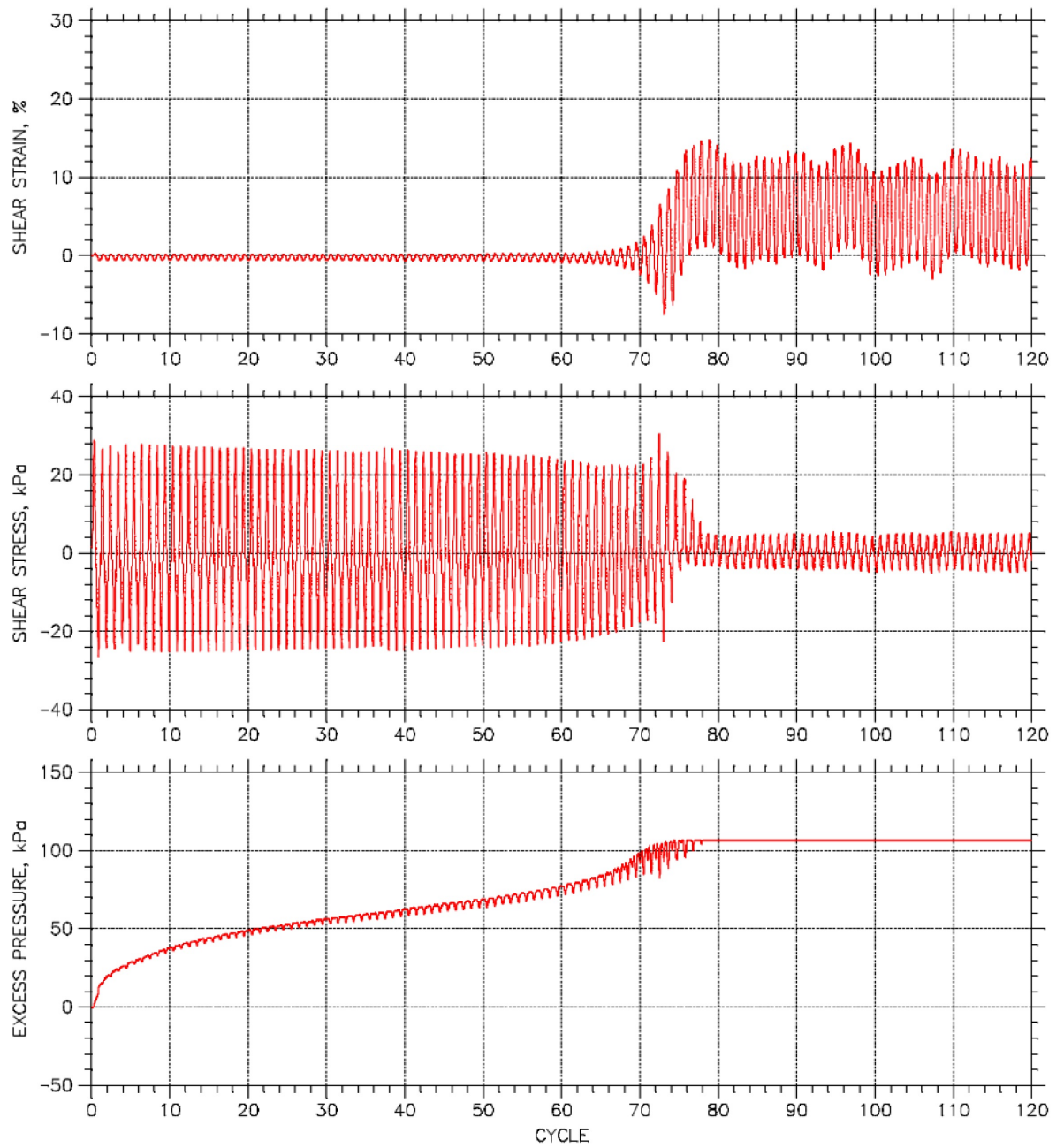


Figure 4.6. Example CSS Test Result.

which is determined using the equation below:

$$e = \frac{G_s \gamma_w}{\gamma_s} - 1 \quad (4.3)$$

where  $\gamma_w$  is the unit weight of water,  $G_s$  is the sand specific gravity and  $\gamma_s$  is the dry unit weight of sample calculated as:

$$\gamma_s = \frac{W_s}{V} \quad (4.4)$$

where  $W_s$  is the dry weight and  $V$  is the volume of the specimen.

In order to calculate  $p'_i$ ,  $K_0$  value is needed since cyclic simple shear samples are consolidated under  $K_0$  conditions. For that purpose, the relationship between  $K_0$  and relative density values were derived from previous retaining wall model tests conducted on Akpınar [75] sand and triaxial test results conducted on Sile and Kilyos sands.

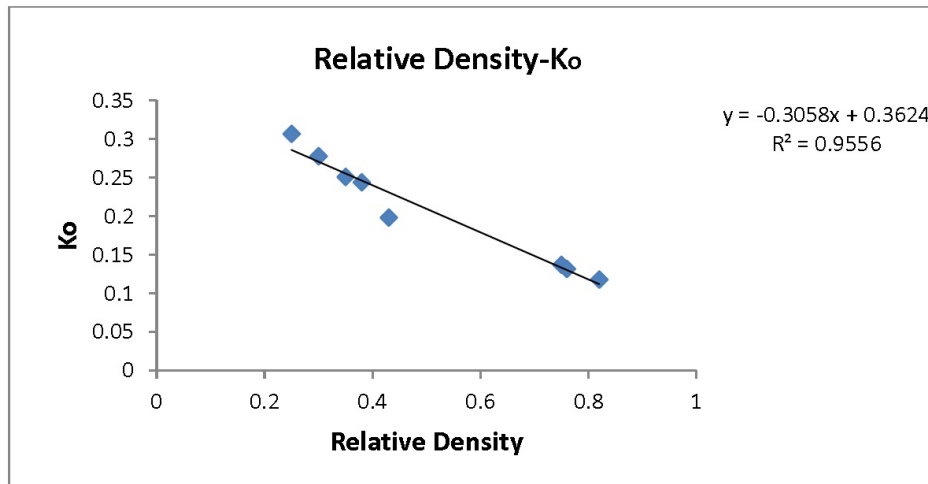


Figure 4.7. Relative Density-  $K_0$  Relationship for Akpınar Sand.

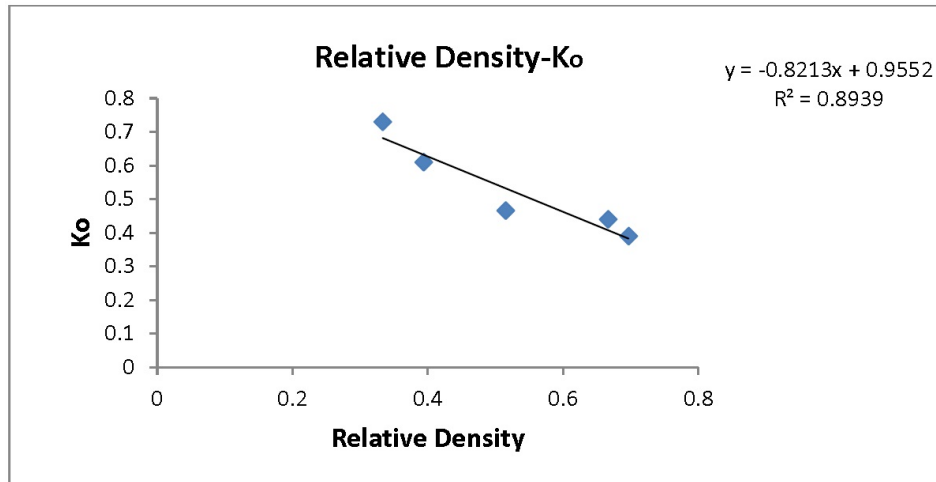


Figure 4.8. Relative Density-  $K_0$  Relationship for Kilyos Sand.

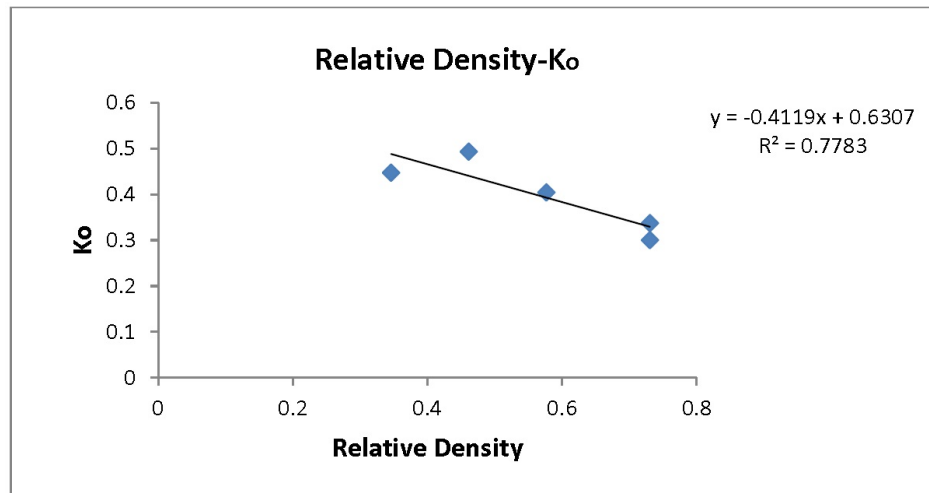


Figure 4.9. Relative Density-  $K_0$  Relationship for Sile Sand.

Table 4.8. Equations Used to Calculate  $K_0$  for CSS samples.

Sand Type	$I_D$ - $K_0$ Relationship
Akpınar	$K_0 = -0.3058I_D + 0.3624$
Kilyos	$K_0 = -0.8213I_D + 0.9552$
Sile	$K_0 = -0.4119I_D + 0.6307$



#### 4.3.1. Akpınar Sand CSS Test Results

Dry sand samples were prepared using air pluviation method. The radial strain is zero in CSS samples since they are confined with teflon rings. Additionally the weight of the samples were kept constant, so the relative density depends only on sample height. Variations in relative density would change  $K_0$  value, and accordingly affects the confinement pressure. As a result of the changes in relative density and confinement pressure, dilation angle value would change from sample to sample. It is known that

Table 4.9. Akpınar CSS Test Results for 50 Kpa Consolidation Pressure.

Sample No	$I_D$	$\psi_p$	$SRA$	$CP(sec)$	$NCL$
1	0.45	15.4	0.2	1	176
2	0.22	7.2	0.2	1	49
3	0.33	11.1	0.2	1	126
4	0.43	14.5	0.2	1	180
5	0.25	8.4	0.2	1	69
6	0.32	10.5	0.2	1	95
7	0.38	12.8	0.2	1	141
8	0.29	9.6	0.2	2	62
9	0.18	5.7	0.2	2	32
10	0.37	12.5	0.2	2	69
11	0.46	15.8	0.2	2	100
12	0.49	16.6	0.2	2	103
13	0.43	14.5	0.2	2	96
14	0.17	5.1	0.2	2	23
15	0.24	7.7	0.2	2	34
16	0.16	5.0	0.3	1	11
17	0.38	12.9	0.3	1	20
18	0.31	10.5	0.3	1	17

Table 4.9. Akpinar CSS Test Results for 50 Kpa Consolidation Pressure (cont).

Sample No	$I_D$	$\psi_p$	$SRA$	$CP(sec)$	$NCL$
19	0.50	17.1	0.3	1	35
20	0.29	9.6	0.3	1	15
21	0.21	6.9	0.3	1	11
22	0.23	7.3	0.3	2	7
23	0.30	10.1	0.3	2	8
24	0.43	14.6	0.3	2	9
25	0.68	22.9	0.3	2	21
26	0.49	16.7	0.3	2	12
27	0.64	21.7	0.3	2	19
28	0.62	20.8	0.3	2	18

liquefaction is dependent on both relative density and confinement pressure values of the sample [46]. Cinicioglu and Abadkon [30] equation relates these two parameters to dilation angle value. So dilation angle is a better indicator when studying liquefaction susceptibility, since it takes both parameters into account.

As shown in the Figure 4.10, liquefaction susceptibility decreases following linear relationship, as the dilation angle increases. This increase in liquefaction resistance is expectedly the general behavior regardless of the loading condition (stress ratio amplitude, cyclic shear stress, cyclic period, etc).

For the two loading conditions with the same SRA and differing CPs, (Figure 4.10, a and b, c and d) the increase in liquefaction resistance with increase in dilation angle is much higher (almost 2.3 times) for the smaller cyclic period (1 sec). It means that under loading condition with lower cyclic periods, the liquefaction resistance is much more dependent of the value of dilation angle. Also, for the two loading condition with the same cyclic period and differing SRAs (Figure 4.10, a and c, b and d), the increase in liquefaction resistance with increase in dilation angle is again higher (almost 2.2 times) for the smaller SRA (0.2).

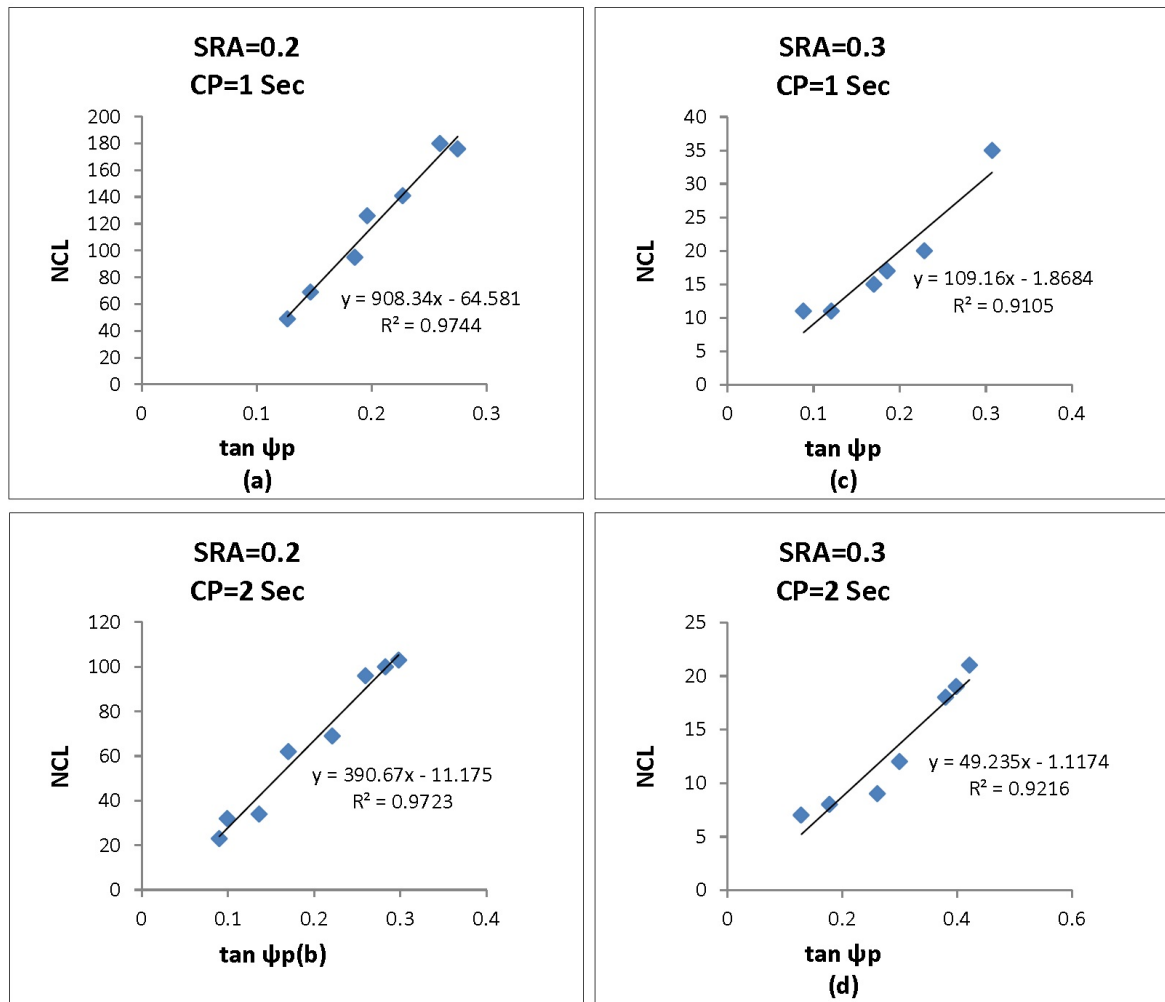


Figure 4.10. Akpinar  $\tan \psi_p$ - NCL (Consolidation pressure= 50 kpa).

For Akpinar sand samples consolidated under 100 kPa, for the two loading conditions with the same SRA and differing CPs, (Figure 4.11, a and b, c and d) the increase in liquefaction resistance with increase in dilation angle is again higher for the smaller CP (1 sec). Also, for the two loading conditions with the same CP and differing SRAs (Figure 4.11, a and c, b and d), the increase in liquefaction resistance with increase in dilation angle is higher for the smaller SRA (0.2). Even though comparing a and b with c and d, as well a and c with b and d, does not result in a similar ratio in samples with 100 kPa vertical stress.

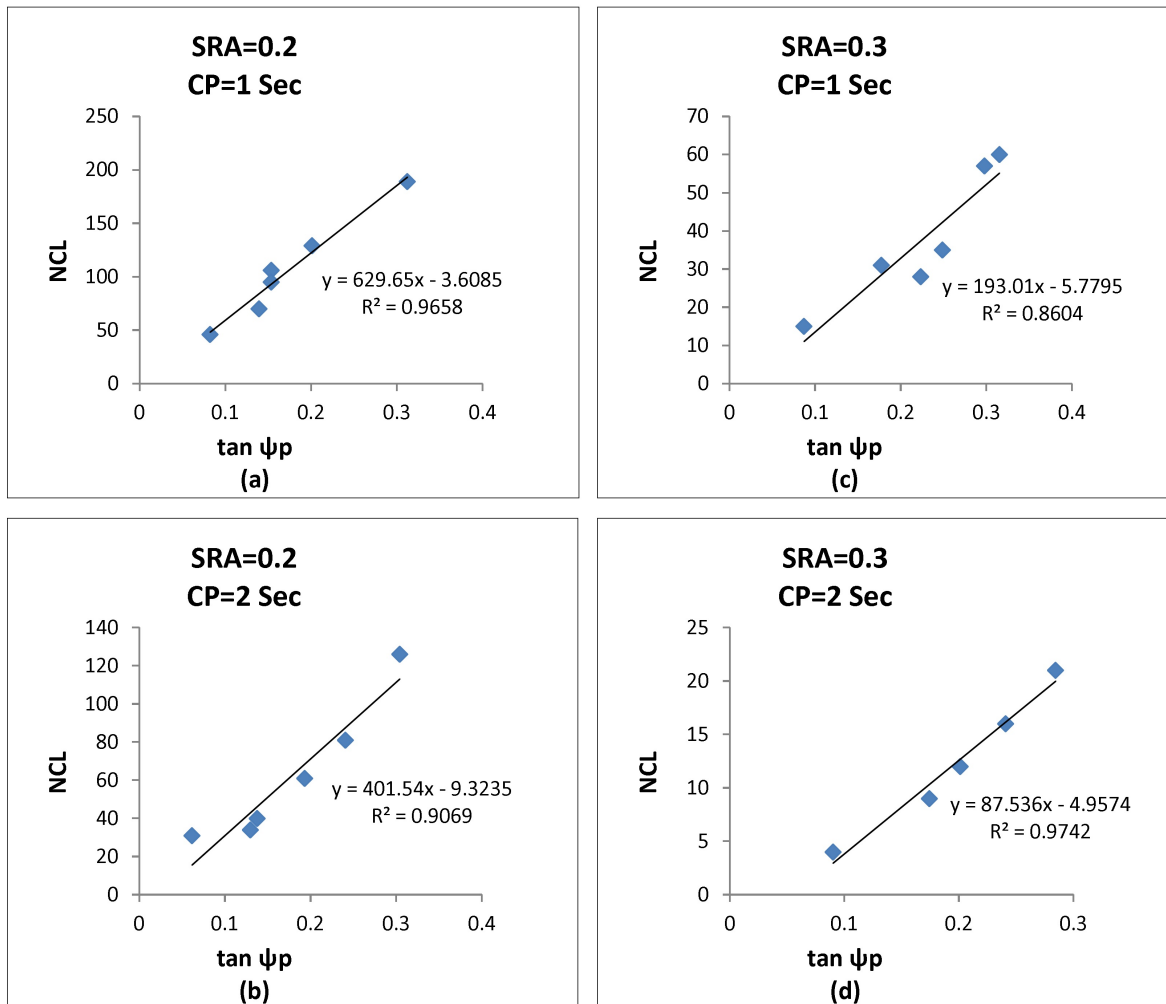


Figure 4.11. Akpinar  $\tan \psi_p$ - NCL (Consolidation pressure= 100 kPa).

Table 4.10. Akpınar CSS Test Results for 100 Kpa Consolidation Pressure.

<b>Sample No</b>	$I_D$	$\psi_p$	$SRA$	$CP(sec)$	$NCL$
1	0.18	4.7	0.2	1	46
2	0.29	8.7	0.2	1	106
3	0.53	17.3	0.2	1	189
4	0.27	7.9	0.2	1	70
5	0.29	8.7	0.2	1	95
6	0.36	11.4	0.2	1	129
7	0.25	7.4	0.2	2	34
8	0.35	10.9	0.2	2	61
9	0.52	16.9	0.2	2	126
10	0.15	3.5	0.2	2	31
11	0.42	13.5	0.2	2	81
12	0.27	7.8	0.2	2	40
13	0.33	10.1	0.3	1	31
14	0.19	4.9	0.3	1	15
15	0.40	12.6	0.3	1	28
16	0.54	17.5	0.3	1	60
17	0.44	13.9	0.3	1	35
18	0.51	16.6	0.3	1	57
19	0.32	9.9	0.3	2	9
20	0.19	5.1	0.3	2	4
21	0.36	11.4	0.3	2	12
22	0.49	15.9	0.3	2	21
23	0.42	13.5	0.3	2	16

#### 4.3.2. Sil Sand CSS Test Results

CSS tests were conducted on dry Sil sand samples with the same SRA (0.2 and 0.3) and CP (1 and 2 sec) combinations, under both 50 kPa and 100 kPa vertical pressure. The test results are as follows:

Table 4.11. Sil CSS Test Results for 50 Kpa Consolidation Pressure.

Sample No	$I_D$	$\psi_p$	SRA	CP(sec)	NCL
1	0.30	7.5	0.2	1	56
2	0.52	16.9	0.2	1	268
3	0.50	16.05	0.2	1	219
4	0.46	14.1	0.2	1	177
5	0.35	9.8	0.2	1	121
6	0.54	17.8	0.2	1	288
7	0.31	8.0	0.2	2	25
8	0.34	9.4	0.2	2	32
9	0.29	7.1	0.2	2	17
10	0.42	12.7	0.2	2	84
11	0.35	9.8	0.2	2	46
12	0.49	15.7	0.2	2	120
13	0.36	10.3	0.2	2	53
14	0.21	3.8	0.3	1	10
15	0.30	7.6	0.3	1	11
16	0.33	8.9	0.3	1	15
17	0.47	15.0	0.3	1	27
18	0.44	13.4	0.3	1	25
19	0.45	14.0	0.3	1	20
20	0.71	24.1	0.3	1	37

Table 4.11. Sile CSS Test Results for 50 Kpa Consolidation Pressure (cont).

Sample No	$I_D$	$\psi_p$	SRA	CP (sec)	NCL
21	0.39	11.7	0.3	2	9
22	0.29	7.4	0.3	2	7
23	0.52	16.8	0.3	2	13
24	0.37	10.5	0.3	2	9
25	0.69	23.1	0.3	2	18
26	0.47	14.9	0.3	2	11

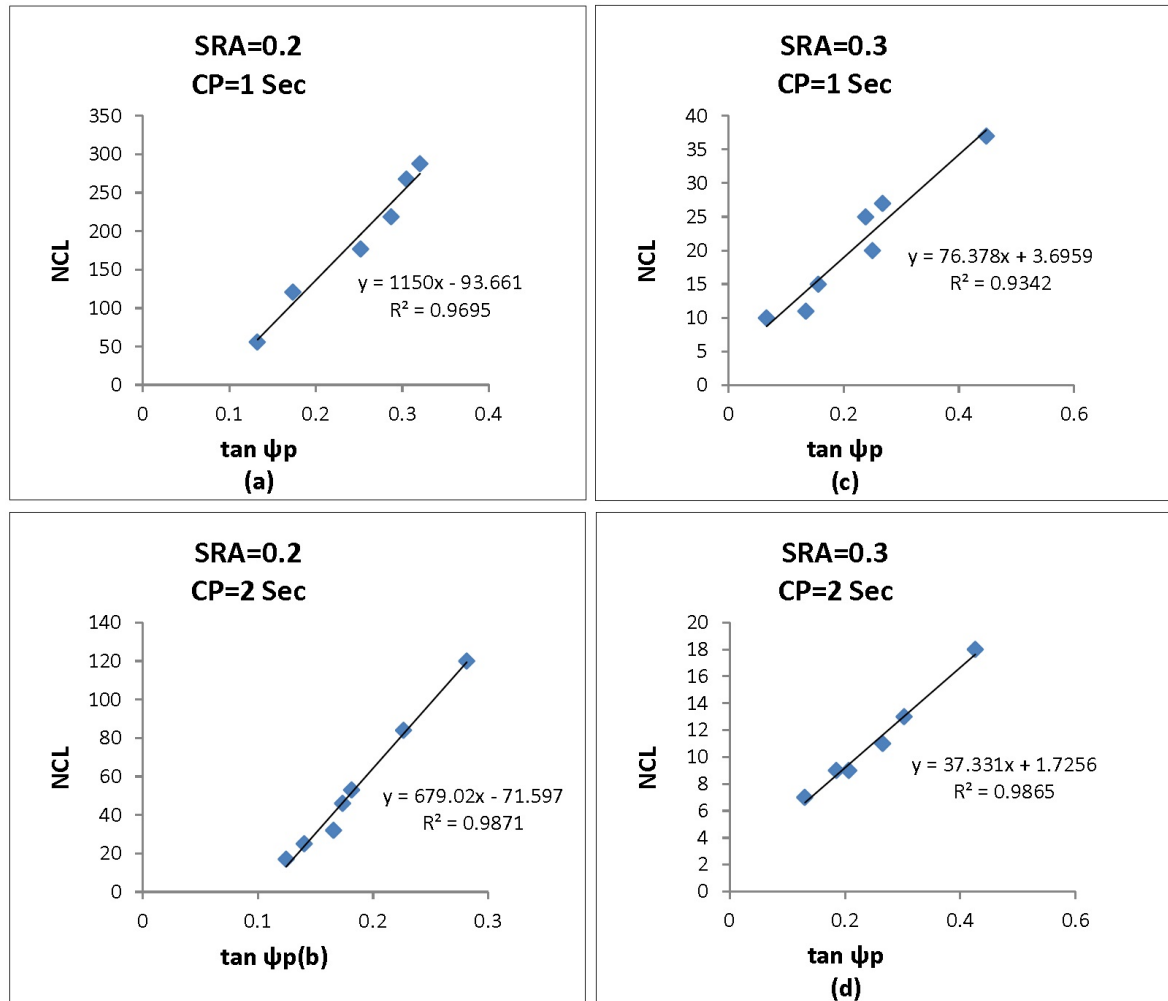
Figure 4.12. Sile  $\tan \psi_p$ - NCL (Consolidation pressure= 50 kpa).

Table 4.12. Silo CSS Test Results for 100 Kpa Consolidation Pressure.

Sample No	$I_D$	$\psi_p$	$SRA$	$CP(sec)$	$NCL$
1	0.36	3.5	0.2	1	117
2	0.46	7.9	0.2	1	191
3	0.31	1.1	0.2	1	90
4	0.34	2.5	0.2	1	105
5	0.3	0.5	0.2	1	94
6	0.39	4.7	0.2	1	182
7	0.31	1.2	0.2	2	44
8	0.47	8.2	0.2	2	81
9	0.34	2.5	0.2	2	62
10	0.32	1.5	0.2	2	46
11	0.54	11.4	0.2	2	117
12	0.39	4.9	0.2	2	75
13	0.34	2.3	0.3	1	17
14	0.51	10.0	0.3	1	42
15	0.34	2.5	0.3	1	20
16	0.44	7.1	0.3	1	29
17	0.30	0.6	0.3	1	22
18	0.58	13.3	0.3	1	53
19	0.31	0.9	0.3	2	11
20	0.38	4.2	0.3	2	13
21	0.52	10.8	0.3	2	24
22	0.35	2.9	0.3	2	11
23	0.39	4.7	0.3	2	15
24	0.54	11.5	0.3	2	31



For Sile samples consolidated under either 50 kPa (Figure 4.12) or 100 kPa (Figure 4.13), for the two loading conditions with the same SRA and differing CPs, the increase in liquefaction resistance with increase in dilation angle is higher for the smaller CP (1 sec). Also, for the two loading condition with the same CP and differing SRA, the increase in liquefaction resistance with increase in dilation angle is higher for the smaller SRA (0.2).

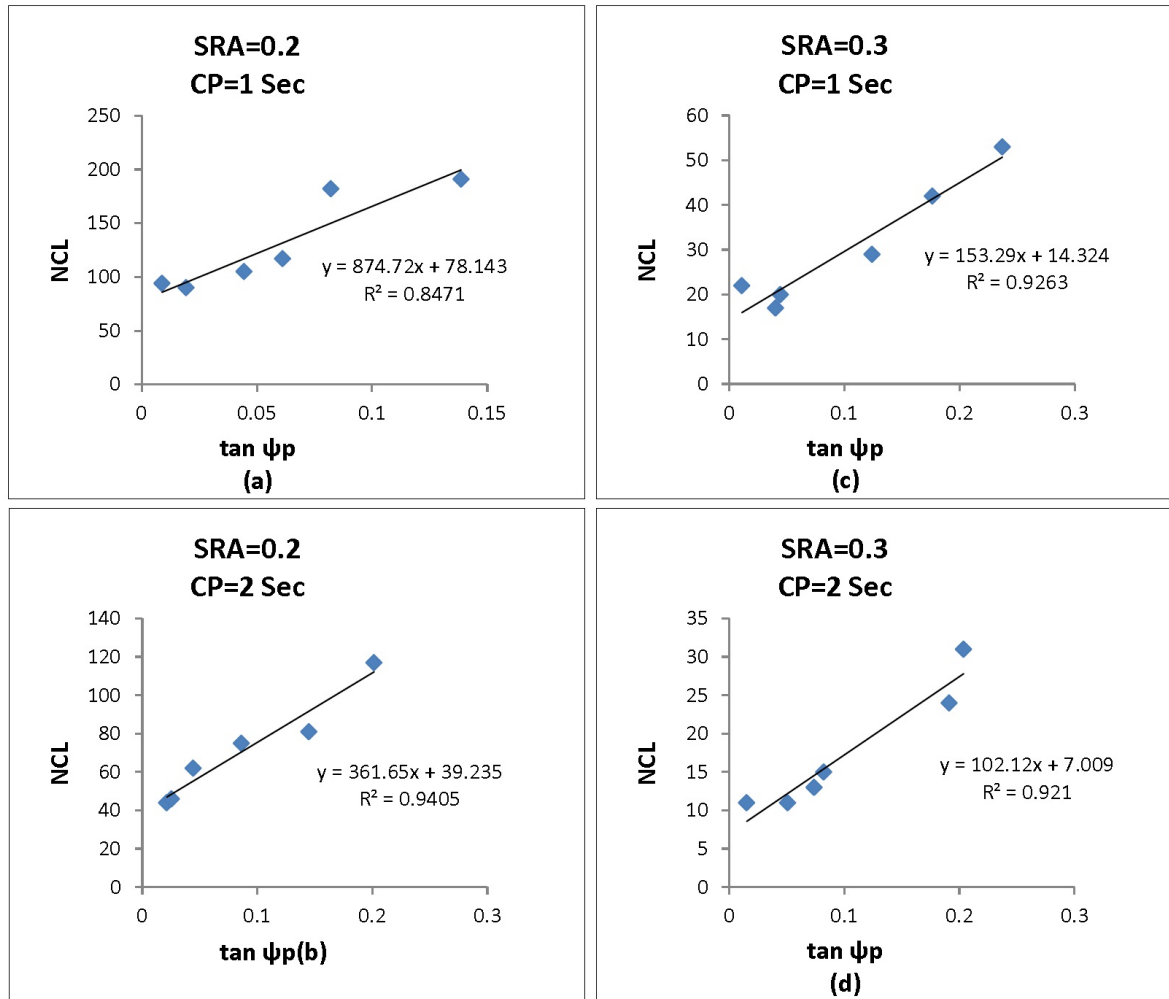


Figure 4.13. Sile  $\tan \psi_p$ -  $NCL$  (Consolidation pressure= 100 kPa).

#### 4.3.3. Kilyos Sand CSS Test Results

CSS tests were conducted on dry Kilyos sand samples too, with the same SRA (0.2 and 0.3) and CP (1 and 2 sec) combinations, under both 50 kPa and 100 kPa ver-

tical pressure. In order to observe the effect of applied consolidation pressure, Kilyos sand was also tested under 150 kPa vertical stress, with the same SRA (0.2 and 0.3) and CP (1 and 2 sec) combinations.

Table 4.13. Kilyos CSS Test Results for 50 Kpa Consolidation Pressure.

Sample No	$I_D$	$\psi_p$	SRA	CP (sec)	NCL
1	0.30	9.9	0.2	1	69
2	0.36	12.1	0.2	1	367
3	0.40	12.2	0.2	1	285
4	0.49	16.1	0.2	1	991
5	0.45	14.7	0.2	1	709
6	0.41	13.5	0.2	1	585
7	0.33	10.9	0.2	2	126
8	0.41	13.5	0.2	2	253
9	0.45	14.7	0.2	2	345
10	0.36	11.8	0.2	2	140
11	0.37	12.4	0.2	2	169
12	0.26	8.6	0.2	2	74
13	0.35	11.8	0.3	1	27
14	0.35	11.8	0.3	1	27
15	0.32	10.6	0.3	1	17
16	0.30	10.2	0.3	1	17
17	0.43	14.2	0.3	1	71
18	0.43	14.2	0.3	1	71
19	0.50	16.4	0.3	1	72
20	0.33	11.1	0.3	2	13

Table 4.13. Kilyos CSS Test Results for 50 Kpa Consolidation Pressure (cont).

Sample No	$I_D$	$\psi_p$	SRA	CP (sec)	NCL
21	0.39	13.1	0.3	2	29
22	0.43	14.1	0.3	2	42
23	0.36	11.9	0.3	2	20
24	0.50	16.5	0.3	2	110
25	0.46	15.3	0.3	2	76
26	0.37	12.4	0.3	2	30

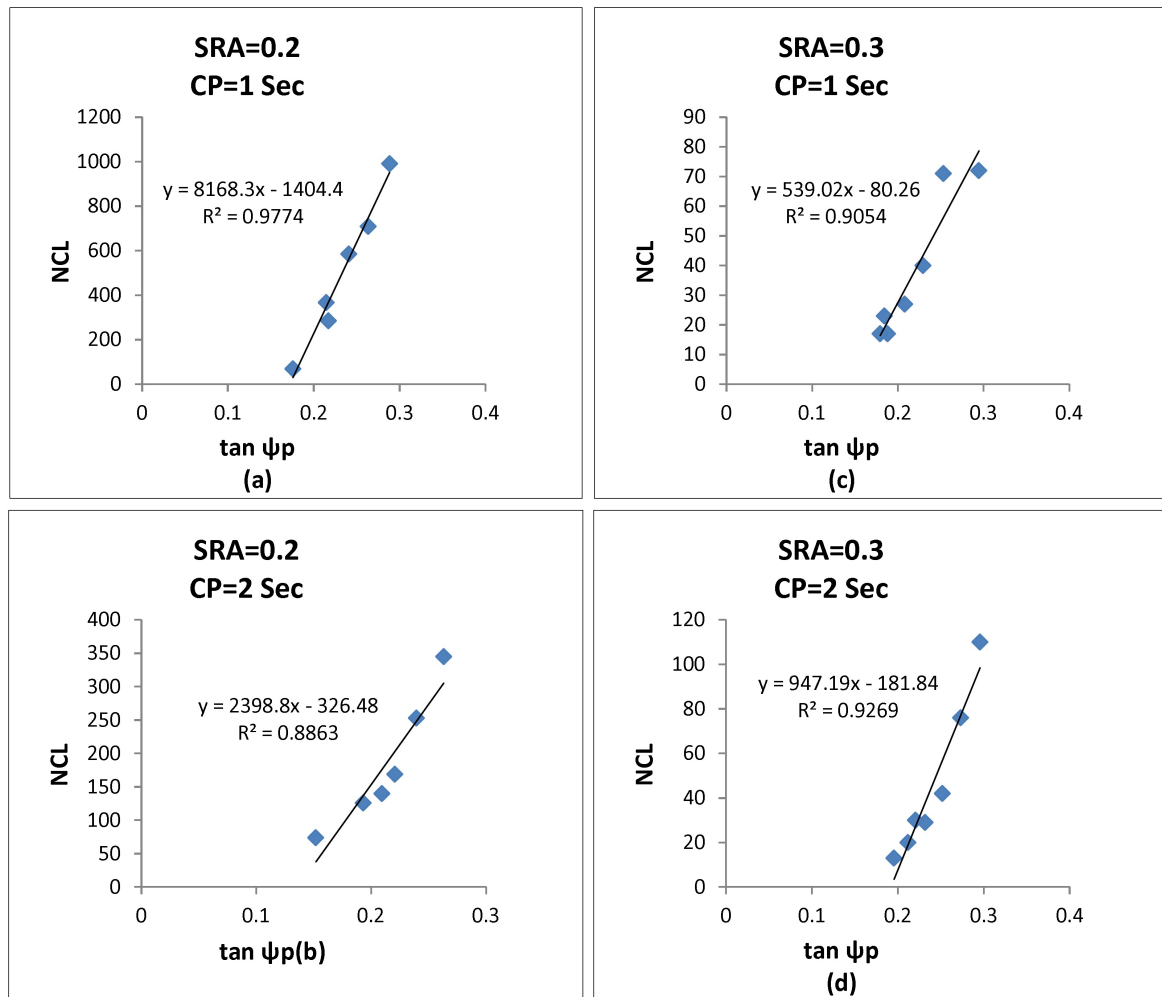
Figure 4.14. Kilyos  $\tan \psi_p$ - NCL (Consolidation pressure= 50 kpa).

Table 4.14. Kilyos CSS Test Results for 100 Kpa Consolidation Pressure.

Sample No	$I_D$	$\psi_p$	$SRA$	$CP(sec)$	$NCL$
1	0.22	7.2	0.2	1	285
2	0.18	6.1	0.2	1	180
3	0.21	6.9	0.2	1	267
4	0.15	5.1	0.2	1	105
5	0.23	7.6	0.2	1	310
6	0.29	9.6	0.2	1	417
7	0.18	6.0	0.2	2	103
8	0.22	7.2	0.2	2	151
9	0.35	11.6	0.2	2	318
10	0.28	9.3	0.2	2	268
11	0.45	14.8	0.2	2	510
12	0.51	16.8	0.2	2	525
13	0.30	9.9	0.3	1	54
14	0.36	12.1	0.3	1	68
15	0.13	4.3	0.3	1	15
16	0.20	6.8	0.3	1	34
17	0.32	10.7	0.3	1	55
18	0.23	7.6	0.3	1	38
19	0.20	6.5	0.3	2	44
20	0.23	7.8	0.3	2	51
21	0.28	9.3	0.3	2	66
22	0.45	14.8	0.3	2	175
23	0.36	12.1	0.3	2	116
24	0.36	12.1	0.3	2	116

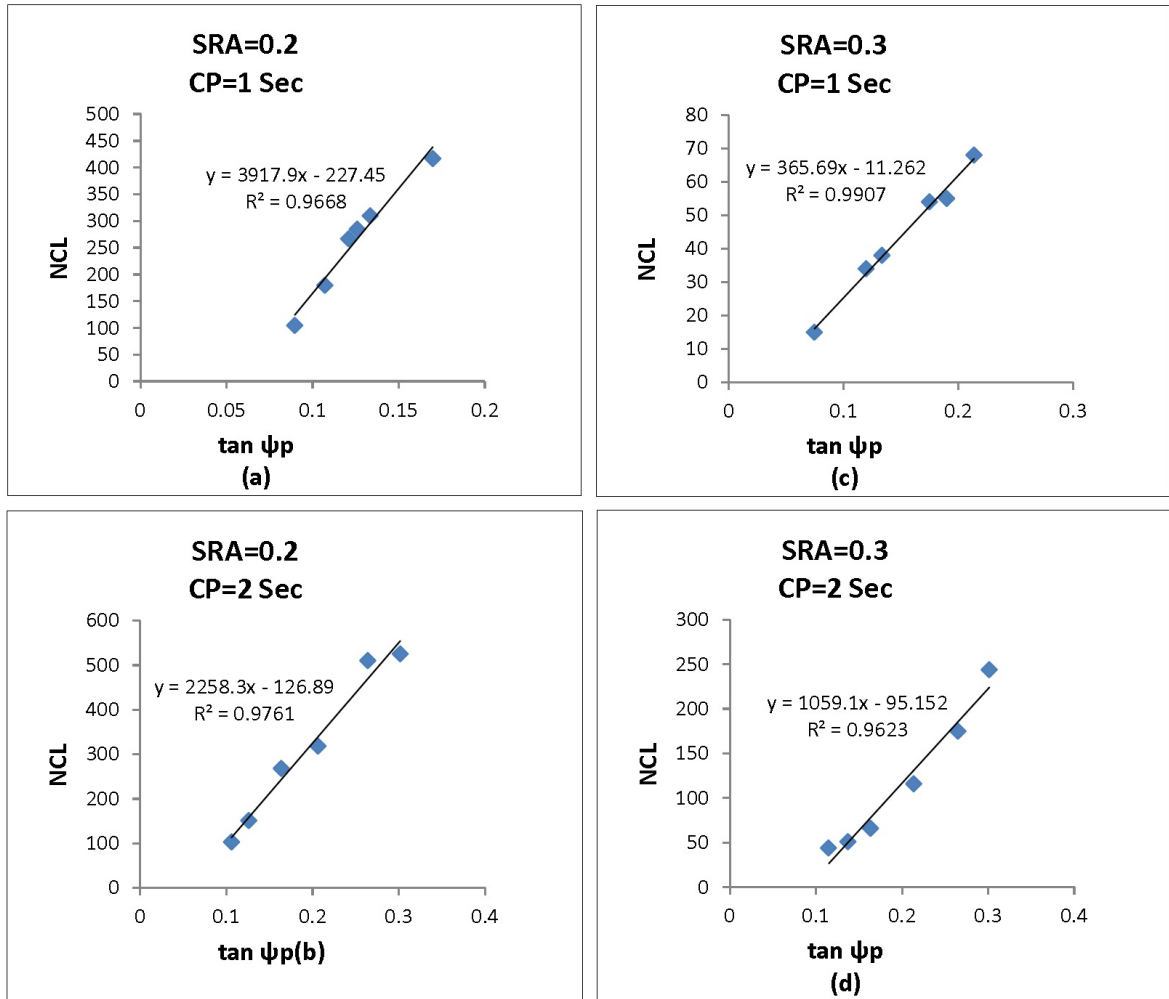


Figure 4.15. Kilyos  $\tan \psi_p$ -  $NCL$  (Consolidation pressure= 100 kpa).

Table 4.15. Kilyos CSS Test Results for 150 Kpa Consolidation Pressure.

Sample No	$I_D$	$\psi_p$	$SRA$	$CP(sec)$	$NCL$
1	0.30	9.9	0.2	1	253
2	0.24	8.1	0.2	1	321
3	0.41	13.5	0.2	1	572
4	0.22	7.3	0.2	1	192
5	0.35	11.7	0.2	1	488
6	0.50	16.4	0.2	1	867
7	0.22	7.1	0.2	2	164
8	0.30	10.1	0.2	2	242
9	0.28	9.2	0.2	2	243
10	0.39	12.8	0.2	2	322
12	0.53	17.2	0.2	2	700
13	0.49	16.0	0.2	2	581
14	0.42	13.9	0.2	2	417
15	0.19	6.5	0.3	1	36
16	0.39	12.8	0.3	1	130
17	0.34	11.1	0.3	1	101
18	0.42	13.7	0.3	1	141
19	0.26	8.5	0.3	1	78
20	0.32	10.7	0.3	1	85
21	0.30	9.9	0.3	2	37
22	0.33	10.9	0.3	2	65
23	0.41	13.5	0.3	2	105
24	0.26	8.7	0.3	2	32
25	0.46	15.1	0.3	2	133
26	0.36	12.0	0.3	2	57

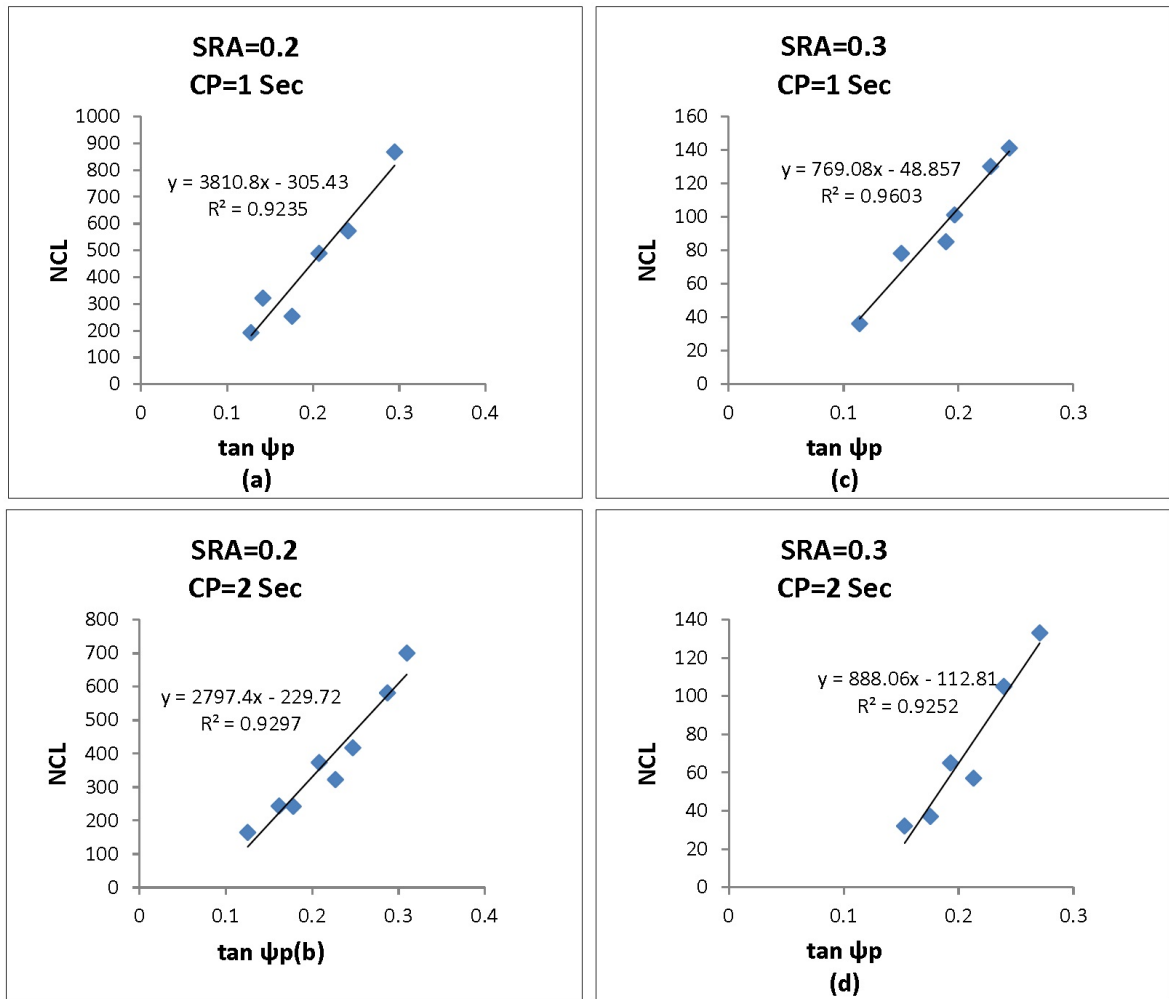


Figure 4.16. Kilyos  $\tan \psi_p$ -  $NCL$  (Consolidation pressure= 150 kpa).

Kilyos sand shows the same behavior as Akpınar and Sile sand in almost all cases. For the two loading conditions with the same SRA and differing CPs, the increase in liquefaction resistance with increase in dilation angle is higher for the smaller CP. Also, for the two loading condition with the same CP and differing SRAs, the increase in liquefaction resistance with increase in dilation angle is higher for the smaller SRA. Unless for samples loaded under 150 kPa vertical pressure, where the line slope for samples with same SRA and differing CPs slightly increases with increase in CP. However, still the number of cycles to liquefy for samples with equal dilation angle is greater for loading combination with lower cyclic period.

All in all according to test results, the dilation angle-liquefaction susceptibility relationship is clearly dependent on factors like stress ratio amplitude, cyclic period, and basic characteristics of sands like their shape factor parameters. The experimental results will be thoroughly studied in the next chapter.



## 5. DISCUSSION

In the previous chapter, the data obtained from all test tests were given. Tthe following lists the summary of the results that can be viewed in the previous chapter:

- (i) Average circularity and roundness values for each of three sand type.
- (ii) Cinicioglu and Abadkon [30] relationships needed to calculate test samples' dilation angles based on the pre-shear relative density and confinement pressure.
- (iii) Critical state friction angles of all sand types.
- (iv) Peak dilation angle of each cyclic simple shear test specimen calculated using Cinicioglu and Abadkon [30] relationship.
- (v) Results of CSS tests for 4-different combinations of Stress Ratio Amplitude and Cyclic Period, conducted on specimens consolidated under 50 Kpa, 100 Kpa or 150 kPa vertical pressure.
- (vi) Number of cycles needed for each specimen to liquefy.

In this chapter, test results of three sand types will be investigated and compared to each other to observe their differences and to understand the potential underlying causes of these differences. First the influence of particle shapes on friction angle will be observed in order to see if the results coincide with previous studies. Then the effects of shape factors on  $\alpha_\psi$  and  $m_\psi$  values of the relationship purposed by Cinicioglu and Abadkon [30] will be discussed. Next, influence of dilatancy on liquefaction resistance will be investigated. For this purpose, dilatancy angle-number of cycles to liquefy (NCL) relationships for all three sand types will be shown. These relationships are plotted for tests that have the same stress ratio amplitude (SRA) and cyclic period (CP). Then, obtained relationships will be investigated to observe the possible influence of particle shapes on the behavior. A normalizing method will be purposed in order to eliminate the effect of vertical stress on liquefaction susceptibility criteria. Finally, using the normalized number of cycles to liquefy (NNCL), dilatancy angle-(NNCL) relationships will be plotted. These relationships are plotted for tests that have either the same SRA, to see the CP influence, or have the same CP, to see the SRA influence.

### 5.1. Influence of Particle Shape on Critical State Friction Angle

Cho *et al.* [35] investigated an immense database derived out of new experimental data and data from previously published studies. They concluded that critical state friction angle ( $\phi_{cs}$ ) increases with the increasing angularity.

Sand types studied in this thesis show the same behavior (Table 5.1). However, the difference in the friction angle values is slight, which is expectable considering that the differences in shape factors are relatively small.

Table 5.1. Circularity, Roundness and Critical State Friction Angle of Sand Types.

Sand Type	Circularity	Roundness	$\phi_{cs}$
Sile	0.674	0.725	33.7
Akpinar	0.716	0.728	31.2
Kilyos	0.743	0.759	31

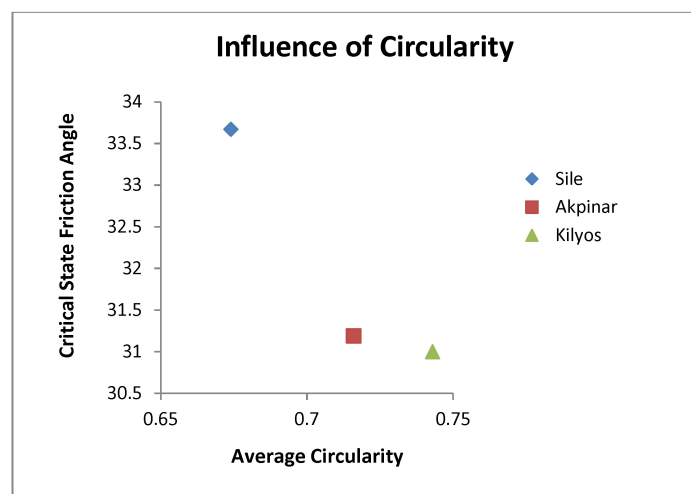


Figure 5.1. Influence of Circularity on Critical State Friction Angle.

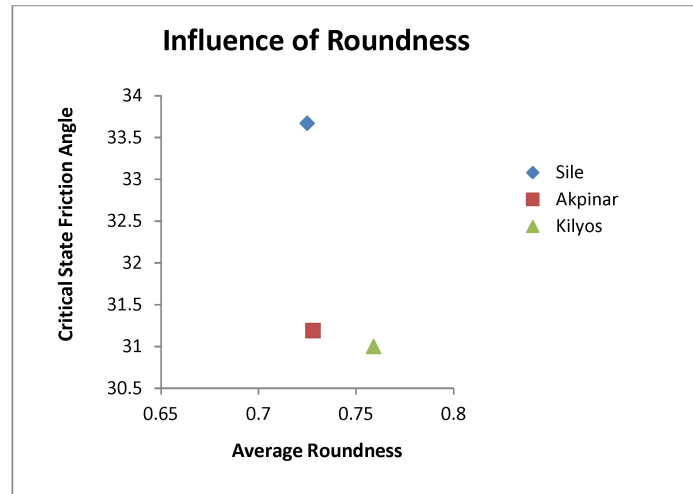


Figure 5.2. Influence of Roundness on Critical State Friction Angle.

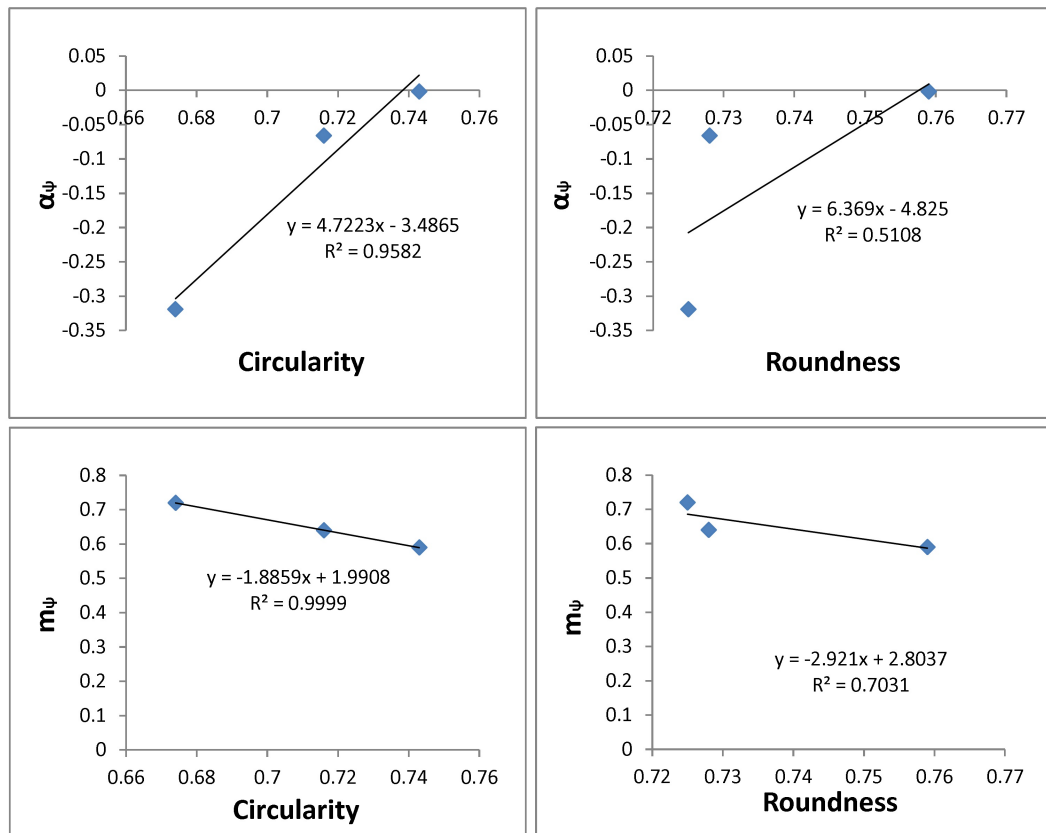
## 5.2. Influence of Shape Factor on Dilatancy Angle

The influence of shape factors on dilatancy angle has received wide attention in recent years. Alshibli and Alsaleh [34] found that as the surface roughness increases, the friction and dilatancy angles of the sands also increase. Cho *et al.* [35] determined that a decrease in sphericity and/or roundness leads to , increase in  $\phi'_{cs}$ , and increase in the critical state line intercept. Guo and Su [36] determined that particle angularity has a significant influence on the peak friction angle and dilatancy. However, the empirical equation proposed by Cinicioglu and Abadkon [30] is a new method that allows the calculation of dilatancy angle as a function of in-situ relative density  $I_D$  and confinement pressure  $p'_i$ . Thus, using this equation with the results from three different sand types, the effect of particle shape on dilation angle is investigated in this study.

As shown in Table 5.2, absolute  $\alpha_\psi$  values decrease as the particle circularity and roundness increase. Likewise,  $m_\psi$  values decrease as the particle circularity and roundness increase.

Table 5.2. Circularity, Roundness,  $\alpha_\psi$  and  $m_\psi$  of Sand Types.

Sand Type	Circularity	Roundness	$\alpha_\psi$	$m_\psi$
Sile	0.674	0.725	-0.319	0.72
Akpinar	0.716	0.728	-0.066	0.64
Kilyos	0.743	0.759	-0.0017	0.59

Figure 5.3. Influence of Particle Circularity and Roundness on  $\alpha_\psi$  and  $m_\psi$  values.

Graphs in Figure 5.3 show that there is a linear relationship between circularity values and the constant values,  $\alpha_\psi$  and  $m_\psi$ . However the relationship between roundness values and the constant values is not as well-defined. Further investigation on more sand types is needed in order to derive a probable correlation between shape factors (circularity and roundness) and dilation angle equation constant values ( $\alpha_\psi$  and  $m_\psi$ ).

### 5.3. Influence of Vertical Pressure on Liquefaction Susceptibility

As mentioned before, Kilyos sand samples were tested with different combinations of stress ratio amplitude and cyclic period. These samples were prepared by consolidating under different vertical stresses (50 kPa, 100 kPa and 150 kPa), in order to observe the effect of applied vertical stress on liquefaction resistance.

The most suitable way of examining the influence of one variable on behavior is to vary that variable while keeping all the other influential variables constant between tests. While the influence of vertical pressure on the  $\psi_p$ - $NCL$  relationship is examined, it is necessary to quantify the  $\psi_p$ - $NCL$  relationship for different vertical stress magnitudes. Other variables (shear stress and frequency of loading) are kept constant.

At our disposal, there are two sets which can be used to analyze the influence of vertical stress on liquefaction resistance with the intended procedure. The first set of tests are conducted under 100 kPa vertical stress with 0.3 stress ratio amplitude, and the second set contains tests that conducted under 150 kPa vertical stress with 0.2 stress ratio amplitude. As a result, both sets contain tests that were conducted with 30 kPa as the initial shear stress (ignoring the fact that, the initial magnitude of shear stress varies throughout the test to keep the stress ratio constant). The initial expectation here is to see that for the same shear stress magnitude, the results would yield the same  $\psi_p$ - $NCL$  relationships even though the applied vertical stresses are different

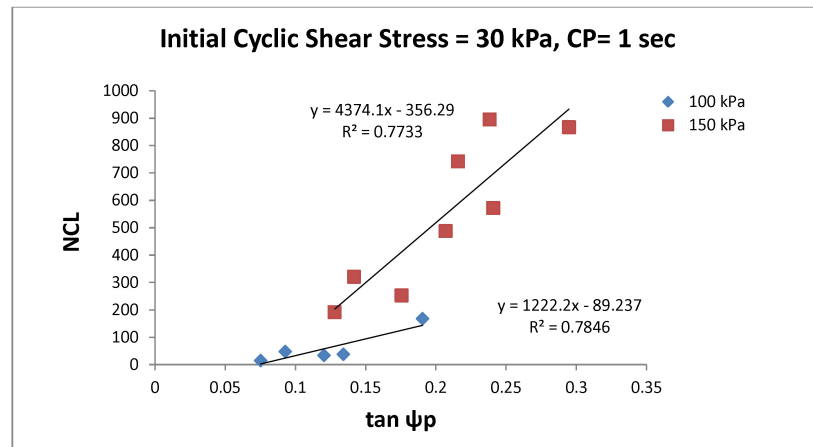


Figure 5.4. Kilyos  $\tan \psi_p$ - $NCL$  Relationship, Initial Shear Stress=30 kPa, CP=1 sec.

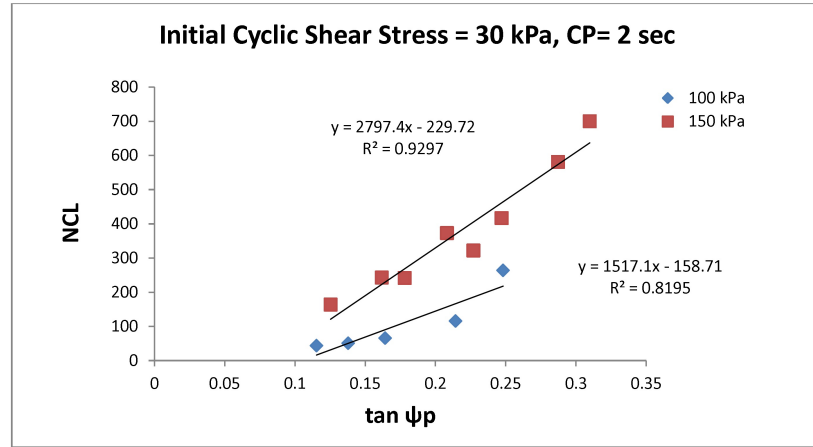


Figure 5.5. Kilyos  $\tan \psi_p$ - $NCL$  Relationship, Initial Shear Stress=30 kPa, CP=2 sec.

As can be seen in Figures 5.4 and 5.5, even for the same dilation angle, which encompasses the effect of relative density and confinement pressure, and initial cyclic shear stress, the results show a considerable discrepancy in the number of cycles needed for the sample to liquefy. That is because although dilation angle does include the effect of confinement pressure, the excess pore water pressure that should be generated in each specimen for effective vertical stress to become zero is different for each loading condition. In the samples vertically loaded up to 100 kPa, 100 kPa excess PWP should be generated whereas in the ones loaded up to 150 kPa this excess PWP is 150 kPa. Thus, for samples that have the same peak dilatancy angle, stress ratio amplitude control liquefaction resistance. For two samples with the same  $\psi_p$ , the one with the greater SRA requires less number of cycles to reach initial liquefaction.

To eliminate this diversity, the numbers of cycles for the specimen to liquefy were normalized with respect to the vertical stress applied on them. The applied vertical stress values were also normalized with respect to atmospheric pressure. Having both confinement pressure value in dilation angle formula and the vertical stress normalized with respect to the atmospheric pressure, the relationship is unit-independent.

Normalized number of cycles to liquefy (NNCL) is defined as:

$$NNCL = \frac{\text{Number of Cycles to Liquefy}}{\frac{\text{Vertical Stress}}{\text{Atmospheric Pressure}}} \quad (5.1)$$

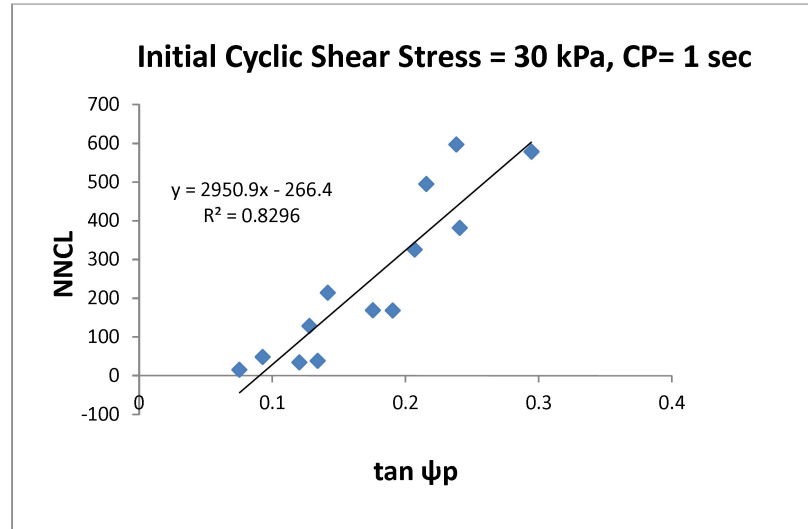


Figure 5.6. Kilyos  $\tan \psi_p$ -NNCL Relationship, Initial Shear Stress=30 kPa, CP=1 sec.

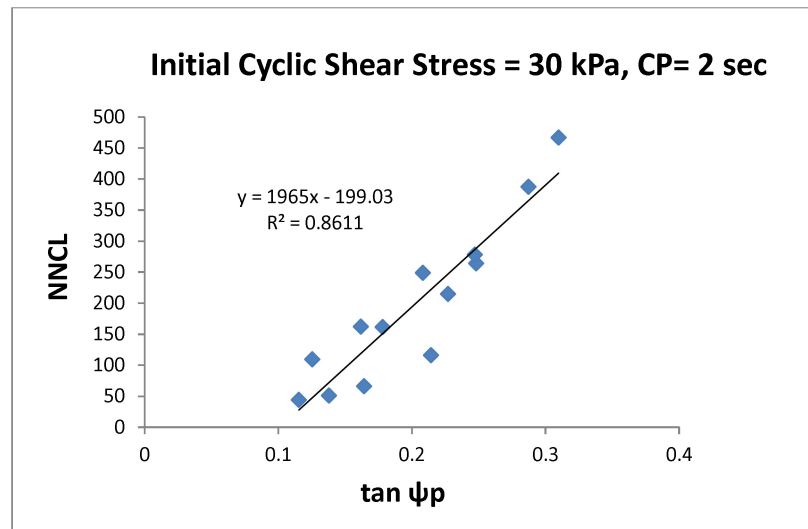


Figure 5.7. Kilyos  $\tan \psi_p$ -NNCL Relationship, Initial Shear Stress=30 kPa, CP=2 sec.

As shown in Figures 5.6 and 5.7, there is a single linear relationship between dilation angle and normalized number of cycles to liquefy (NNCL) depending on cyclic shear stress and cyclic period. This property can be used to compare the liquefaction potential of soil samples under different consolidation pressures, according to their dilation angle. However further investigation is needed to see the effect of over consolidation ratio on the relationship since in this study all the specimens were normally consolidated.

#### 5.4. Liquefaction Potential of Sands with Regard to Dilation angle

CSS tests were conducted on normally consolidated sand samples. All three sand types were consolidated under 50 kPa and 100 kPa vertical pressure. Comparing the dilation angle - liquefaction susceptibility relationship of different sands with the same consolidation pressure will show the effect of shape factors on this relationship.

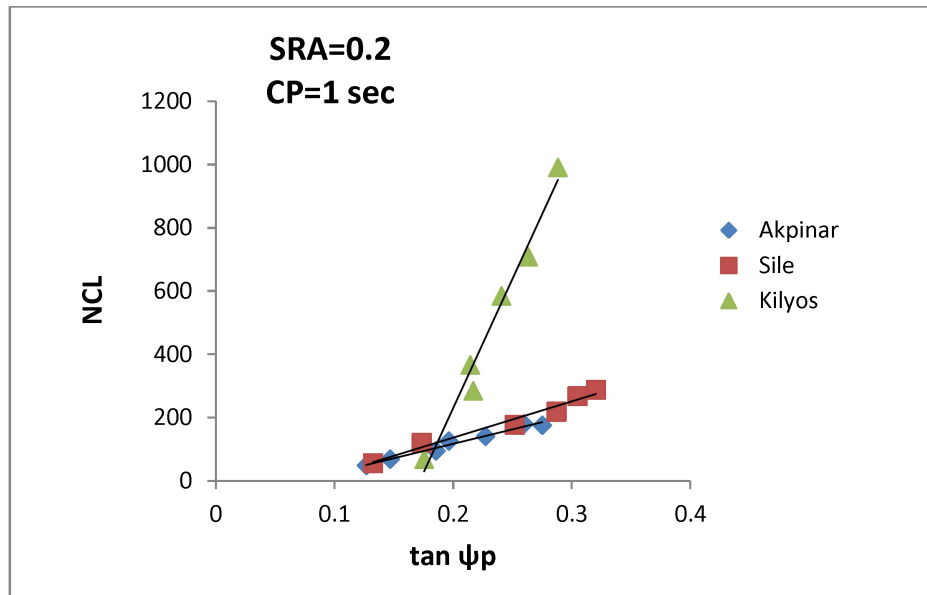


Figure 5.8.  $\tan \psi_p$ -NNCL Relationships, Vertical Stress=50 kPa, SRA=0.2, CP=1 sec.



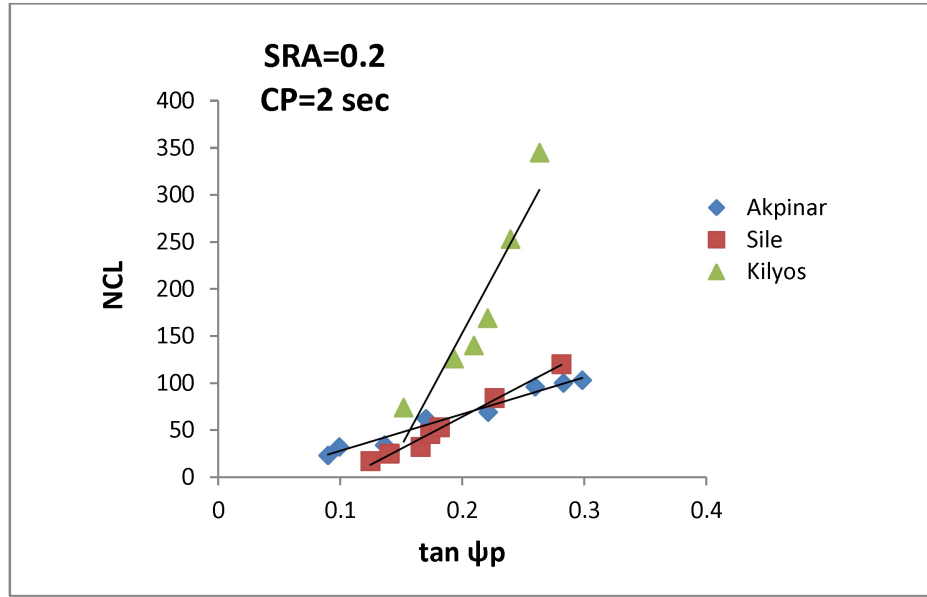


Figure 5.9.  $\tan \psi_p$ - $NNCL$  Relationships, Vertical Stress=50 kPa, SRA=0.2, CP=2 sec.

According to the provided graphs, for the same dilation angle values in Sile and Akpınar sands, the liquefaction resistance is mainly similar, however in some loading combinations the number of cycles to liquefy are slightly higher for Sile sand, which is expected because of the more angular particles. On the other hand, Kilyos sand has significantly higher liquefaction resistance in all loading combinations. Nevertheless for the samples under same loading conditions we would expect the particles with higher circularity and roundness to have higher liquefaction potential. This peculiarity might have been caused by surface roughness or the mineral characteristics of Kilyos sand, which were not considered in this study. Moreover,  $K_o$  values of Kilyos sand are much greater than the other two sands. Therefore, confinement for Kilyos sand is significantly greater compared to Akpınar and Sile sands. Thus, stress ratio amplitude, when calculated as  $\frac{\tau}{p'_i}$ , is relatively lower in case of Kilyos sand, which possibly lead to seemingly greater liquefaction resistance.

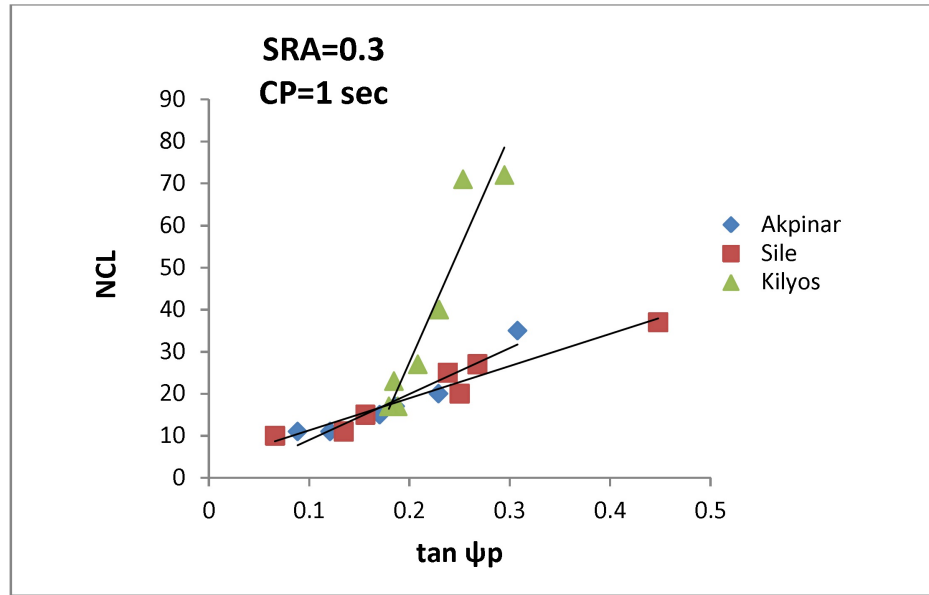


Figure 5.10.  $\tan \psi_p$ - $NNCL$  Relationships, Vertical Stress=50 kPa, SRA=0.3, CP=1 sec.

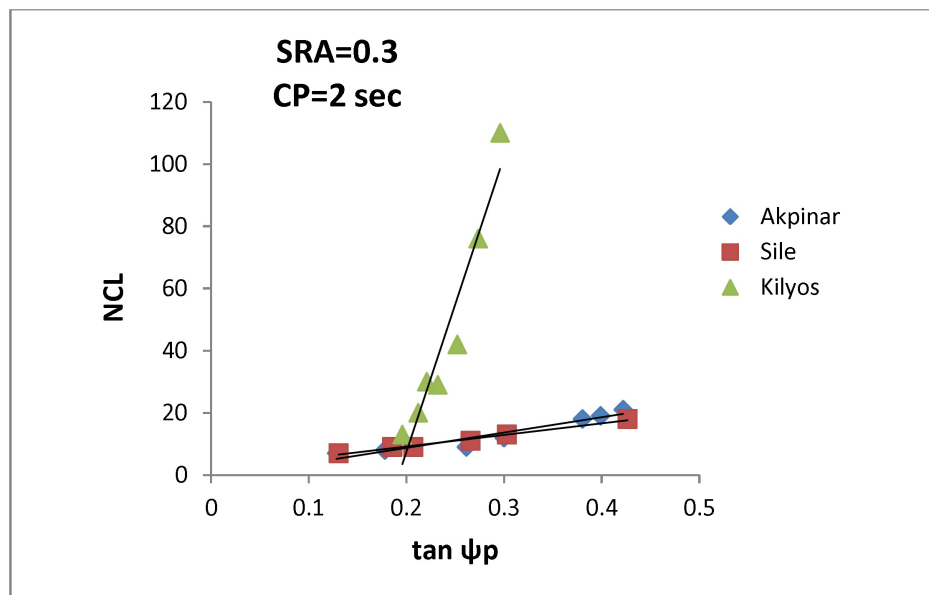


Figure 5.11.  $\tan \psi_p$ - $NNCL$  Relationships, Vertical Stress=50 kPa, SRA=0.3, CP=2 sec.

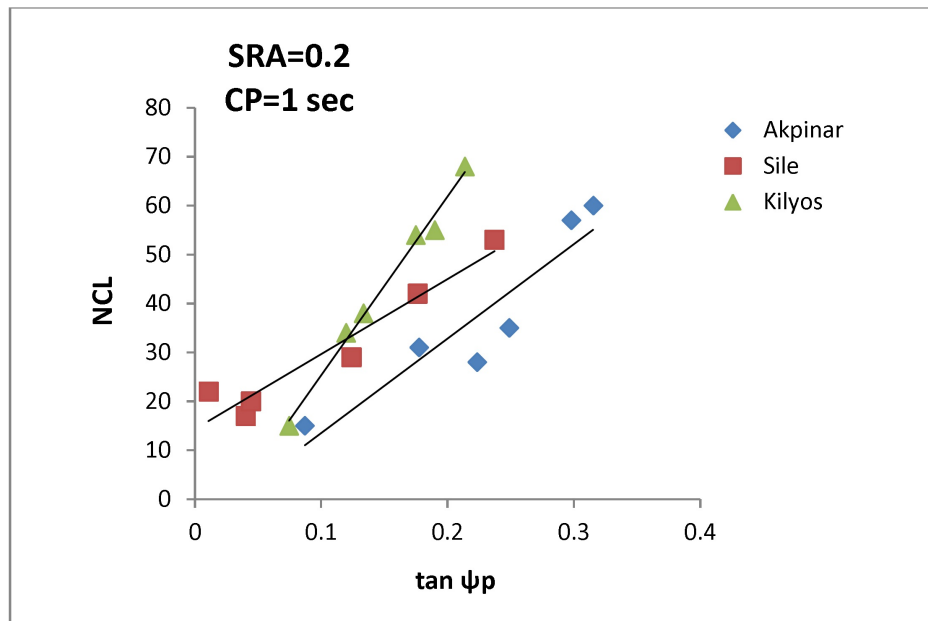


Figure 5.12.  $\tan \psi_p$ - $NNCL$  Relationships, Vertical Stress=100 kPa, SRA=0.2, CP=1 sec.

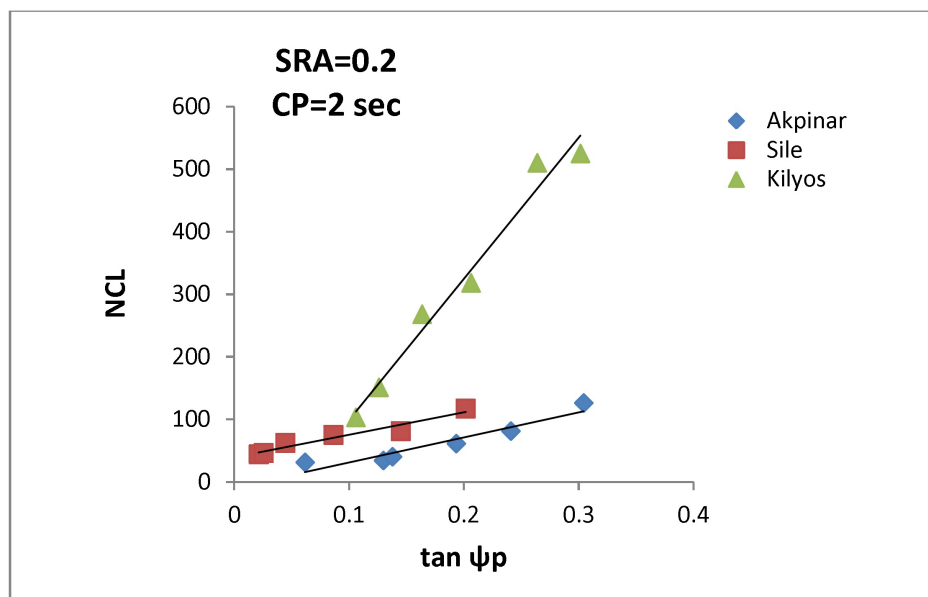


Figure 5.13.  $\tan \psi_p$ - $NNCL$  Relationships, Vertical Stress=100 kPa, SRA=0.2, CP=2 sec.

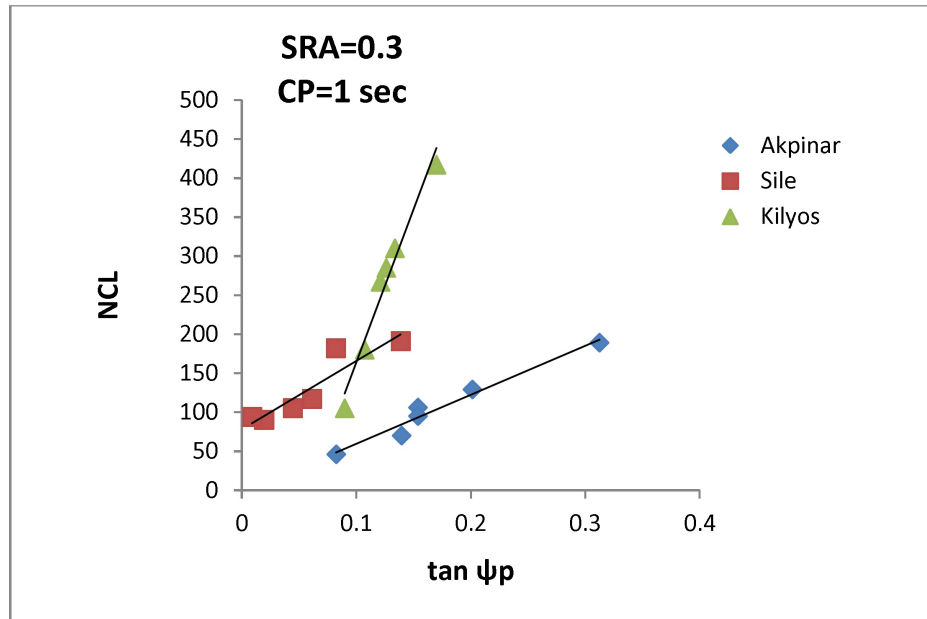


Figure 5.14.  $\tan \psi_p$ - $NNCL$  Relationships, Vertical Stress=100 kPa, SRA=0.2, CP=2 sec.

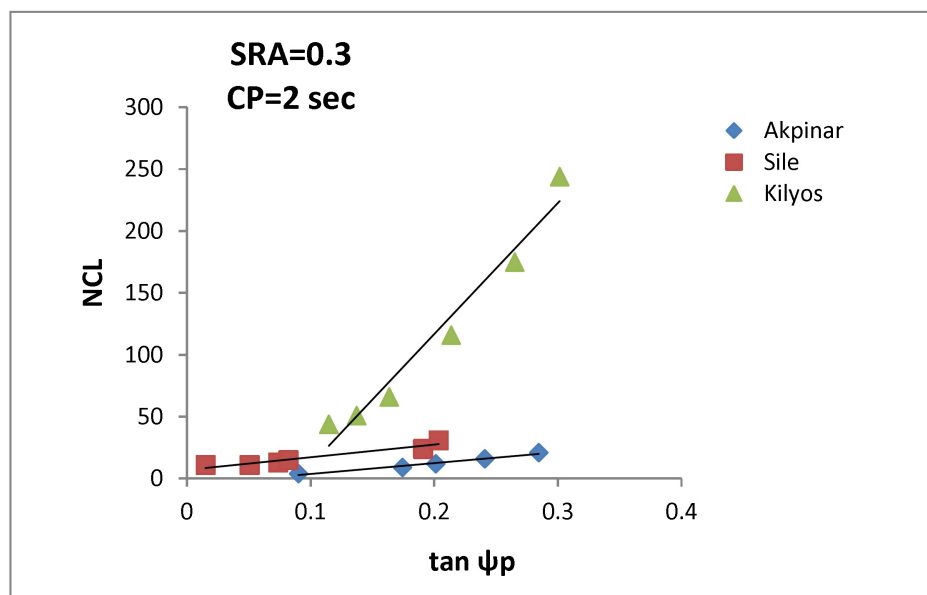


Figure 5.15.  $\tan \psi_p$ - $NNCL$  Relationships, Vertical Stress=100 kPa, SRA=0.3, CP=1 sec.

### 5.5. Influence of Stress Ratio Amplitude on Liquefaction Susceptibility

CSS tests were conducted on each of 3 sand types either with 1 or 2 seconds of CP. For each CP value,  $\tan \psi_p$ - $NNCL$  relationships are plotted for both SRA values. Plots for different SRAs are shown on the same graphs. The results show that  $\tan \psi_p$ - $NNCL$  relationships are dependent on the applied SRA regardless of the initial cyclic shear stress value.

#### 5.5.1. Akpinas Sand SRA Effect

Akpinar sand samples loaded with SRA=0.2 were loaded horizontally with either 10 kPa or 20 kPa initial cyclic shear stress (Figures 5.16 and 5.17, blue points), where the initial cyclic shear stress applied on the samples with SRA=0.3 was either 15 kPa or 30 kPa (Figures 5.16 and 5.17, red points). As it is clear in the graphs, for a constant cyclic period and same dilation angle,  $NNCL$  is significantly higher for tests with SRA=0.2.

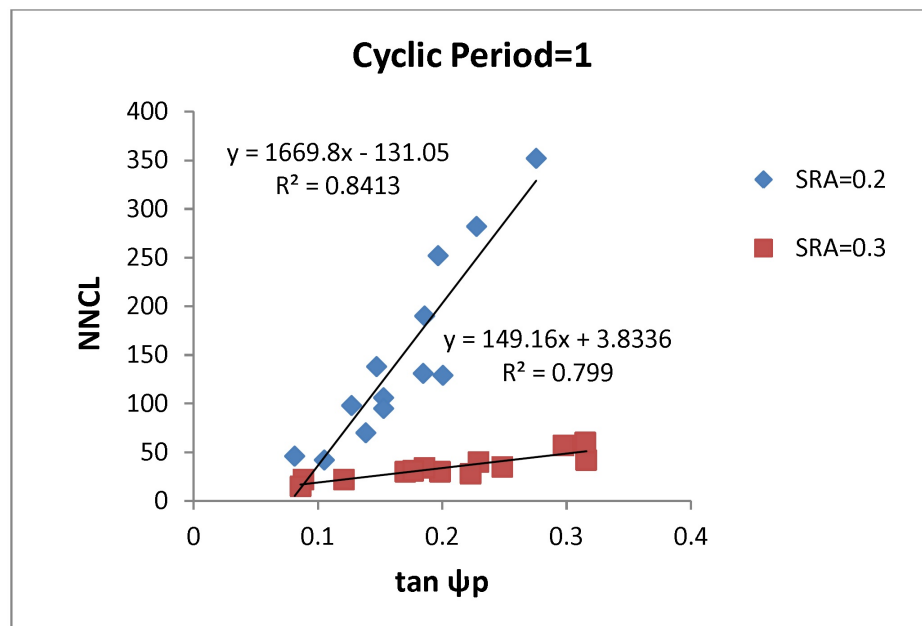


Figure 5.16. Akpinar Sand SRA Effect on  $\tan \psi_p$ - $NNCL$  Relationships, CP=1 sec.

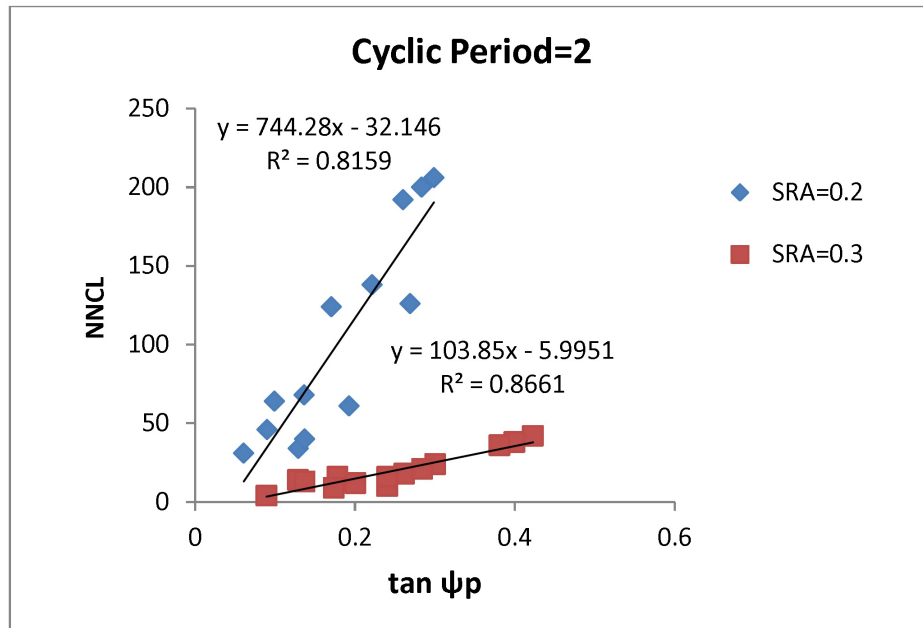


Figure 5.17. Akpinar Sand SRA Effect on  $\tan \psi_p$ - $NNCL$  Relationships, CP=2 sec.

### 5.5.2. Sile Sand SRA Effect

Sile sand samples loaded with SRA=0.2 were loaded horizontally with either 10 kPa or 20 kPa initial cyclic shear stress (Figures 5.18 and 5.19, blue points), where the initial cyclic shear stress applied to the samples with SRA=0.3 was either 15 kPa or 30 kPa (Figures 5.18 and 5.19, red points). Like in the case of Akpinar sand, in Sile sand samples for a constant CP and same dilation angle, NNCL is significantly higher for tests with SRA=0.2.

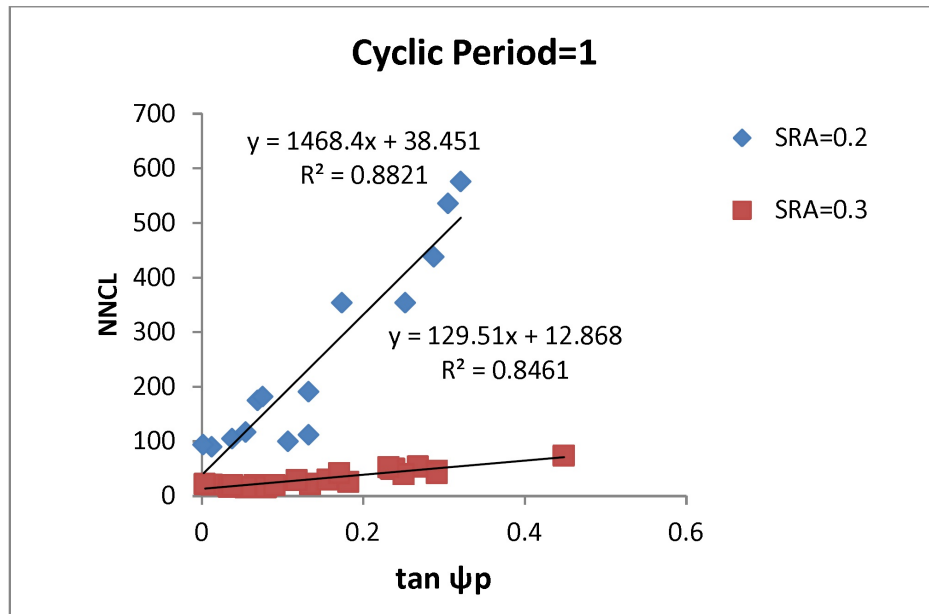


Figure 5.18. Silty Sand SRA Effect on  $\tan \psi_p$ - $NNCL$  Relationships, CP=1 sec.

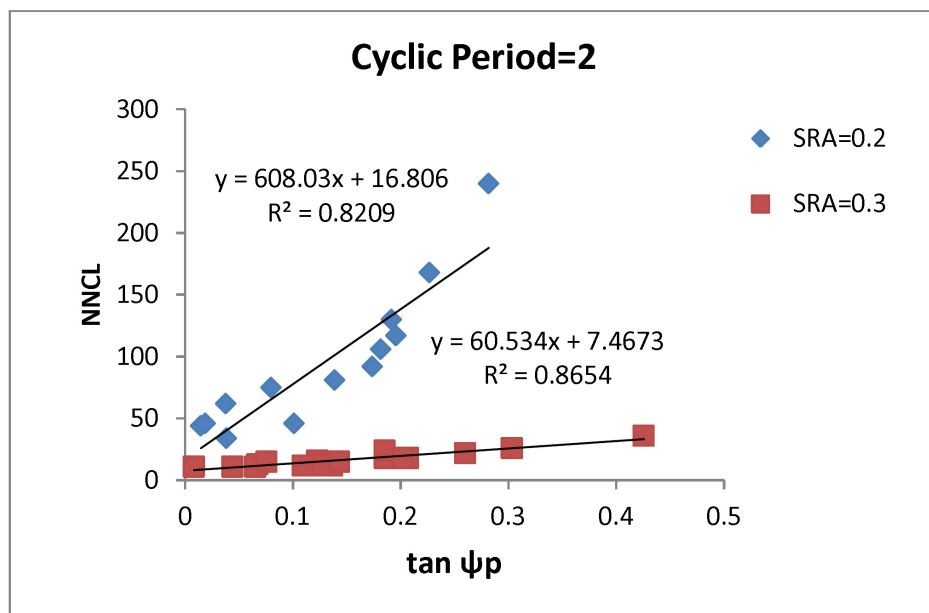


Figure 5.19. Silty Sand SRA Effect on  $\tan \psi_p$ - $NNCL$  Relationships, CP=2 sec.

### 5.5.3. Kilyos Sand SRA Effect

Kilyos sand samples loaded with  $SRA=0.2$  were loaded horizontally with either 10 kPa, 20 kPa or 30 kPa initial cyclic shear stress (Figures 5.20 and 5.21, blue points), where the initial cyclic shear stress applied to the samples with  $SRA=0.3$  was either 15, 30 or 45 kPa (Figures 5.20 and 5.21, red points).

In section 5.3 it was shown that samples with 30 kPa cyclic shear stress lie on the same line with respect to the cyclic period of loading. Here, it can be seen that sand samples for a constant cyclic period and same dilation angle, NNCL is significantly higher for tests with  $SRA=0.2$  for Kilyos sand too.

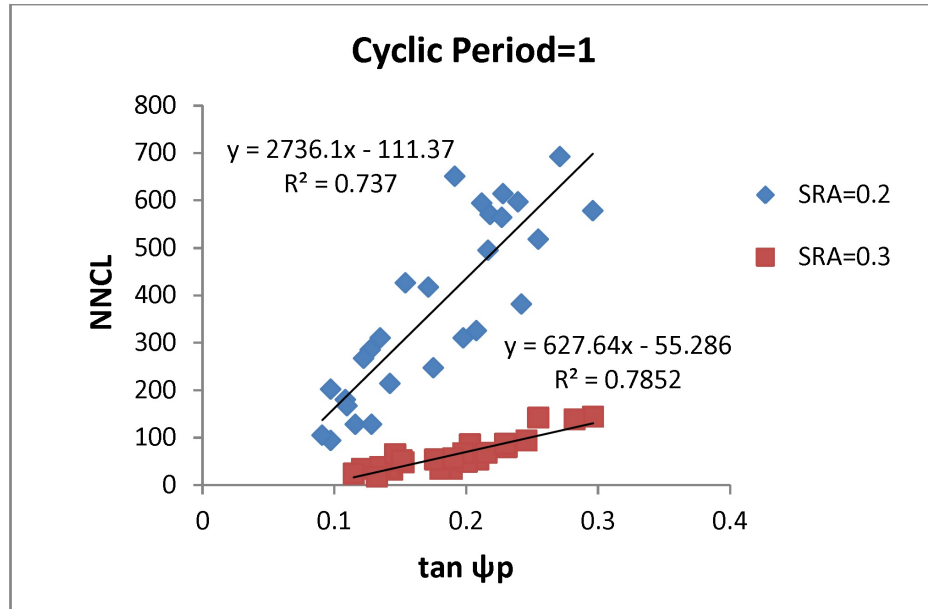


Figure 5.20. Kilyos Sand SRA Effect on  $\tan \psi_p$ -NNCL Relationships, CP=1 sec.

It seems like there is a general behavior in all sand types with respect to stress ratio amplitude when the loading cyclic period is kept constant. In the next section, this effect will be numerically studied.



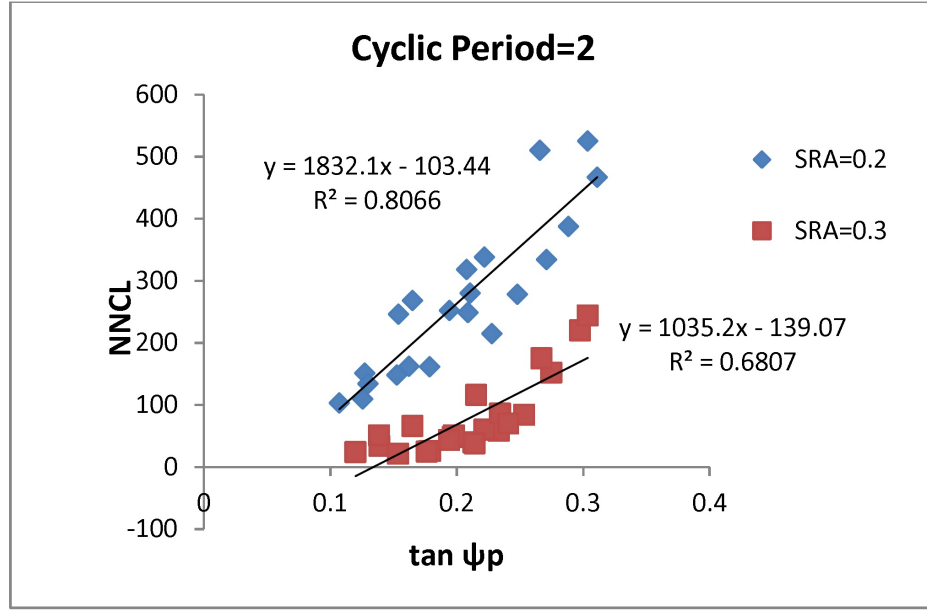


Figure 5.21. Kilyos Sand SRA Effect on  $\tan \psi_p$ - $NNCL$  Relationships, CP=2 sec.

#### 5.5.4. Comparing SRA Effects

In this study, in order to investigate the effect of SRA and compare this effect on different sand types, normalized number of cycles to liquefy ratio for a specific cyclic period was defined as:

$$(NNCL)_{CP} = \frac{NNCL_{for SRA = 0.2}}{NNCL_{for SRA = 0.3}} \quad (5.2)$$

where CP refers to cyclic period, meaning that cyclic period should be kept constant (either 1 sec or 2 sec).

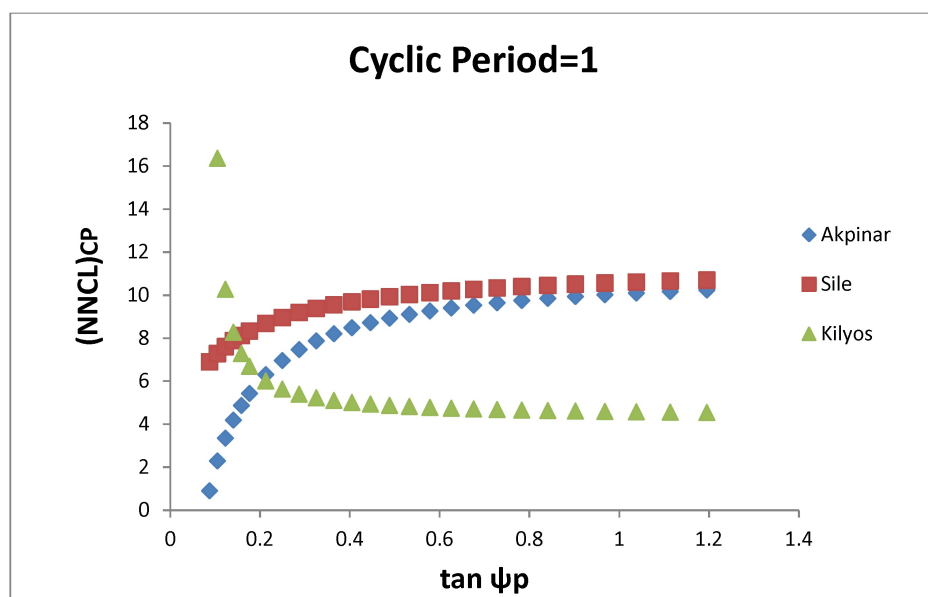
Investigating the  $\tan \psi_\phi - (NNCL)_{CP}$  for each specific cyclic period (1 and 2 sec) shows that the effect of SRA either decreases or increases with increasing dilation angle, depending on the sand type and cyclic period. However, the  $\tan \psi_\phi - (NNCL)_{CP}$  variation slope tends to become zero with increase in dilation angle.

Table 5.3. Comparing SRA Effects for CP=1 sec.

Sand Type	Line equation for SRA=0.2	Line equation for SRA=0.3
Sile	$NNCL = 1468.4 \tan \psi_p + 38.45$	$NNCL = 129.5 \tan \psi_p + 12.87$
Akpinar	$NNCL = 1669.8 \tan \psi_p - 131.05$	$NNCL = 149.2 \tan \psi_p + 3.83$
Kilyos	$NNCL = 2736.1 \tan \psi_p - 111.37$	$NNCL = 627.6 \tan \psi_p - 55.28$

Table 5.4. Comparing SRA Effects for CP=2 sec.

Sand Type	Line equation for SRA=0.2	Line equation for SRA=0.3
Sile	$NNCL = 608.0 \tan \psi_p + 16.81$	$NNCL = 60.5 \tan \psi_p + 7.47$
Akpinar	$NNCL = 744.3 \tan \psi_p - 32.15$	$NNCL = 103.85 \tan \psi_p - 5.99$
Kilyos	$NNCL = 1832.1 \tan \psi_p - 103.44$	$NNCL = 1035.2 \tan \psi_p - 139.1$

Figure 5.22.  $\tan \psi_p - (NNCL)_{CP}$  Relationships, CP=1 sec.

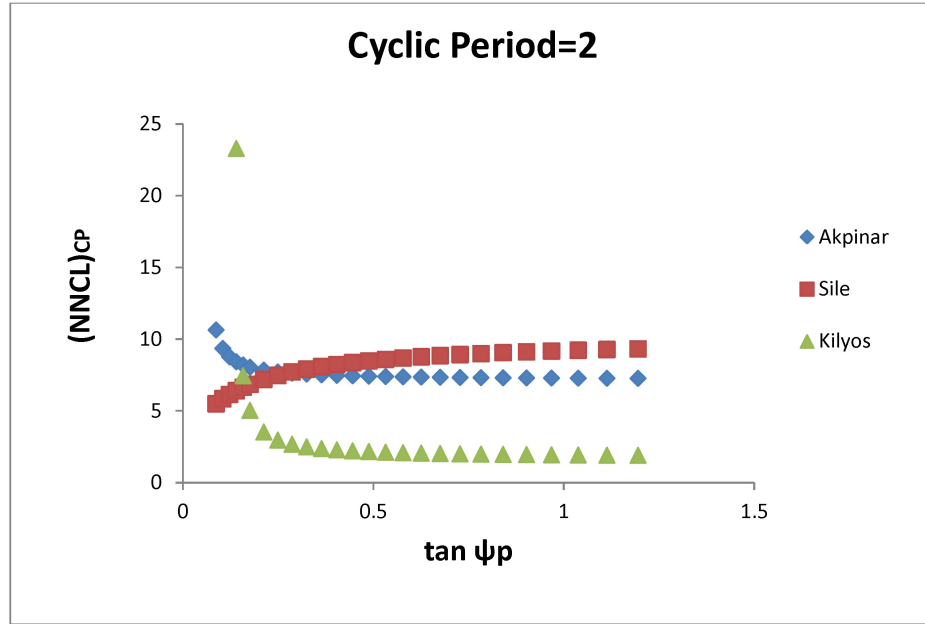


Figure 5.23.  $\tan \tan \psi_p - (NNCL)_{CP}$  Relationships, CP=2 sec.

The final  $(NNCL)_{CP}$  for Akpinar and Sile sands are almost identical. However for both cyclic period values in Kilyos and, final  $(NNCL)_{CP}$  values are significantly lower than this ratio for the other two sand types.

Furthermore, the certain dilation angle values, at which the slopes of above diagrams become almost zero, are so similar for all three sand types, almost 16 degrees for cyclic period = 1 sec and 20 degrees for cyclic period = 2 sec. The changes in  $(NNCL)_{CP}$  are negligible after these dilation angles.

### 5.6. Influence of Cyclic Period on Liquefaction Susceptibility

In the literature, the field results and laboratory results on the dependence of liquefaction on frequency appear to be in conflict. On the one hand existing laboratory results show little frequency-dependence of liquefaction [77] [78], on the other hand in situ studies of seismically instrumented liquefaction sites show an association of liquefaction with low-frequency ground motions [79].

In this study, CSS tests were conducted on specimens of 3 sand types with either 0.2 or 0.3 of stress ratio amplitudes. For each SRA value, all dilation angles and NNCLs for all sand type were plotted on the same graph. The results show that the points separate according to cyclic period values.

#### 5.6.1. Akpinar Sand CP Effect

Akpinar sand samples loaded with SRA=0.2 were loaded horizontally with either 10 kPa or 20 kPa (Figures 5.24 and 5.25, blue points) initial cyclic shear stress, where the initial cyclic shear stress applied to the samples with SRA=0.3 was either 15 kPa or 30 kPa (Figures 5.24 and 5.25, red points).

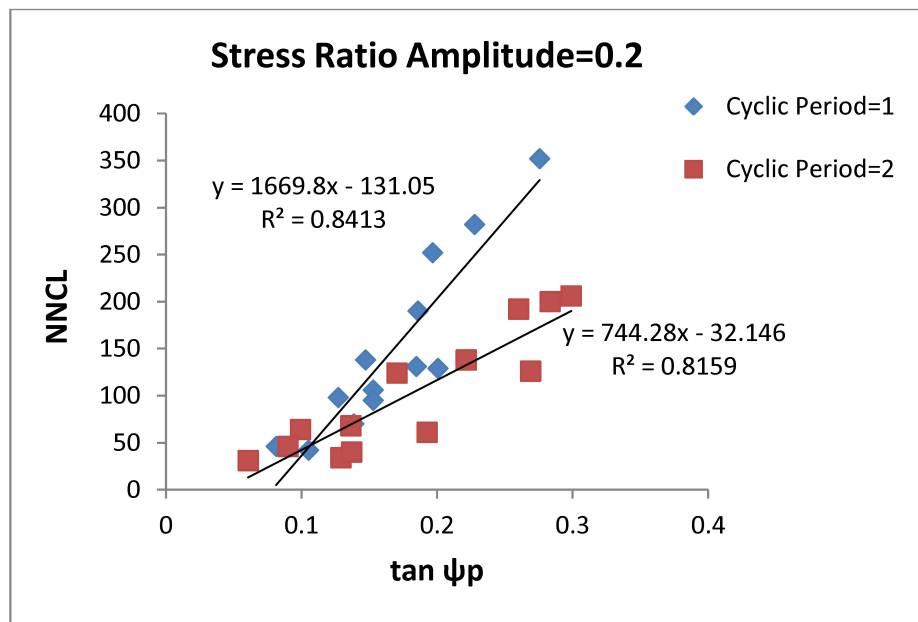


Figure 5.24. Akpinar Sand CP Effect on  $\tan \psi_p$ -NNCL Relationships, SRA=0.2.

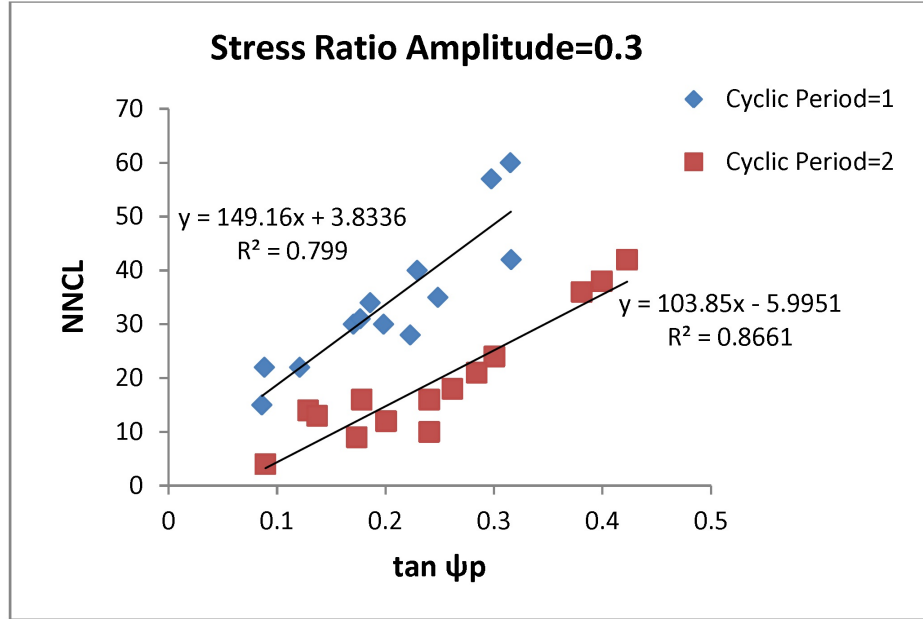


Figure 5.25. Akpinar Sand CP Effect on  $\tan \psi_p$ - $NNCL$  Relationships,  $SRA=0.3$ .

As shown in the graphs for a specific  $SRA$  and same dilation angle,  $NNCL$  is higher for tests with smaller cyclic period.

### 5.6.2. Sile Sand CP Effect

Sile sand samples with  $SRA=0.2$ , also were loaded horizontally with either 10 kPa or 20 kPa (Figures 5.26 and 5.27, blue points) initial cyclic shear stress, where the initial cyclic shear stress applied to the samples with  $SRA=0.3$  was either 15 kPa or 30 kPa (Figures 5.26 and 5.27, red points).

As shown in the graphs (Figure 5.26 and 5.27), for a specific  $SRA$  and same dilation angle,  $NNCL$  is again higher for tests with cyclic period=1.

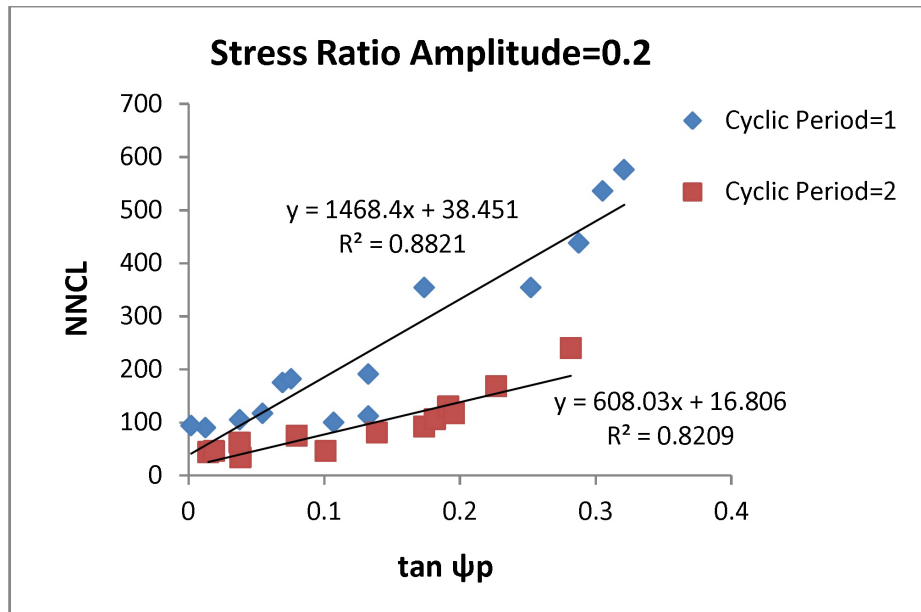


Figure 5.26. Sils Sand CP Effect on  $\tan \psi_p$ - $NNCL$  Relationships,  $SRA=0.2$ .

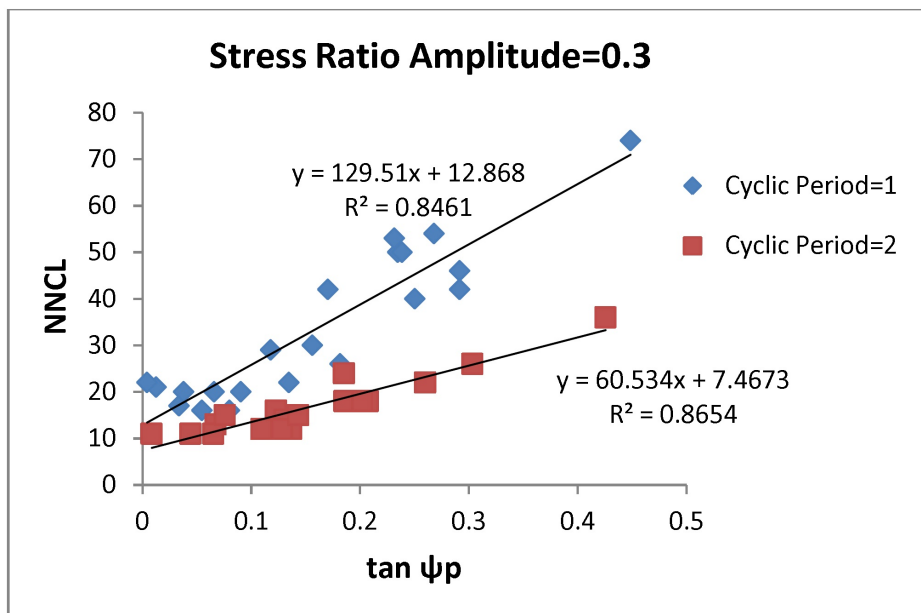


Figure 5.27. Sils Sand CP Effect on  $\tan \psi_p$ - $NNCL$  Relationships,  $SRA=0.3$ .

### 5.6.3. Kilyos Sand CP Effect

Kilyos sand samples with  $SRA=0.2$  were loaded horizontally with either 10 kPa, 20 kPa or 30 kPa (Figures 5.28 and 5.29, blue points) initial cyclic shear stress, where the initial cyclic shear stress applied to the samples with  $SRA=0.3$  was either 15 kPa, 30 kPa or 45 kPa (Figures 5.28 and 5.29, blue points). As shown in the graphs for a specific  $SRA$  and same dilation angle,  $NNCL$  is again higher for tests with cyclic period=1. However in comparison to Akpinar and Sile sands, the effect of cyclic period seems lower.

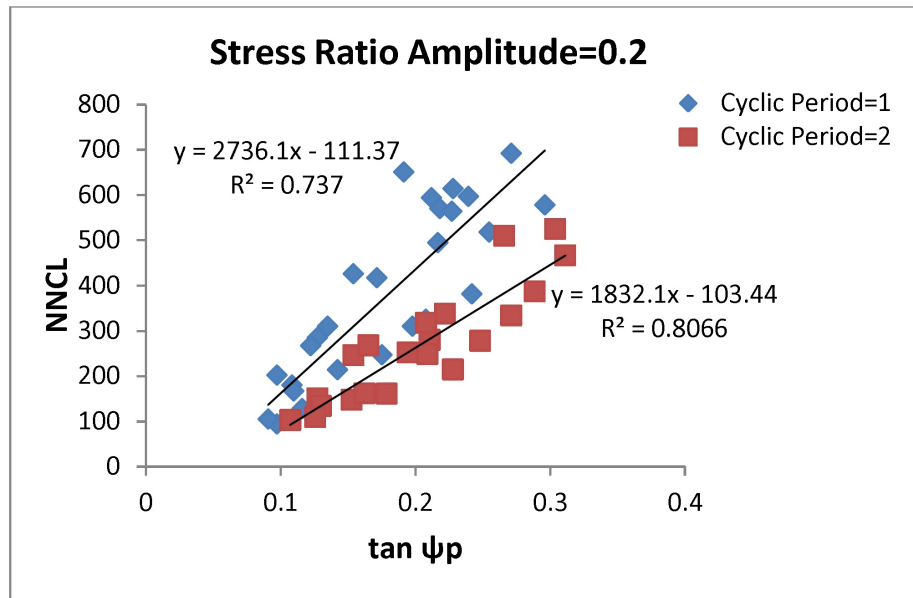


Figure 5.28. Kilyos Sand CP Effect on  $\tan \psi_p$ - $NNCL$  Relationships,  $SRA=0.2$ .

In the next section, it will be investigated whether there is a general behavior in all sand types with respect to stress ratio amplitude when the loading cyclic period is kept constant.

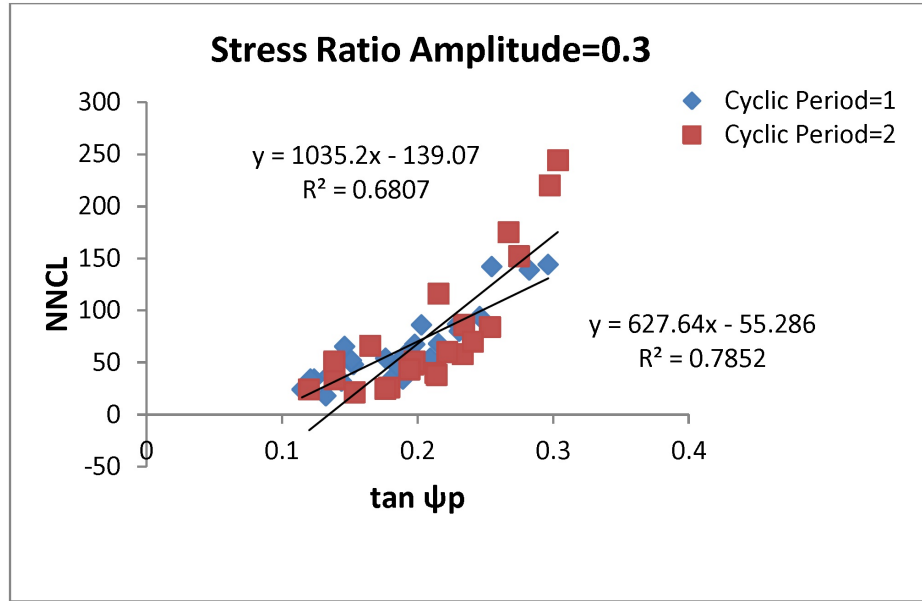


Figure 5.29. Kilyos Sand CP Effect on  $\tan \psi_p$ - $NNCL$  Relationships,  $SRA=0.3$ .

#### 5.6.4. Comparing CP Effects

To investigate the effect of CP and compare this effect on different sand types, normalized number of cycles to liquefy ratio for a specific stress ratio amplitude was defined as:

$$(NNCL)_{SRA} = \frac{NNCL_{for CP = 1}}{NNCL_{for CP = 2}} \quad (5.3)$$

where SRA refers to stress ratio amplitude, meaning that stress ratio amplitude should be kept constant (either 0.2 or 0.3).

Investigating the  $\tan \psi_p$  -  $(NNCL)_{SRA}$  for each specific SRA (0.2 and 0.3) shows that the effect of CP either decreases or increases with increasing dilation angle, depending on the sand type and SRA. However, the  $\tan \psi_p$  -  $(NNCL)_{SRA}$  variation slope tends to become zero with increase in dilation angle.



Table 5.5. Comparing CP Effects for SRA=0.2 sec.

Sand Type	Line equation for CP=1 sec	Line equation for CP=2 sec
<b>Sile</b>	$NNCL = 1468.4 \tan \psi_p + 38.45$	$NNCL = 608 \tan \psi_p - 16.8$
<b>Akpinar</b>	$NNCL = 1669.8 \tan \psi_p - 131.0$	$NNCL = 744.3 \tan \psi_p - 32.14$
<b>Kilyos</b>	$NNCL = 2736.1 \tan \psi_p - 111.37$	$NNCL = 1832.1 \tan \psi_p - 103.44$

Table 5.6. Comparing CP Effects for SRA=0.3 sec.

Sand Type	Line equation for CP=2 sec	Line equation for CP=2 sec
<b>Sile</b>	$NNCL = 129.5 \tan \psi_p + 12.87$	$NNCL = 60.5 \tan \psi_p + 7.47$
<b>Akpinar</b>	$NNCL = 149.2 \tan \psi_p + 13.8$	$NNCL = 103.8 \tan \psi_p - 5.99$
<b>Kilyos</b>	$NNCL = 1035.2 \tan \psi_p - 139.1$	$NNCL = 627.6 \tan \psi_p - 55.28$

For Akpinar and Sile sands the final  $(NNCL)_{SRA}$  are so close in magnitude. For both SRA values in Kilyos sand, final  $(NNCL)_{SRA}$ s are lower than this ratio for the other two sand types.

Another important point is that the certain dilation angle values, at which the slope of above diagrams becomes almost zero, are so similar for all three sand types, almost 12 degrees for cyclic period = 1 sec and 20 degrees for cyclic period = 2 sec. The changes in  $(NNCL)_{SRA}$  is negligible after these dilation angles.

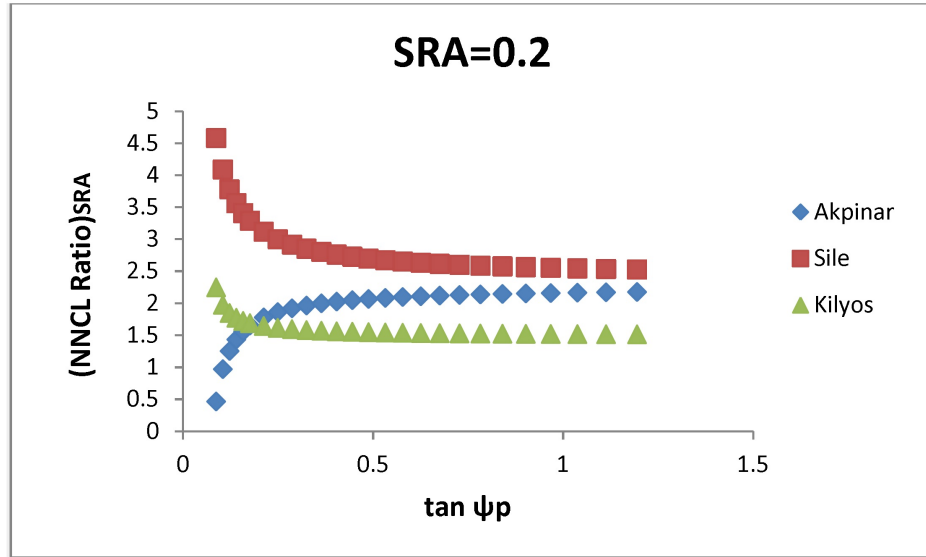


Figure 5.30.  $\tan \psi_p$ -( $NNCL$ )<sub>SRA</sub> Relationships, SRA=0.2.

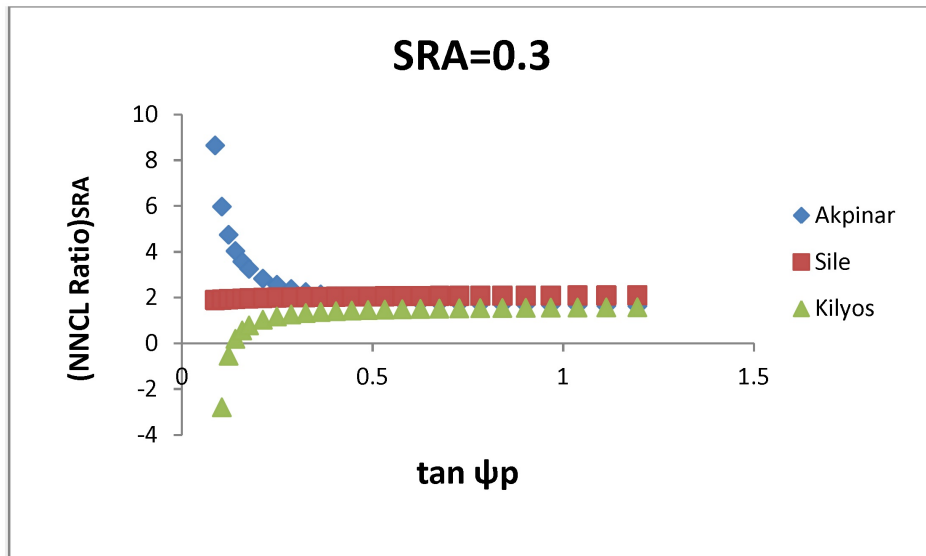


Figure 5.31.  $\tan \psi_p$ -( $NNCL$ )<sub>SRA</sub> Relationships, SRA=0.3.

## 6. CONCLUSIONS

The aim of this study is to investigate the influence of particle shape on peak dilation angle and liquefaction susceptibility. Additionally, the correlation between peak dilatancy angle and liquefaction susceptibility is examined. For this purpose an experimental program was set up. According to the testing program, first of all, microscopic pictures of 50 individual particles of 3 sand types were processed using an image processing software (ImageJ) to quantify their average circularity and roundness. Then conducting CD triaxial tests on each of 3 sand types, dilatancy constants  $\alpha_\psi$  and  $m_\psi$  of Cinicioglu and Abadkon [30] relationship were obtained. Finally over 200 cyclic simple shear tests were conducted on sand specimens with 4 different stress ratio amplitude and cyclic period combinations and differing consolidation pressures (50 kPa, 100 kPa and 150 kPa).

As the investigation progressed, other cyclic shearing variables were also taken into account. The effects of initial cyclic shear stress, consolidation pressure, stress ratio amplitude and cyclic period on dilation angle – number of cycles to liquefy or dilation angle – normalized number of cycles to liquefy were investigated.

Having the average circularity and roundness values,  $\alpha_\psi$  and  $m_\psi$  values of Cinicioglu and Abadkon [30] relationship which allows the calculation of peak dilation angle depending on sample relative density and confinement pressure, and cyclic behavior of each sample, the factors mentioned above were studied.

With all the test results analyzed, following conclusions can be drawn:

- (i) As the average circularity and roundness values increase, the critical state friction angle values increase.
- (ii) As the average circularity and roundness values increase, the value of  $\alpha_\psi$  increases following a line equation.
- (iii) As the average circularity and roundness values increase, the value of  $m_\psi$  decreases increases following a line equation.

- (iv) It is observed that the relationship between peak dilatancy angle and normalized number of cycles to liquefy is linear for sand samples loaded cyclically with the same stress ratio and the frequency of loading.
- (v)  $\psi_p$ - normalized number of cycles to liquefy relationships are functions of the stress ratio and frequency of loading.
- (vi) For samples loaded with same stress ratio amplitude, normalized number of cycles to liquefy for a constant  $\psi_p$  is higher for smaller cyclic period.
- (vii) For samples loaded with same cyclic period, normalized number of cycles to liquefy for a constant  $\psi_p$  is higher for smaller stress ratio amplitude.
- (viii) When defined as the ratio of normalized number of cycles to liquefy for cyclic period=1 to normalized number of cycles to liquefy for cyclic period=2 while stress ratio amplitude is kept constant, normalized number of cycles to liquefy ratio becomes constant after a certain peak dilation angle for all sand types. Meaning that after a certain peak dilation angle, the effect of changing cyclic period is constant with an increasing dilation angle.
- (ix) When defined as the ratio of normalized number of cycles to liquefy for stress ratio amplitude=0.2 to normalized number of cycles to liquefy for stress ratio amplitude=0.3 while cyclic period is kept constant, normalized number of cycles to liquefy ratio becomes constant after a certain peak dilation angle for all sand types. Meaning that after a certain peak dilation angle, the effect of changing stress ratio amplitude is constant with an increasing dilation angle.

### 6.1. Recommendations for Future Work

- (i) Studying more sand types with variety of circularity, roundness and surface roughness to quantify their effect on  $\alpha_\psi$  and  $m_\psi$  constant values
- (ii) Investigating the influence of over consolidation ratio on  $\tan \psi_p$ - $NCL$  relationship with regard to shear stress and cyclic period.
- (iii) Investigating the influence of particle surface roughness on  $\tan \psi_p$ - $NCL$  relationship.
- (iv) Quantifying the effect of cyclic period on  $\tan \psi_p$ -( $NNCL$ ) $_{SRA}$  relationship by conducting CSS tests with various values of CP.

## REFERENCES

1. Reynolds, O., "On the Dilatancy of Media Composed of Rigid Particles in Contact, With Experimental Illustrations", *Philosophical Magazine and Journal of Science*, Vol. 5, No. 20, pp. 469-481, 1885.
2. Lambe, T. W. and R. V., Whitman, "Soil Mechanics", John Wiley & Sons, New York, 1969.
3. Youd. T. L, "Packing Changes and Liquefaction Susceptibility", *Journal of the Geotechnical Engineering Division, ASCE*, Vol. 103, GT8, pp. 918-923, 1977.
4. Rodriguez, J., T., Edeskar and S., Knutsson, "Particle Shape Quantities and Measurement Techniques-A Review", *Electronical Journal of Geotechnical Engineering*, Vol. 18, pp. 169-198, 2013.
5. Wentworth, W. C., "The Shape of Beach Pebble", *Washington, U. S. Geological Survey Bulletin*, Vol. 131C, pp. 75-83, 1922.
6. Sukumaran, B. and A. K., Ashmawy, "Quantitative Characterisation of the Geometry of Discrete Particles", *Geotechnique*, Vol. 51, No. 7, pp. 619-627, 2001.
7. Wadell, H., "Volume, Shape, and Roundness of Rock Particles", *Journal of Geology*, Vol. 40, pp. 443-451, 1932.
8. Rittenhouse, G., "A Visual Method of Estimating Two-Dimensional Sphericity", *Journal of Sedimentary Petrology*, Vol. 13, pp. 79-81, 1943.
9. Powers, M. C., "A New Roundness Scale for Sedimentary Particles", *Journal of Sedimentary Petrology*, Vol. 23, No. 2, pp. 117-119, 1953.
10. Krumbein, W. C., "Measurement and Geological Significance of Shape and Round-

- ness of Sedimentary Particles”, *Journal of Sedimentary Petrology*, Vol. 11, No. 2, pp. 64-72, 1941.
11. Krumbein, W. C. and L. L., Sloss, “Stratigraphy and Sedimentation”, *Journal of Sedimentary Petrology*, 2 nd ed., W.H. Freeman, San Francisco, 1963.
  12. Luerkens, D. W., “The Theory and Application of Morphological Analysis: Fine Particles and Surfaces”, CRC Press, Inc., Boca Raton, FL, 1991.
  13. Ehrlich, R. and B., Weinberg, “An Exact Method for Characterization of Grain Shape”, *Journal of Sedimentary Petrology*, Vol. 40, No. 2, pp. 205-212, 1970.
  14. Vallejo, L. E., “Fractal Analysis of Granular Materials”, *Geotechnique*, Vol. 45, No. 1, pp. 159-163, March 1995.
  15. Bowman, E. T., K. Soga and W., Drummond, “article Shape Characterization Using Fourier Descriptor Analysis”, *Geotechnique*, Vol. 51, No. 6, pp. 545-554, 2001.
  16. Kaye, B. H., “Specification of the ruggedness and/or texture of a fine particle profile by its fractal dimension”, *Powder Technology*, Vol. 21, No. 1, pp. 1-16, 1978.
  17. Roscoe, K. H., A. N., Schofield and C.P., Worth, “On the Yielding of Soils”, *Géotechnique*, Vol. 8, No. 1, pp. 22-53, 1958.
  18. Schofield, A. N. and C. P., Wroth, *Critical state soil mechanics*, McGraw-Hill, New York, 1968.
  19. Cox, M. R. B, *The Influence of Grain Shape on Dilatancy*, Ph.D. Thesis, The University of Arizona, 2008.
  20. Budhu, M., *Soil Mechanics and Foundations*, John Wiley & Sons, Inc. New York, N.Y, 2000.
  21. Bishop, A. W., “Shear Strength Parameters for Undisturbed and Remoulded Soil

- Specimens. Stress-Strain Behaviour of Soils”, *Proceedings of the Roscoe Memorial Symposium, Cambridge University, 29-31 March*, pp. 3-58, 1972.
22. Abadkon, A., *Strength and Dilatancy of Anisotropic Cohesionless Soils*, Ph.D. Thesis, Bogazici University, 2012.
  23. Wood, D. M., *Soil Behaviour and Critical State Soil Mechanics*, Cambridge, Cambridge University Press, 1990.
  24. Taylor, D. W., *Fundamentals of Soil Mechanics*, John Wiley & Sons, Inc. New York, N.Y, 1948.
  25. Rowe, P. W., *The Stress Dilatancy Relations for Static Equilibrium of an Assembly of Particles in Contact*, *Proceedings of Royal Society, London, Series A*, 269, pp. 500-527, 1962.
  26. De Josselin de Jong, G., “Rowe’s Stress-Dilatancy Relation based on Friction”, *Géotechnique*, London, Vol. 26, No. 3, 527–534, 1976.
  27. Bolton, M. D., “Strength and Dilatancy of Sands”, *Géotechnique*, Vol. 36, No. 1, pp. 65-78, 1986.
  28. Vermeer, P. A. and R., de Borst, “Non-associated Plasticity for Soils, Concrete and Rock”, *Heron*, Vol. 29, No. 3, pp. 3-64, 1984.
  29. Schanz, T. and P. A., Vermeer, “Angles of Friction and Dilatancy of Sand”, *Géotechnique*, Vol. 46, No. 1, pp. 145-151, 1996.
  30. Cinicioglu, O. and A., Abadkon, “Dilatancy and Friction Angles Based on In Situ Soil Conditions”, *Journal of Geotechnical and Geoenvironmental Engineering*, 141(4), 06014019, 2015.
  31. Holubec I. and E., D’Appolonia “Effect of Particle Shape on the Engineering Properties of Granular Soils”, *Géotechnique*, ASTM STP, Vol. 523, pp. 304-318, 1996.



32. Bowden, F. P. and D., Tabor, *Friction and Lubrication*, Chem. Soc. Rep. 42, 20, 1945.
33. Ng, T. T., "Behavior of Ellipsoids of Two Sizes", *Journal of Geotechnical and Geoenvironmental Engineering*, Vol. 103, No. 10, pp. 1077-1083, October 2004.
34. Alshibli, K. A. and M. I., Alsaleh, "Characterizing Surface Roughness and Shape of Sands Using Digital Microscopy", *Journal of Computing in Civil Engineering*, Vol. 18, No. 1, pp. 36-45, January 2004.
35. Cho, G. C., J., Dodds and J. C., Santamarina, "Particle Shape Effects on Packing Density, Stiffness, and Strength: Natural and Crushed Sands", *Journal of Geotechnical and Geoenvironmental Engineering*, Vol. 132, No. 5, pp. 591-602, May 2006.
36. Guo, P. and X., Su, "Shear Strength, Interparticle Locking, and Dilatancy of Granular Materials", *Canadian Geotechnical Journal*, Vol. 44, pp. 579-591, 2007.
37. Hazen, A., *Transactions of the American Society of Civil Engineers*, Vol. 83, pp. 1717-1745, 1920.
38. Iwasaki, T., F., Tatsuoka, K., Tokida and S., Yasuda, *A Practical Method for Assessing Soil Liquefaction Potential Based on Case Studies at Various Sites in Japan*, 2nd International Conference on Microzonation, San Francisco, pp. 885-896, 1978.
39. Iwasaki, T., K., Tokida, F., Tatsuoka, S., Watanabe, S., Yasuda and H., Sato, *Microzonation for Soil Liquefaction Potential Using Simplified Methods*, 3rd International Earthquake Microzonation Conference, Seattle, pp. 1319-1330, 1982.
40. Seed, H. B. and W. H., Peacock, "Test Procedures for Measuring Soil Liquefaction Characteristics", *Journal of the Soil Mechanics and Foundations Division*, Vol. 97, No. 8, pp. 1099-1119, 1971.

41. Seed, H. B., “Soil Liquefaction and Cyclic Mobility Evaluation for Level Ground During Earthquakes”, *Journal of the Geotechnical Engineering Division*, Vol. 105, No. 2, pp. 201–255, 1979.
42. Seed, H. B., I., Idriss and I., Arango, “Evaluation of Liquefaction Potential Using Field Performance Data”, *Journal of Geotechnical Engineering*, Vol. 109, No. 3, pp. 458–482, 1983.
43. Seed, H. B., K., Tokimatsu, L., Harder and R., Chung, “The Influence of SPT Procedures in Evaluating soil Liquefaction Resistance”, *Journal of Geotechnical Engineering*, Vol. 111, No. 12, pp. 1425–1445, 1985.
44. Carraro, J., P., Bandini and R., Salgado, “Liquefaction Resistance of Clean and Nonplastic Silty Sands Based on Cone Penetration Resistance”, *Journal of Geotechnical and Geoenvironmental Engineering*, Vol. 129, No. 11, pp. 965–976, 2003.
45. Ishibashi, I., M. A., Sharif and W. L., Cheng, “Confining Pressure, Grain Angularity, and Liquefaction”, *Soils and Foundations*, Vol. 22, No. 1, pp. 39–48, 1982.
46. Vaid, Y. P., J. C., Chern and H., Tumi, “Confining Pressure, Grain Angularity, and Liquefaction”, *Journal of Geotechnical Engineering*, Vol. 111, No. 10, pp. 1229–1235, 1985.
47. Sukumaran, B., *Study of the Effect of Particle Characteristics on the Flow Behavior and Strength Properties of Particulate Materials*, Ph.D. Thesis, Purdue University, 1996.
48. Ashour, M. and G., Norris, “Liquefaction and Undrained Response Evaluation of Sands from Drained Formulation”, *Journal of Geotechnical and Geoenvironmental Engineering, ASCE*, Vol. 125, No. 81, pp. 649–658, 1999.
49. Sitharam, T. G., “Discrete Element Modeling of Cyclic Behaviour of Granular Materials”, *Geotechnical and Geological Engineering*, Vol. 21, No. 4, pp. 297–329, 2003.

50. Dinesh, S. V., *Discrete Element Simulation of Static and Cyclic Behaviour of Granular Media*, Ph.D. Thesis, Indian Institute of Science, Bangalore, 2002.
51. Vinod, J. S., *Liquefaction and Dynamic properties of Granular Materials: A Discrete Element Approach*, Ph.D. Thesis, Indian Institute of Science, Bangalore, 2006.
52. Ashmawy, A. K., B. Sukumaran and V. V., Hoang, *Evaluating the Influence of Particle Shape on Liquefaction Behavior Using Discrete Element Modeling*, *Proc, 13th International Offshore and Polar Engineering Conference, ISOPE*, 2, pp. 542-549, 2003.
53. Vallejo, L. E., "Fractal Analysis of Granular Materials", *International Journal of Rock Mechanics and Mining Sciences and Geomechanics Abstracts*, Vol. 8, No. 32, pp. 317A, 1995.
54. Gori, U. and M., Mari, "The Correlation between the Fractal Dimension and Internal Friction Angle of Different Granular Materials", *Soils and Foundations*, Vol. 41, No. 6, pp. 17-23, 2001.
55. Bowman, E. T., K., Soga and T. W., Drummond, "Particle Shape Characterisation Using Fourier Descriptor Analysis", *Geotechnique*, Vol. 51, No. 6, pp. 545-554, 2001.
56. Whalley, W. B. and J. D., Orford, "Analysis of Scanning Electron Microscopy Images of Sedimentary Particle Form by Fractal Dimension and Fourier Analysis Methods", *Scanning Electron Microscopy*, Part. 2, pp. 639-647, 1982.
57. Thomas, M. C., R. J., Wiltshire and A. T., Williams, "The Use of Fourier Descriptors in the Classification of Particle Shape", *Sedimentology*, Vol. 42, pp. 635-645, 1995.
58. Rasband, W. S., *ImageJ*, *National Institutes of Health, Bethesda, Maryland, USA*, 2004, <http://rsb.info.nih.gov/ij/>, [Accessed December 2014].

59. Syverud, K., G., Chinga, P. O., Johnssen, , I., Leirset and K., Wiik, "Analysis of Lint Particles from Full-Scale Printing Trials", *Appita J*, Vol. 60, No. 4, pp. 286-290, 2007.
60. Bishop, A. W. and D. J., Hankel, *The Measurement of Soil Properties in the Triaxial Test, 2nd Edition*, Edward Arnold, London, 1962.
61. Terzaghi, K., "Tragfähigkeit der Flachgründungen", *1st Cong. Int. Ass. Bridge Struct. Eng.*, pp. 659-672., 1932.
62. Rendulic, L., "Ein Grundgesetz der Tonmechanik und sein Experimentaler Beweis", *Bauingeniuer*, Vol. 18, pp. 459-467, 1937.
63. Hight, D. W., *Laboratory Investigations of Sea Bed Clays*, Ph.D. Thesis, Imperial College, University of London, 1983.
64. Bishop, A. W. and L. D., Wesley, "A Hydraulic Triaxial Apparatus for Controlled Stress Path Testing", *Geotechnique*, Vol. 25, No. 4, pp. 657-670, 1975.
65. Atkinson, J. H., "Simple and Inexpensive Pressure Control Equipment for Conventional and Stress Path Triaxial Testing of Soils", *Geotechnique*, Vol. 35, No. 1, pp. 61-63, 1985.
66. Atkinson, J. H., J. S., Evans and C. R., Scott, "Developments in Microcomputer Controlled Stress Path Testing Equipment for Measurement of Soil Parameters", *Ground Engineering*, Vol. 18, No. 1, pp. 15-22, 1985.
67. Siddique, A., C. R. I., Clayton, S. A., Khatrush, and R. J., Hopper, "An automated Triaxial System for Stress and Strain Path Testing of Soils", *Journal of the Institute of Engineers*, Vol. 27, No. 2, 1996.
68. Franke, E., M., Kiekbusch and B., Schuppener, "A New Direct Simple Shear Device", *Geotechnical testing journal*, Vol. 2, No. 4, PP. 190-199, 1979.

69. Dyvik, R., T., Berre, S., Lacasse and B., Raadim, “Comparison of Truly Undrained and Constant Volume Direct Simple Shear Rests”, *Geotechnique*, Vol. 37, No. 1, pp. 3-10, 1987.
70. DeGroot, D. J., C. C., Ladd and J. T., Germaine, “Direct Simple Shear Testing of Cohesive Soils”, *MIT Research Report*, No. R92-18, Center for Scientific Excellence in Offshore Engineering, Department of Civil Engineering, MIT, Cambridge, MA, 1992.
71. DeGroot, D. J., J. T., Germaine and R., Gedney, “An Automated Electropneumatic Control System for Direct Simple Shear Testing”, *Geotechnical Testing Journal, GTJODJ*, Vol. 14, No. 4, pp. 339-348, 1991.
72. DeGroot, D. J., J. T., Germaine and C. C., Ladd, “The Multidirectional Direct Simple Shear Apparatus”, *Geotechnical Testing Journal, GTJODJ*, Vol. 16, No. 3, pp. 283- 295, 1993.
73. Bjerrum, L. and A., Landva, “Direct Simple Shear Tests on a Norwegian Quick Clay”, *Géotechnique*, Vol. 16, No. 1, pp. 1–20, 1966.
74. Gulick, J., *Circle Test plugin in ImageJ*, 2000, Orphan Technologies, Inc., <http://rsbweb.nih.gov/ij/plugins/circle-test.html>, [Accessed December 2014].
75. Altunbas, A., *Influence of Dilatancy on Slip Panes and on Localization of Strains*, Ph.D. Thesis, Bogazici University, 2015.
76. Silver, M. L., *Laboratory Triaxial Testing Procedures to Determine the Cyclic Strength of Soils*, Report No. NUREG-31, U.S. Nuclear Regulatory Commission, Washington DC, 1977.
77. Yoshimi, Y. and H., Oh-Oka, “Influence of Degree of Shear Stress Reversal on the Liquefaction Potential of Saturated Sand”, *Soils Found*, Vol. 15, pp. 27–40, 1975.

78. Sumita, I. and M., Manga, “Suspension Rheology Under Oscillatory Shear and its Geophysical Implications”, *Earth and Planetary Science Letters*, Vol. 269, No. 3, pp. 468-477, 2008.
79. Wong, A. and C. Y., Wang, “Field Relations Between the Spectral Composition of Ground Motion and Hydrological Effects During the 1999 Chi-Chi (Taiwan) Earthquake”, *Journal of Geophysical Research: Solid Earth (1978–2012)*, Vol. 112, No. B10, 2007.